Università degli Studi di Pavia

Facoltà di Ingegneria
Dipartimento di Ingegneria Civile e Architettura

Tesi per il conseguimento della laurea magistrale in:
Ingegneria Civile Strutturistica

Title:
Design and rapid prototyping of a SMA based actuator

Titolo:
Progetto e prototipazione rapida di un attuatore basato su leghe a memoria di forma

candidato:
Luca Marioni
relatore:
Prof. F. Auricchio - Università degli Studi di Pavia
correlatore:
Dott. M. Ferraro - Università degli Studi di Pavia

A.A. 2013/14

The miracle
of the appropriateness of the language of mathematics
for the formulation of the laws of physics
is a wonderful gift which we neither understand
nor deserve

E. Wigner

Abstract

Materials, especially in the field of structures engineering, have always been studied and analysed by their mechanical properties. Even today, the behaviour of the main building materials such as steel, concrete and wood is described through stiffness, yield strain, fracture stress *et cetera*; given a material, it is supposed to passively and indiscriminately react to external inputs. Despite the fact that this classical approach to the study of materials is the most common approach, new and more sophisticated material draw attention to its lacks: these materials could be designed in order to react differently in base of the kind and magnitude of external stimuli. This work will mainly focus on Shape Memory Alloys (SMA); these materials manage to drastically change their behaviour according to temperature. The peculiar capacity of these materials has made them very interesting in the field of actuators as they are able to produce large motion in low volumes without the use of mechanical components. In this thesis, classical SMA's constitutive models will be investigated, after which will be performed the numerical analysis of a real SMA-based micro-actuator through a commercial Finite Element Method (FEM) software(Abaqus). These analysis will support the effective project and construction of a large-scaled prototype of an actuator by a 3D printer in order to test how these simulations can predict the real behaviour of the actuator.
The world of Shape Memory Alloys seems to be little inherent to structural engineering; however one of this thesis goals is to understand the great potential of these materials and how they can contribute in the evolution of structures by giving the possibility to really interact with users and their needs and not only provide a mechanical performance.

Sommario

I materiali, specialmente quelli da costruzione, sono da sempre studiati mediante le loro proprietà meccaniche; ancora oggi i materiali strutturali di maggiore diffusione quali acciai, murature, cementi armati e legname sono identificati attraverso la loro rigidezza, deformazioni e tensioni a rottura e snervamento; dato un materiale il suo utilizzo è pensato come una reazione passiva e indiscriminata alle sollecitazioni tensodeformative esterne. Nonostante ciò, nuovi e sofisticati materiali, sviluppati nel corso degli ultimi decenni, evidenziano come tale approccio alla progettazione risulti sempre più inadeguato alle possibilità che le nuove tecnologie ci offrono: questi nuovi materiali possono essere prodotti in modo da reagire differentemente in base al tipo e all'intensità degli stimoli esterni. Il lavoro seguente si concentrerà sulle leghe a memoria di forma, leghe che riescono a modificare la propria forma e le proprie caratteristiche meccaniche in base alla temperatura. Grazie a queste capacità, le leghe a memoria di forma hanno conquistato un ruolo di primissimo piano nel campo degli attuatori, in quanto sono in grado di produrre elevate forze e cinematismi in volumi ridotti, senza tuttavia la necessità di sistemi meccanici. In questa tesi si studieranno i classici modelli costitutivi adottati per lo studio delle leghe a memoria di forma, dopodiché verranno presentati i risultati della progettazione e delle analisi FEM di un reale attuatore prodotto mediante prototipazione rapida 3D, in modo da poter commentare il supporto che tali simulazioni possono dare alla progettazione dell'elemento.
Il mondo degli attuatori basati su leghe a memoria di forma trova oggi poco spazio nell'ambito dell'ingegneria strutturale, tuttavia è proposito di questa tesi cercare di capire il potenziale di questi materiali e come essi possano contribuire all'evoluzione delle strutture, in modo che queste non svolgano un semplice lavoro meccanico, ma possano realmente interagire con l'utenza, garantendo maggiore efficienza ed efficacia durante l'esercizio.

Contents

List of Figures

List of Tables

Introduction to Shape Memory Alloys and Actuators

From a mechanical to a functional design approach

Materials have always been defined by their mechanical properties. Even today, structural engineering carries in this cultural approach: just think that the main structural materials such as steel, concrete, masonry, wood *et cetera* are described through mechanical parameters as stiffness, ductility, yield and fracture strain. Nevertheless, research in materials has produced lots of sophisticated and advanced materials able not only to passively and indiscriminately react to external stimuli, but also to interact "intelligently" with the external world. Among these materials we can find a large variety of properties, for example *piezoelectric* materials manage to product electric potential when deformed, *PH-sensitive* materials are able to change in volume and colour accordingly to the environment's PH, *acoustic* materials product noise when deformed over a threshold, and so on. In addition of these, exist the material considered in this thesis, the shape memory alloys, that change their shape and mechanical properties accordingly to their temperature.
The approach to the material has therefore become more complex: the material is no more called to just ensure a mechanical performance, but to perform a function. It's important to point up that even in the classical approach to design a certain function was needed, but was carried out by the structural element or by a set of mechanical components, while with the *functional design* approach is the material itself to be designed in order to carry out its function without any other mechanical element. Thanks to the capacity of these materials to react differently according to the environment, engineers have the possibility to re-invent the classical mechanical and structural elements because the function they were used to carry out can be achieved in an easier way employing intelligent materials. This is the spirit of SMA-based actuators: as will be extensively discussed in 2, they employ the capacity of shape memory alloys to produce hight displacements in low volumes if correctly actuated without mechanical elements in order to get a more simple and durable actuation system.

Chapter 1

Shape Memory Alloys

Shape Memory Alloys (SMA) have been widely used for decades in intelligent systems design thanks to their peculiar properties. They are able to get external stimuli (thermal, magnetic or mechanical) and to react in different and predetermined ways that depend on the way in which they were manufactured. Thank to this ability, important mechanical parameters such as stiffness, shape, dumping manage to change and adapt themselves to working conditions.
The expression "Shape Memory" refers to the main macroscopic feature related to these materials i.e. their capability to "remember" the original shape and to return to it, even after have been subjected to significant strain states; this phenomenon happen through two main mechanisms:

- **Shape Memory Effect - SME**: when the alloy get deformed below a predetermined temperature, it will be able to recover the initial shape if properly heated.
- **Pseudo-Elasticity - PE**: the alloy largely deformed at hight temperature is able to recover the initial configuration when the cause of deformation is removed.

These mechanisms are caused by the fact that two distinct solid phases exist in the material as crystal lattice get stability in two configurations which depend from stress rate and temperature: *martensite* configuration, stable at low temperatures and stress-free state, and *austenite* configuration, stable at high temperatures and stress-free-state.
Moreover, SMA thermomechanical properties strongly depend from the manufacturing processes, thus allowing to tune the material characteristics in order to fit the alloy performance into the expected working conditions; in addition is important to stress that the metallurgy aspect of these materials is not far from steel: they're are able to be formed in wires and sheets which are the principal commercial elements for these alloys.

1.1 Martensite transformation

As previously mentioned in chapter 1, SMA main properties are caused by transformations between two different solid phases: austenite and martensite. As shown in fig.1.1, the main difference between the two phases is the molecular crystal: for austenite it is stable at hight temperatures characterized by strong bonds and an highly ordered atom disposition, but during cooling processes atom bonds weaken and relative displacements occur, which dues a deformation of the molecular crystal. It is interesting to stress that despite the terms "austenite" and "martensite" originally referred only to phases of steel, they are now commonly accepted and refers not to the type and nature of crystals but to the type of transformation.
Solid phase transformations are of two types:

- *Diffusional transformations*, in which a new phase can onlybe formed by moving atoms randomly over relatively long distances. Long range diffusion is required becouse the new phase is of a different chemical composition than the matrix from which it is formed. Since atomic migration is required, the progress of this type of transformation is dependent upon both time and temperature.

- *Displacive transformations* which do not require such long range movements; in these cases atoms are cooperatively rearranged into a new, more stable crystal structure, but without changing the chemical nature of the matrix. Because no atomic migration is necessary, these transformations generally progress in a time-independent fashion, with the motion of interface between the two phases being limited only by the speed of sound. Unlike the first type of transformations, as no chemical transformation occurs, displacive transformations are reversible.

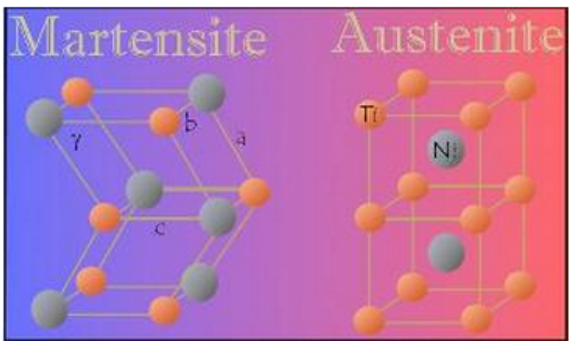

Figure 1.1: Crystal structures of Austenite and Martensite

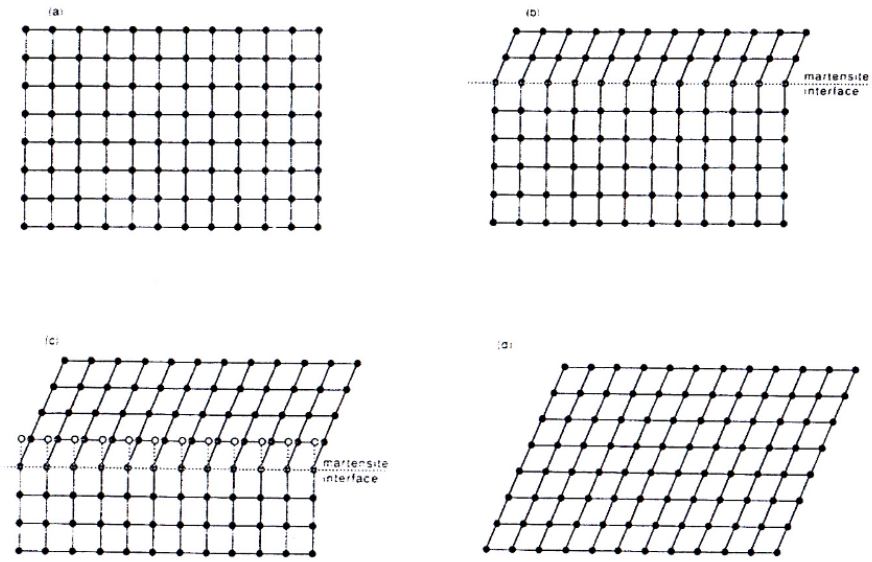

Figure 1.2: Two dimension schematization of a full transformation from a completely austenitic phase (a) to a completely martensitic phase (d) [1]

Martensitic transformations in SMA are usually of the second type, and are formed upon cooling from an higher temperature phase called *parent phase* or *austenite*. This type of transformation are *first order transformations* as release heat during direct transformation (from austenite to martensite) and adsorb heat during the reverse transformation (from martensite to austenite).
From the lattice point of view, the transformation from austenite to martensite is often modelled of in two parts: the *bain strain* and the *lattice-invariant shear*. The bain strain, or lattice deformation, consists of all the atomic displacements needed to produce the new structure configuration from the old one; in fig.1.2 a bidimensional schematization of the problem is proposed: the austenitic structure (a) transform in a fully martensitic structure by (b). Note that, as the interface progresses one atomic layer, each atom is required to move by only a very small amount.

The second part of the martensitic transformation is an accomodation step: the martensitic structure produced by the bain strain usually presents different shape and volume than the surrounding austenite. It is therefore necessary for martensite to adapt its configuration in order to minimize discontinuity with the austenite's interface. There are two general mechanisms by which this occurs: *slip* and *twinnig* (fig.1.3). While slip is a permanent process, twinning accomodate shape changes in a reversible way, but is not able to accomodate volume changes. Since SME is a fully reversible phenomenon, it is reasonable to assume that twinning accomodation is dominant with respects to slip.

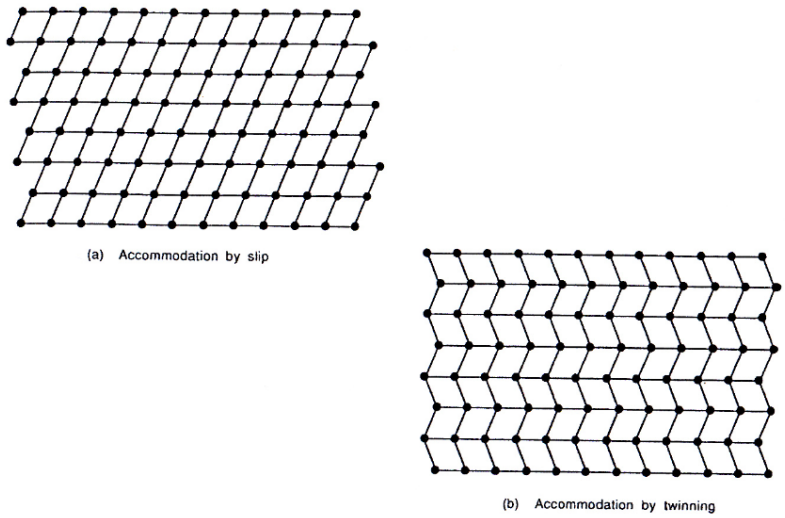

Figure 1.3: The two mechanisms of accomodating the shape change due the atomic shear of a martensitic transformation [1]

Another interesting aspect of martensitic structure, is that weakened intermolecular bonds permit permit easly sliding of crystal structure when a shear stress is applied. This phenomenon, shown in fig.1.4, is called *detwuinning* convert the existing *multivariant* structure into a new *monovariant* one; the new variant follows the most favourable orientation of crystals, according to the direction of the stress, and is stable as long as a non-zero stress rate is imposed.

From a macroscopic perspective, the detwinning process modify the global stiffness of the element; as shown in fig.1.5, stress-strain curve at low temperaturecan be subdivided in four regions:

- low stress/strain rate, when no crystal lattice modification occurs
- plateau, where structures gets detwinned, the crystals easly slide each other and the global stiffness is very low
- hardening caused by the completely detwinned state of martensite and no more shape accomodation is possible
- onset of slip accomodation and degradation of chemical nature of the matrix, case not object of this thesis

The stress/strain rate is not only cause of the detwinning process, but also can induce the martensite transformation itself. As it has already been told, austenite phase is stable at high temperatures and in a stress-free state; the application of

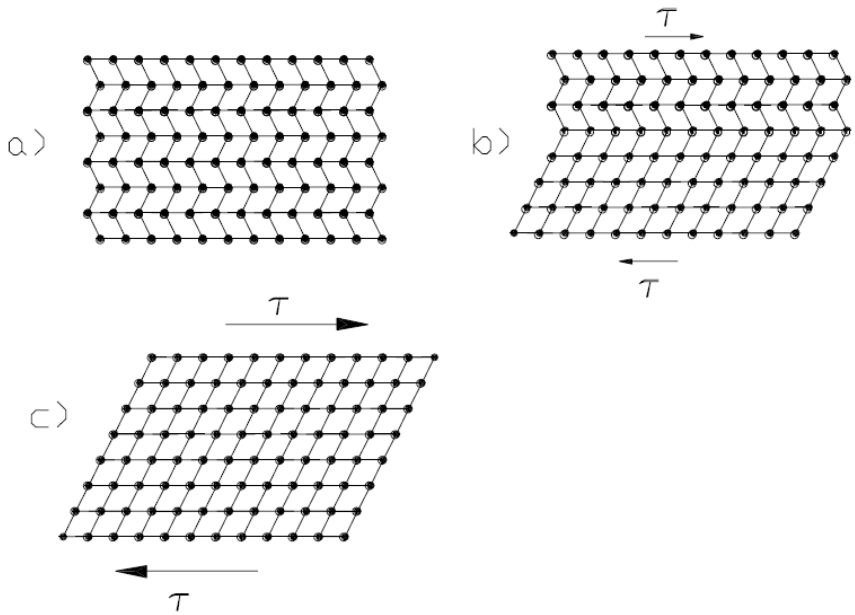

Figure 1.4: Detwinning process in a shear-loaded twinned martensite structure

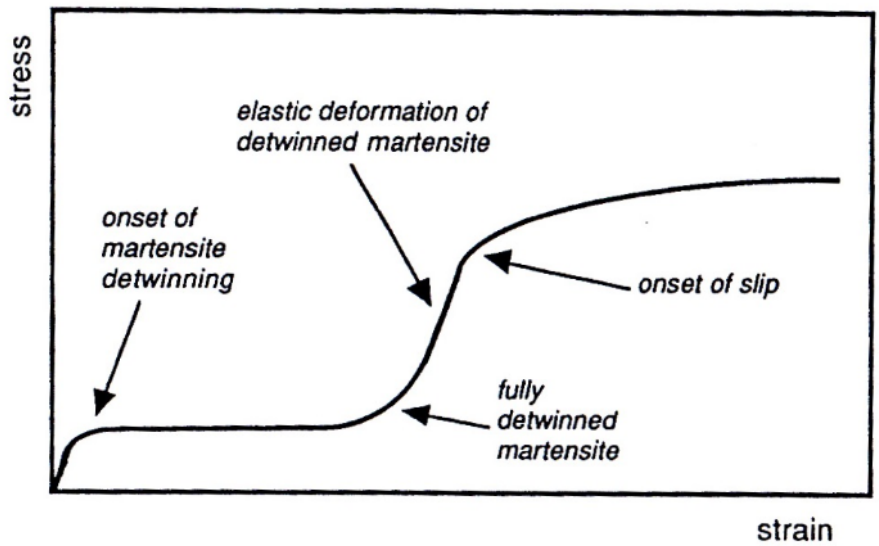

Figure 1.5: Stress-strain curve for a twinned martensite material

shear stress weaken the crystal bonds inducing the direct transformation as shown in fig. 1.2. Finally, all SMA-related phenomena can be microscopically modelled by the transformation (caused by a variation in temperature or stress) between three stable lattice configurations, as shown in fig. 1.6.

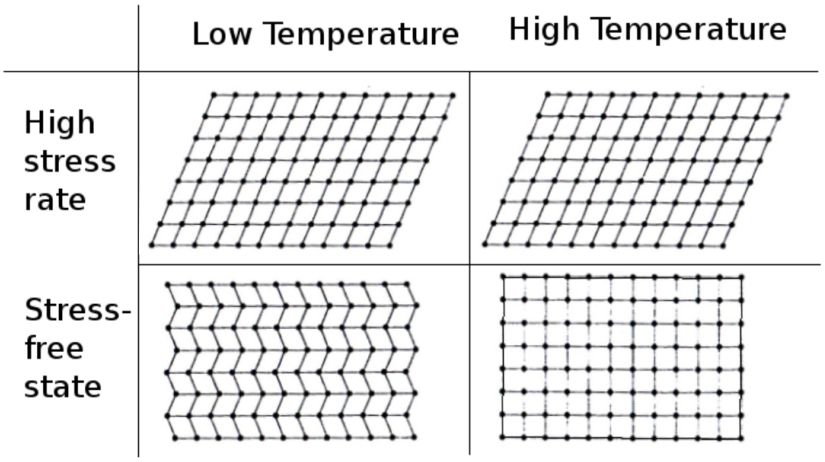

Figure 1.6: Lattice dependency on stress and temperature variations

Until now martensite transformation has been discussed in terms of "high" and "low" temperatures, but no magnitude has been mentioned. This because transformation temperatures depends on the chemical nature of the material. In table 1.1 temperatures for main alloys are reported. Ignoring the real magnitudes, noticeable

Table 1.1: Princopal features of most common commercial shape memory alloys [3]

Alloy	Composition	Tranformation Temperatures [°C]
Ag-Cd	44/49% atom. Cd	from -190 to -50
Ag-Cd	46/50% atom. Cd	from from 30 to 100
Cu-Al-Ni	14% atom. Al. 4% atom. Ni	from -140 to 100
Cu-Sn	15% atom. Sn	from -120 to 30
Cu-Zn	38/41% atom. Zn	from -180 to -10
In-Ti	18/23% atom. Ti	from 60 to 100
Ni-Al	36/38% atom. Al	from -180 to 100
Ni-Ti	49/51% atom. Ni	from -50 to 110
Fe-Pt	25% atom. Pt	≃-130
Mn-Cu	5/35% atom. Cu	from -250 to 180
Fe-Mn-Si	32% atom. Mn, 6% atom. Si	from -200 to 150

temperatures of transformation will be defined as:

- M_s: is the temperature when direct transformation begins
- M_f: is the temperature when direct transformation finishes

- A_s: is the temperature when inverse transformation begins
- A_s: is the temperature when direct transformation finishes

In fig. 1.7 a synthetic representation of martensitic transformation is proposed.

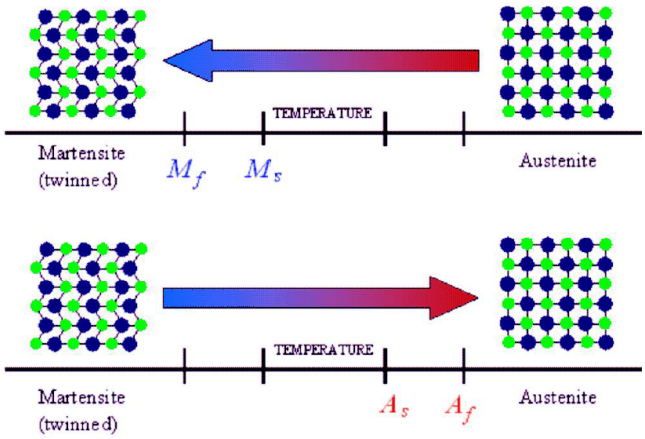

Figure 1.7: Noticeable temperatures for direct and reverse transformation

1.2 Shape memory effect

1.2.1 The origin of shape memory

Although it has not been explicitly stated, it is implied from the above considerations, that martensite is generally a lower symmetry phase than austenite. The consequence of this is that exist many ways in which martensite can form from austenite, but there is only one possible route which will return the austenite structure. Because of this, martensite phase can be deformed in different stable variants, but the reverse transformation will return the original undeformed austenite structure.
This concept becomes the foundation for the shape memory effect. Upon cooling from austenite (fig. 1.8(a)), the self-accomodating variants of martensite are formed (fig.1.8(b)). The twin boundaries migrate during deformation resulting in a biased distribution of martensite variants. Independently from the new accomodated configuration, by heating, original austenite structure is formed. By performing a new martensitic transformation, the lowest-symmetry stable martensite configuration is returned, as the high symmetry is caused only by external mechanical work.

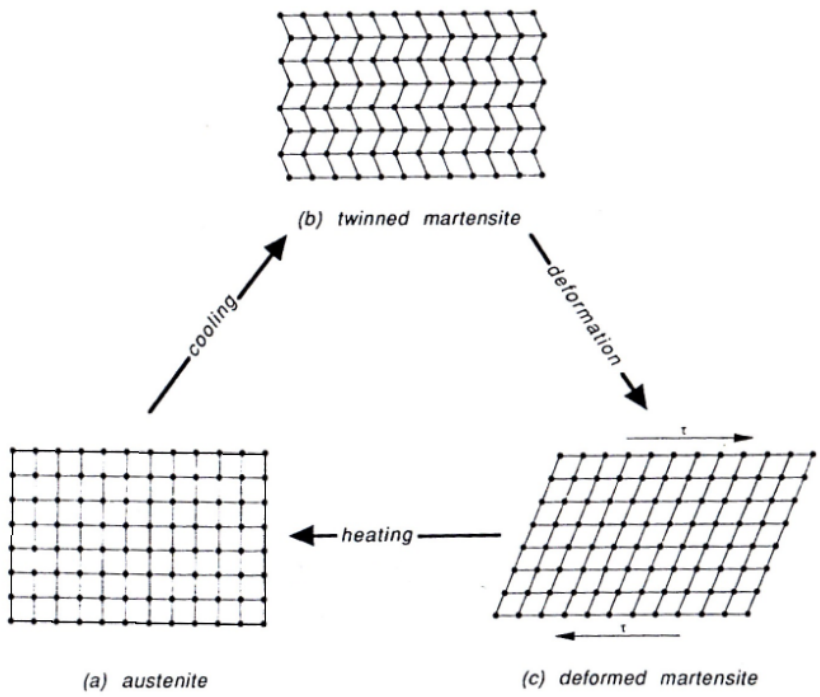

Figure 1.8: Microscopical description of shape memory effect

1.2.2 One-way shape memory effect

The one-way shape memory effect is the closest implication of what has been discussed in section 1.2.1. Referring to fig. 1.9, the element in martensite phase is loaded and highly deformed getting permanent deformations due to detwuinning process so, after having removed the load, this strain isn't recovered. When the specimen (e.g. a spring) gets heated above A_f, the original shape is completely recovered.

This macroscopic phenomenon could be efficiently reported by a curve in a 3-axis space: temperature, stress and strain. This representation is very useful in order to

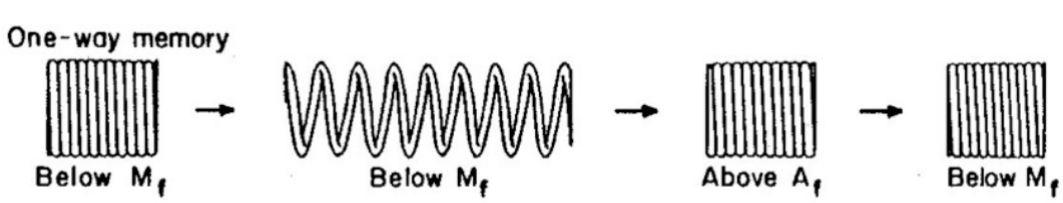

Figure 1.9: One-way shape memory effect for a spring element

understand the SMA behaviour. In fig. 1.10 is shown the first loading-unloading phase at constant temperature in $\sigma - \epsilon$ plane: from a stress-free state in point "0", when the crystal lattice gets loaded, accomodates in a detwinned martensite phase characterised by high stress-rate (see fig. 1.6) in point "1". By removing the external load, just a part of the strain is recovered, as the lattice adjust in a martensite configuration in point "2". After that is shown the complete recovery of strain of the unloaded element by heating it and inducing reverse transformation from a stress-free martensite phase to a stress-free austenite configuration of point "3".

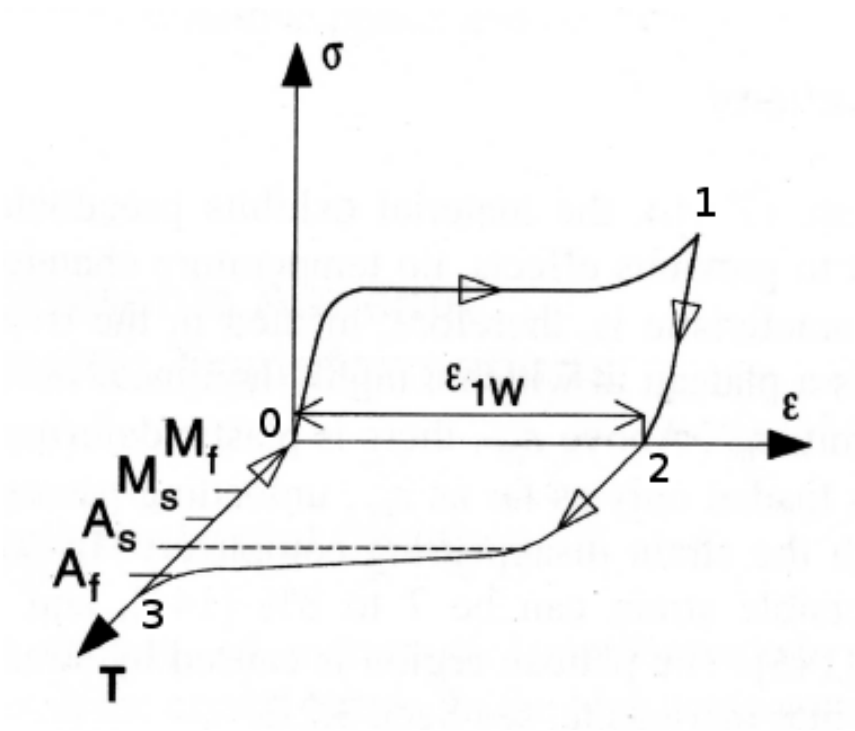

Figure 1.10: One-way shape memory effect represented in a $T - \sigma - \epsilon$ space

1.2.3 Two-way shape memory effect

The two-way shape memory effect is based on a similar concept then the one-way effect described above. The main difference is that in the latter one, austenite transforms in a self-accomodating lattice configuration, without "remembering" the previous deformed martensite shape, whereas in the two-way effect transformation recovers the shape of deformed martensite. This, as reported in fig. 1.11, implies a biunivocal correspondence between a specific austenite and martensite configuration and can be repeated any number of times.

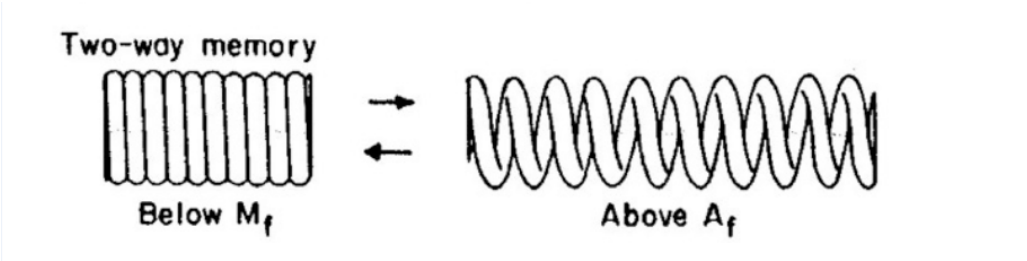

Figure 1.11: Two-way shape memory effect for a spring element

This macroscopic phenomenon could be efficiently reported by a curve in a 3-axis space: temperature, stress and strain. This representation is very useful in order to understand the SMA behaviour. In fig.1.12 is shown that an unloaded martensite deformed element recovers original shape when heated, as seen in section 1.2.2. Differently from one-way effect, upon cooling the austenite, strain changes, recovering the original martensite deformation.

This property is very useful in actuation, as alloys to change between two configuration just by temperature control, without any external mechanical work, as will be widely commented in chapter 2.

Despite the fact that this effect results very useful, it's not as diffuse as the one way

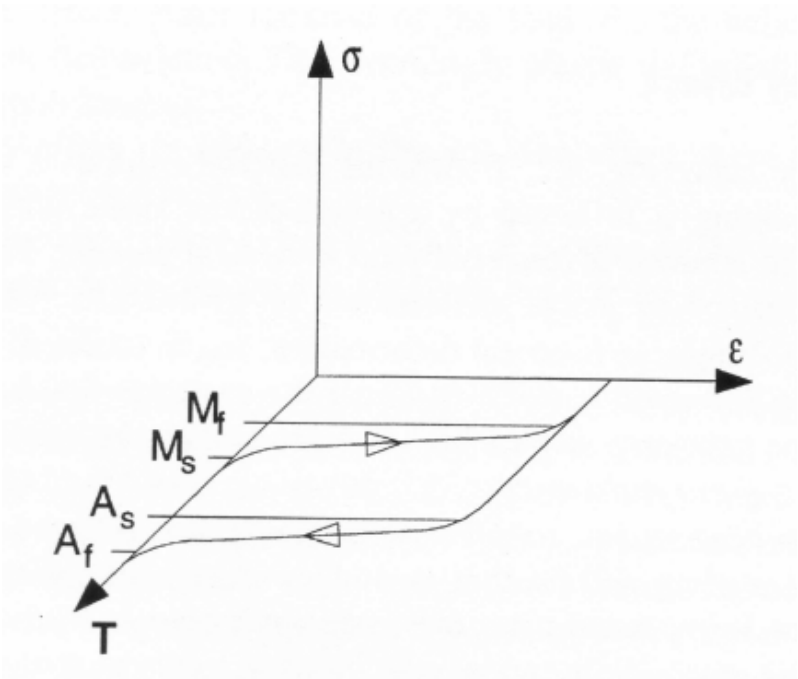

Figure 1.12: Two-way shape memory effect represented in a $T - \sigma - \epsilon$ space

effect alloys because the process which produces these alloys is more complicated and expensive; the martensite undergoes to particular thermomechanical processes in order to induce microstresses in molecular lattice which influence the making of martensite, creating preferential variants of the lattice itself.

1.2.4 Superelasticity

So far it has been shown how shape memory effect could be induced by temperature variation, but there is another way to cause transformation, regardless of temperature: superelasticity. It has been discussed that with no stresses, martensite is formed by cooling the material below M_s; nevertheless, in the same material, martensite could form even at higher temperatures than M_s when an adeguate stress is applied. The magnitude of stress required to induce transformation increases accordingly to temperature, until M_d, the maximum temperature which allows the formation of martensite; in fact, above that temperature austenite is very stable and the stress necessary to form martensite is higher than the one which would create dislocations in the lattice.
Pseudoelastic phenomenon is illustrated in figure 1.13 by a stress-strain curve for a 1-d loading/unloading test at a constant temperature $T^* > A_f$; in the state corresponding to point "1", the material accomodates into a austenite phase, as the temperature is greater than A_f and no stress is applied. By applying a external load, the direct transformation is induced and the material accomodates into a martensite phase high stress rate (point "3"). After that, by removing the external load, as the temperature is still greater than A_f, the material comes back to a austenite phase, recovering the original shape.

It is noticeable that transformation due to mechanical work is not permanent: when unloaded, the element returns to have an austenite microstructure recovering the original shape. From an engineering point of view is important to stress the magnitude of the pseudoelastic effect: even if it depends on temperature, the maximum strain which the material is able to completely recover is about 10%, a very high value if compared to classical materials; above that range of strain, molecular dislocations start and the rate of recoverable strain decrease.
Superelasticity and shape memory effect have been discussed separately for ease of exposition, but they are not unlinked phenomena. In order to really understand the material behaviour, is important to see how superelasticity and shape memory effect are two sides of the same coin; as illustrated in figure 1.14 the two effects coexist but superelasticity overcomes shape memory effect at low temperatures and viceversa for high temperatures. Below M_f the specimen subjected to a tensile 1D test turns its lattice configuration between twinned martensite, detwinned martensite, austenite and then twinned martensite again (fully SME); above A_f the material turns between an austenite phase, detwinned martensite and then, after having removed

the load, austenite again (PE effect). Finally, at very high temperatures, austenite is so stable that no load can induce a transformation to twinned martensite.

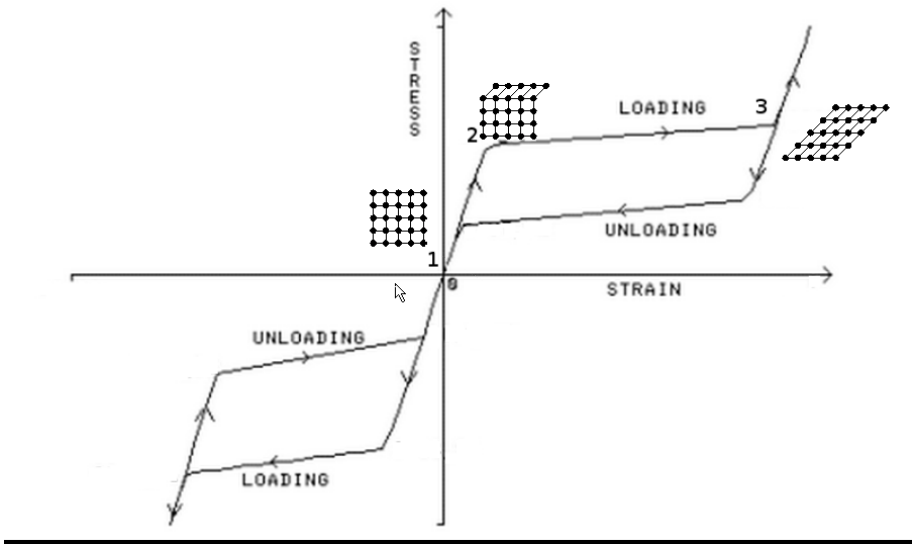

Figure 1.13: Superelasticity: 1-D load and unload test

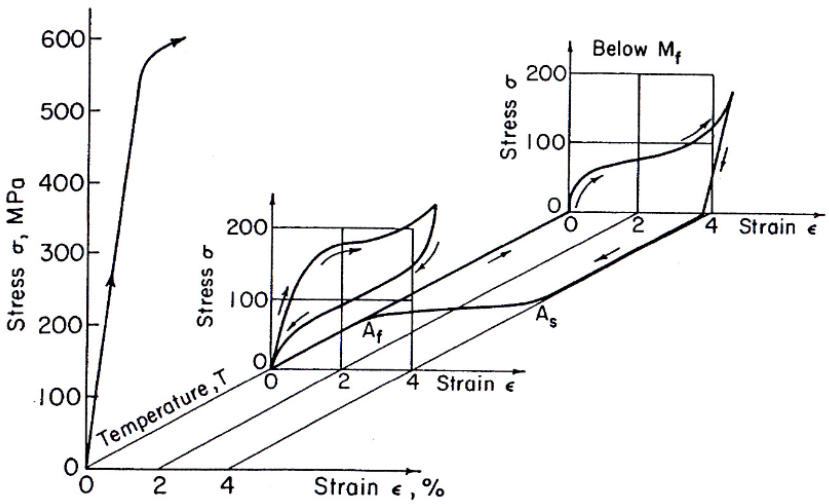

Figure 1.14: Relations between temperature, stress and strain in SMA

1.3 Applications

The most classical application of SMA is in biomedical field, especially in orthodontics, vascular surgery and orthopedy: as in these fields a great added value is supposed to exist, SMA managed to spread even when their cost were much higher than now. Pseudo-elasticity was the main effect used: thanks to it biomedical instruments were able to be subjected to large strain rate without kinking and damaging soft tissues; examples of these application are biopsy forceps (fig.1.15(d)) able to bending with small radius without kink, guide wires (fig.1.15(b)) that don't kink even in winding vascular paths, kidney stone graspers (fig.1.15(c)) and stents used in vascular surgery (fig.1.15(a)). In the last years, SMA have been largely employed in the design of robotic arms used in automatic surgery

SMA are also usually used in common devices that are supposed to resist hurts without any damaging, i.e. glasses can remain in elastic state even when subjected to large strain thanks to PE (fig.1.16(a)) or can recover the original shape if they

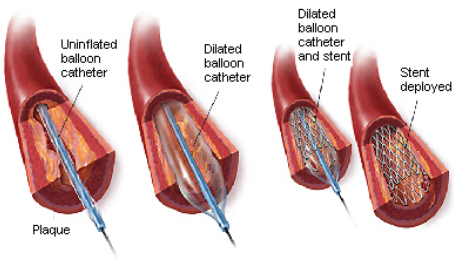

(a) Stents

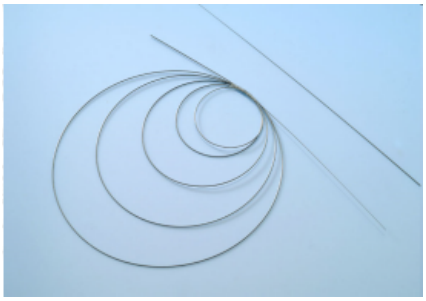

(b) Guide wires

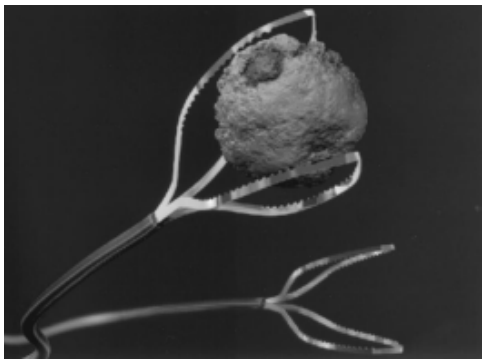

(c) Kidney stone gaspers

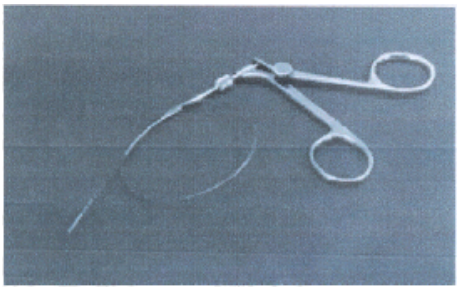

(d) Biopsy forceps

Figure 1.15: Examples of biomedical applications of SMA

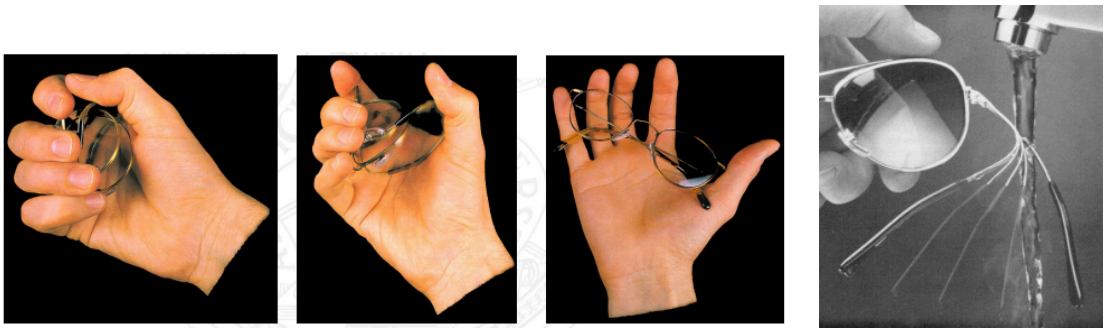

(a) PE application in glasses production

(b) SME application in glasses production

Figure 1.16: Example of SMA glasses advantages

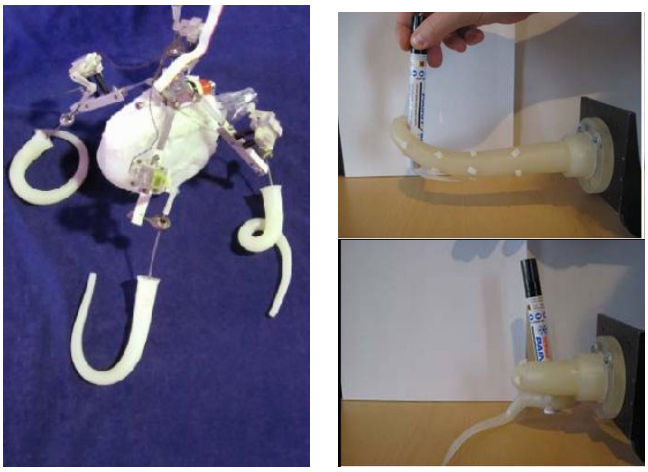

(a) (b)

Figure 1.17: Robotic Octopus by Scuola superiore Sant'Anna

had been damaged when heated thanks to SME (fig.1.16(b)).

In addition to biomedical field, SMA are commonly used in mechanics. SMA wires and actuators are widely employed in robotics, e.g. in "Scuola superiore Sant'Anna" a totally automatic octopus robotic arm (fig.1.17) has been built. SMA are also used in the manufacture of thermal machines, opening and closure systems and actuators of any type; in particular, cars include a large amount of applications of SMA, as shown in figure 1.18.

Finally, civil engineering is one of the last, in term of date, fields of application of SMA. Pseudo-elasticity is employed in structural elements e.g. seismic insulators (fig.1.19(a)), beam-colums connectors (fig.1.19(b)), dampers and energy dissipation

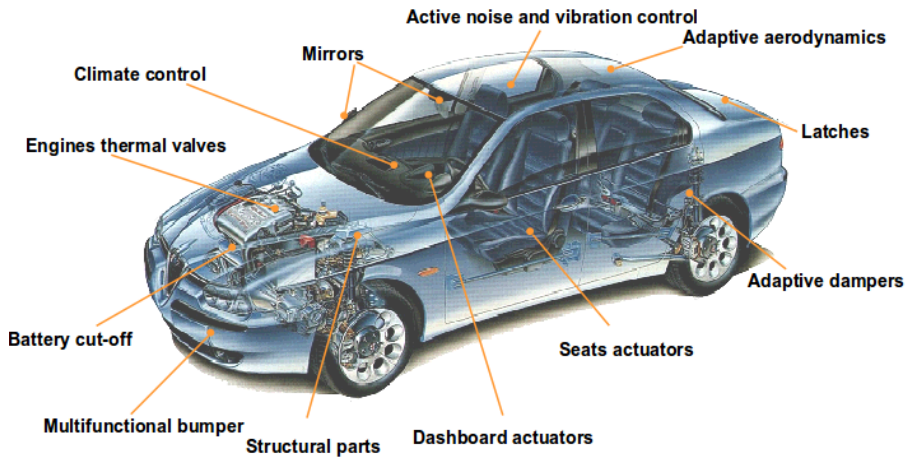

Figure 1.18: SMA applications in car construction - Courtesy of F. Butera, Saes Getters S.P.A.

systems (fig.1.19(c)), while SME is usually used in plant design (photovoltaic, gas planting et cetera) or even in elements which replace blasting in rock fracturing (fig.1.19(d)).

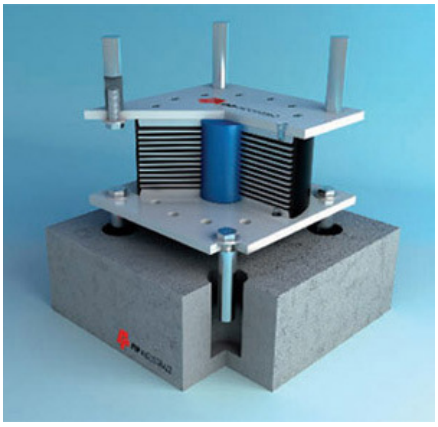

(a) Seismic isulators

(b) Beam-colums connectors

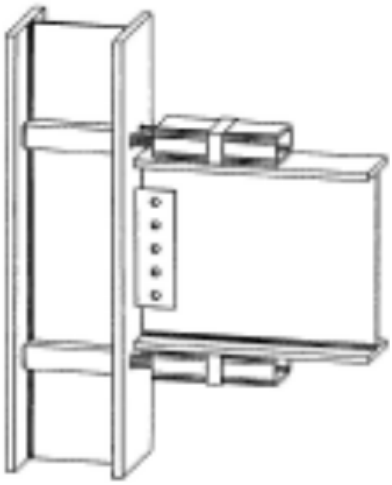

(c) Energy dissipation systems - dampers

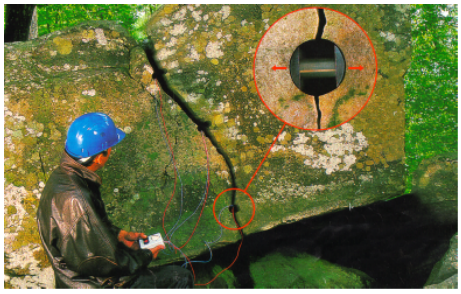

(d) Rock fracturing using SMA elements

Figure 1.19: Examples of biomedical applications of SMA

Chapter 2

Overview on actuators' mechanisms and design

As introduced in the previous chapter, smart materials are able to recognize external stimuli and react accordingly to them. This ability lead them to be designed more in base of this feature than in base of their classical mechanical characteristics. On one hand, these materials can be designed so that they react accordingly to exercise mechanical situation (as stress/strain imposed) and produce a reaction based on the magnitude of external stimuli which can be translated in an electrical signal; this particular function defines the so-called *sensor* mechanism, which translates a mechanical input to an electrical output and allows to control the exercise environment. On the other hand, intelligent materials' features can be used contrariwise as *actuators*: from an electrical, chemical or thermal input they can produce a mechanical work in terms of motion and forces. The above described distinction is schematically shown in fig.2.1.

Shape memory alloys are widely used in the field of actuators as they are able to produce great forces and displacement (as discussed in section 1.2) within a small volume. In this chapter, an overview on different types of actuators and design approaches will be presented.

SMA actuators are included in the general definition of actuators (fig.2.2): the common feature of actuators is transforming a particular source of energy in mechanical work; in particular, SMA actuators transform thermal energy in mechanical work. Basically, it is possible to obtain by controlling the temperature of the mechanism, a certain response in terms of displacements can be obtained; the variation of temperature which produces the phase transformation and the consequent deformation is called "*actuation*".

The main issue in actuation is that, while heating phase can be quasi-instantaneous, the reversal transformation due to cooling takes more time; this difficulty is due to the fact that there are no cheap technologies able to decrease temperature quickly,

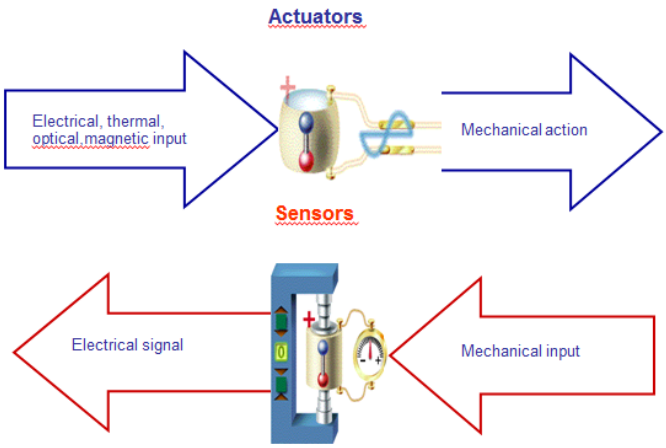

Figure 2.1: Schematization of the difference between sensors and actuators

Actuators

To / From	Electrical	Magnetic	Mechanical	Thermal	Chemical	Radiative
Electrical		Ampere's Law	Electrostatics, Piezoelectricity	Resistive Heating	Electrolysis, Ionization	EM Transmission
Magnetic	Hall Effect, Mag. Resistance		Magnetostatics, Magnetostriction	Eddy Currents Hysteretic Loss	Magnetic Separation	Magneto-optics
Mechanical	Piezoresistance, Piezoelectricity	Magnetostriction	Pneumatic, Hydraulic	Friction	Phase Change	Tribo-luminescence
Thermal	Thermoelectric	Curie Point	Expansion, SMA, Phase Change		Reaction Rate, Ignition	Thermal Radiation
Chemical	Electrochemical Potential	Chemomagnetic	Combustion	Exo/Endothermic Reaction		Chemo luminescence
Radiative	Photoconductivity, EM Recovering	Magneto optics	Radiation Hardening	Photothermal	Photochemical	

Figure 2.2: Categories of actuators

in fact the cooling process is usually performed by natural convection. In addition to this, also the heating phase presents some problems i.e, in many cases the exercise environment's temperature is not easy to control or there is not space enough to install necessary instruments to control the temperature. Given these issues electrical actuation is preferred to thermal one in the majority of applications. In particular electric current gets induced in the SMA element which works as an electrical resistance and, accordingly to Joule effect, produces heat, increasing the temperature of the element itself. This kind of actuation based on a electrically induced transformation is field of research; in this work it has been modelled as an equivalent thermal actuation considering the temperature variation produced by electricity.

2.1 Type of actuation

The typical electrical actuated actuator mechanism is outlined in fig.2.3. In this example the wire gets deformed at low temperature (martensite phase) by an external load; when the electrical circuit is closed, current flows through the wire, increasing its temperature and inducing direct transformation (from martensite to austenite phase), so that the wire recovers its original configuration thanks to shape memory effect.

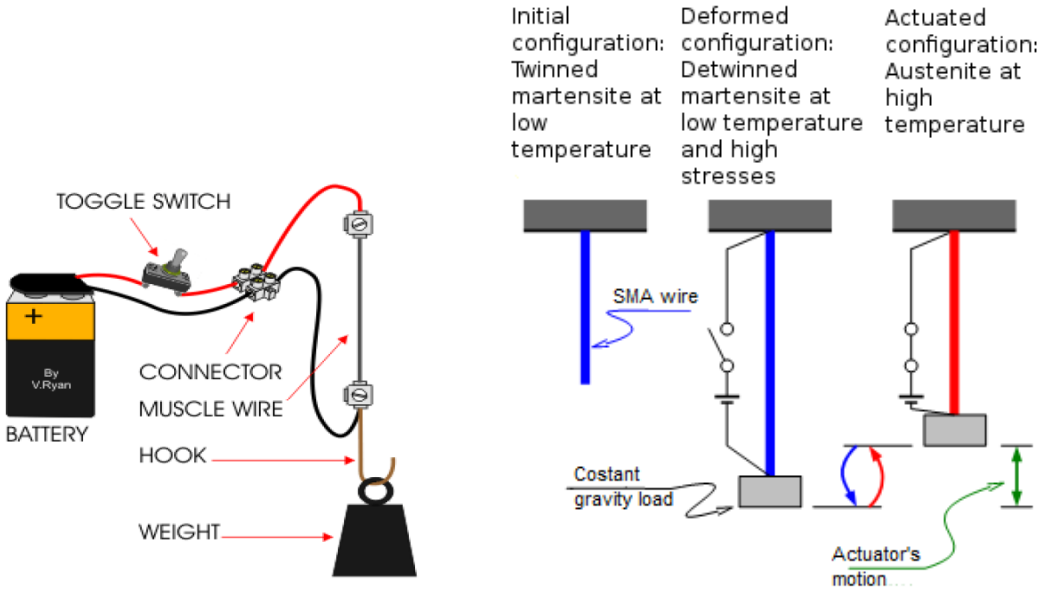

(a) Electrical circuit schematization for a simple electrically actuated SMA wire;

(b) Behaviour of a SMA wire actuator;

Figure 2.3: Schematization of a SMA-wire based actuator

2.2 Recovering system

For one-way shape memory effect, this mechanism is not repeatable because, when the inverse transformation is performed (by decreasing temperature), the deformation is constant. In order to get actuator's mechanism repeatable, an external load called "*bias*" is needed e.g. in the case in figure 2.3 the external gravity load works as bias because re-deforms the wire when the temperature decreases and inverse transformation occurs. From this point of view another possible distinction between

SMA actuators can be performed in base of how it returns the original configuration after the actuation. As shown in fig.2.4 actuators can be distinguished in:

- *One-way actuators*: whenever the transformation is performed and the original shape is recovered, they maintain the shape independently from the temperature
- *Biased actuators*: they are the most common actuators: a elastic element is disposed next to the SMA one. This elements (outlined in the figure as a spring) is the bias element which deforms the SMA element whenever the inverse transformation occurs until it recovers the shape it had before the direct transformation
- *Two-way actuators*: two SMA elements are arranged so that they work oppositely: the direct transformation of the first works as a "bias" by deforming the second and vice-versa; these actuators have the great advantage that by working on both elements it is possible to achieve intermediate configurations, whereas in the others actuators only two configurations were possible (correspondent to the two phases of the SMA element).

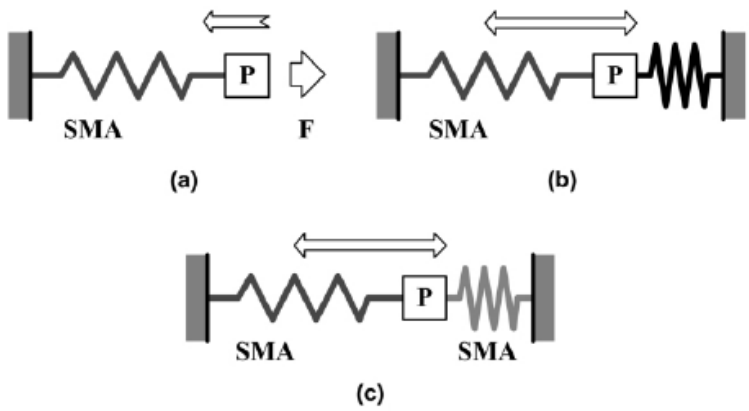

Figure 2.4: Categories of actuators based on recovery system: (a) One-way actuators (b) Biased actuators (c) Two-way actuators

2.3 Type of motion produced

Actuators can be identified also through the motion they produce; so far *linear actuators* have been discussed (fig.2.5a), but also angular displacements can be produced (fig.2.5b).

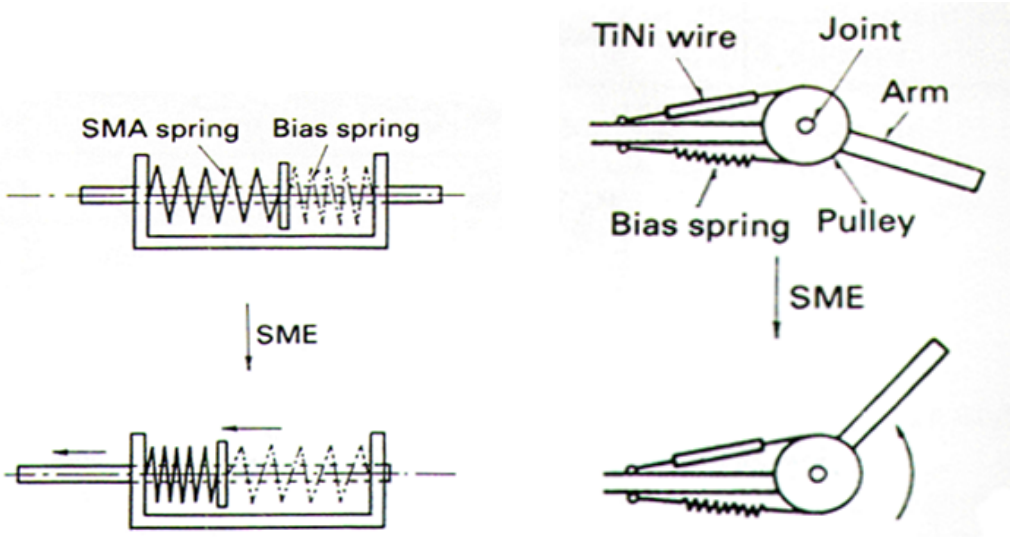

(a) Linear actuators mechanism (b) Angular actuators mechanism

Figure 2.5: Types of displacements produced by actuators

It is important to stress that both categories are composed by combination of wire and spring SMA elements; even complicated mechanisms (e.g. fig.2.6) can be manufactured only by using wires and spring, providing a great advantage in simplicity. Most of commercial actuators are starting from these basic components and for this reason thesis consider only spring and wire elements.

The simplicity is the great feature of SMA actuators i.e. as seen in fig.2.7, classic actuators need bulky engines, transformators and mobile parts to produce motion from electrical input. Consequently a large amount of volume were needed; in addition too many mobile parts imply high probabilities of exercise damages and low robustness. Conversely, SMA actuators can do the same work without mobile parts and requesting a small volume. In fact the complexity of the mechanism is avoided by the specific design of the material itself.

2.4 Design of actuators

For the aforementioned reasons the actuator design is a complex procedure: SMA element must be designed in geometry and material, as well as the bias; in addition the electric circuit must be designed and, if necessary, also a control system must be predisposed. Because of this complexity, simplified constitutive models are usually used since the model has a little effect on the outcome if compared to other elements such as control system.

For example SMA behaviour can be modelled as linear elastic by distinguish elastic

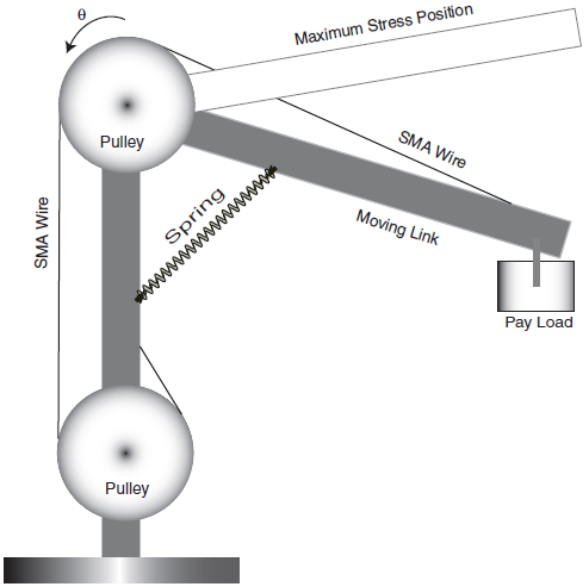

Figure 2.6: Example of actuated robotic arm

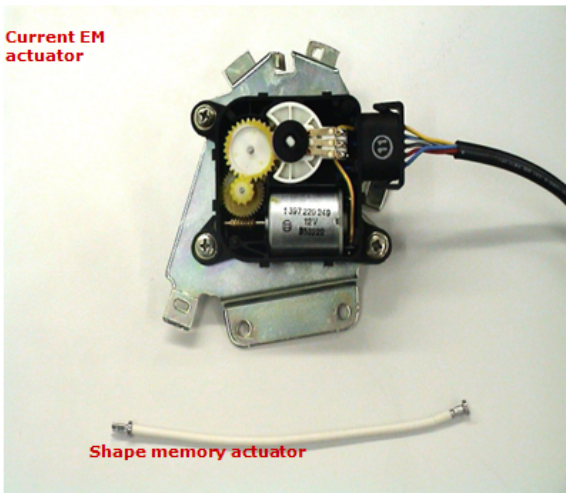

Figure 2.7: Example of simplification due to the use of SMA actuators

parameters in austenite and martensite phases, as seen in fig.2.8. This assumption results very inaccurate to model the general behaviour, but is acceptable if the element works in the first section of the $\sigma - \varepsilon$ graph.

For classic linear biased actuator (fig.2.5a), the mechanical study of the actuator can be done through graph 2.9 where the black curve is the response of elastic spring while the red and blue ones are the austenite and martensite responses re-

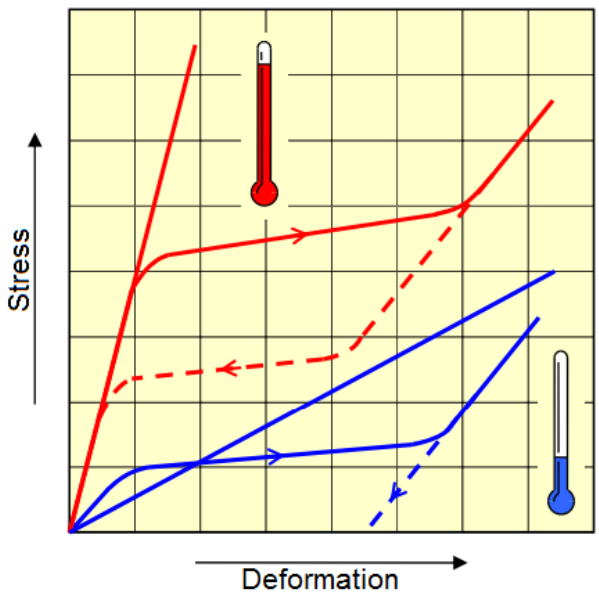

Figure 2.8: Simplified constitutive model for actuators

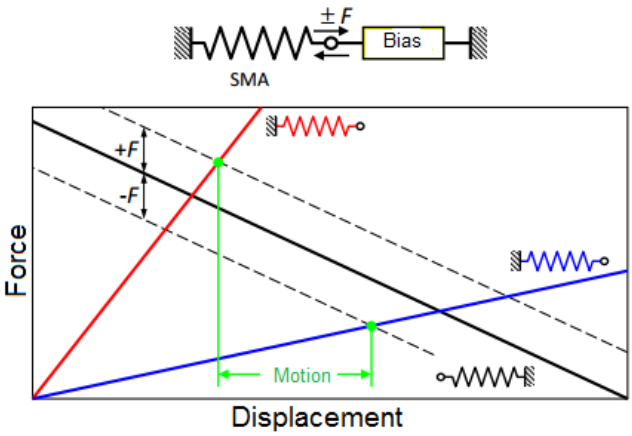

Figure 2.9: Simplified constitutive model for actuators mechanisms

spectively. In part 2 a different approach will be adopted: numerical simulations of actuators will be performed in support to the design; these simulations will use more sophisticated constitutive models in order to show that simulations can offer many advantages without a too large effort in time and calculus.
An example of a real actuator is reported in figure 2.10; the element gets actuated by the heat coming from the water flow: this leads to a variation in temperature of

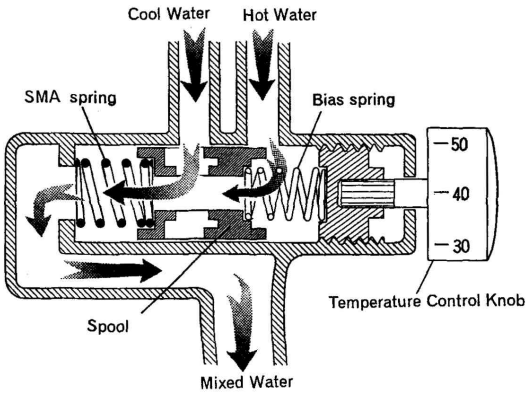

Figure 2.10: Example of a real actuator

the SMA spring, inducing the transformation. The design aims at reaching an equilibrium state between the SMA spring and the bias, in order to control the incoming flows of hot and cool water and the temperature of the output flow. This kind of actuator is used in several thermal machines e.g. coffee boiling systems (fig.2.10).

Chapter 3

Constitutive models for SMA

Several models have been proposed since SMA have spread in market; the choice of which model use depend on the type of the object is supposed to be designed. For the design of actuators (as discussed in chapter 2) or complex mechanisms, simple models are preferred: models defined by 2/4 parameters which are not able to predict both superelasticity and shape memory effect; for example, an empirical, widely used model supposes martensite and austenite as linear elastic phases, separated by an instant transformation at a certain reference temperature. These models are acceptable whenever the working environment and the kind of transformation are known a priori and the SMA element works in a very standard way. Although the ability of these models to catch the complex phenomena related to SMA is very limited, which affects the possibility to fully exploit the potential of these materials. Since the main issue in the design of any mechanical element based on SMA is the design of the alloy more than the mechanism itself, the formulation of more sophisticated constitutive models were needed; in addition the most common applications of these models, e.g. stents or tendons, involve very complex geometries, analytical models are no more sufficient and numerical methods, typically based on the finite elements method (FEM), are supposed to be derived.
In this work I want to show how the use of numerical simulations based on sophisticated constitutive models manage to support effectively the design process without involving too much effort in terms of time. This chapter includes the description of the two SMA constitutive models adopted in this work. In particular, the Auricchio-Petrini model [4], i.e., a constitutive model able to reproduce both PE and SME, and Auricchio-Taylor model [5], which represents the built-in model for PE in many FEM commercial solvers such as Abaqus, Ansys et cetera.

3.1 Auricchio-Petrini constitutive model

This model aims at reproducing both PE and SME features of SMA; it is based on a more classical model proposed by Souza [6] in 1998, by adding some features e.g. regulation norm, discussed in the following sections.

3.1.1 Time-continuous model

The model assumes the strain, ε, and the absolute temperature, T , as control variables and the second-order transformation strain tensor, ε^{tr} , as internal variable. The quantity ε^{tr} has the role of describing the strain associated to the phase transformations; moreover, it is assumed to be traceless, following experimental evidences [7] indicating no volume changes during phase transition. Moreover, indicating with ε_L the maximum transformation strain reached at the end of the transformation during an uniaxial test, it is required that:

$$0 \leq ||\varepsilon^{tr}|| \leq \varepsilon_L \tag{3.1}$$

where ε_L can be regarded as a material parameter.
Assuming a small strain regime, the free energy function Ψ for a polycrystalline SMA material is expressed through the following convex potential:

$$\Psi(\varepsilon, e^{tr}, T) = \Psi_{el} + \Psi_{ch} + \Psi_{tr} + \Psi_{id} + F_{\varepsilon_L}(e^{tr}) \tag{3.2}$$

where:

- the elastic strain energy Ψ_{el}, due to the thermo-elastic material deformation, is set equal to:

$$\Psi_{el} = \frac{1}{2}K\Theta^2 + G||e - e^{tr}||^2 - 3\alpha K\Theta(T - T_0) \tag{3.3}$$

  with K the bulk modulus, G the shear modulus, α the thermal expansion coefficient, T_0 a reference temperature, e and Θ respectively the deviatoric and volumetric components of the total strain;

- the chemical energy Ψ_{ch}, due to the thermally-induced martensitic transformation, is set equal to:

$$\Psi_{ch} = \beta\langle T - M_f\rangle||e^{tr}|| \tag{3.4}$$

  with β a material parameter related to the dependence of the critical stress on the temperature and $\langle\bullet\rangle$ the positive part of the argument;

- the transformation strain energy Ψ_{tr} , due to the transformation-induced hardening, is set equal to:

$$\Psi_{tr} = \frac{1}{2}h||e^{tr}||^2 \tag{3.5}$$

with h a material parameter defining the slope of the linear stress-transformation strain relation in the uni-axial case;

- the free energy Ψ_{id}, due to the change in temperature with respect to the reference state ($T = T_0$) in a incompressible ideal solid, is set equal to:

$$\Psi_{id}(u_0, T\eta_0) + c\left[(T - T_0) - Tln\frac{T}{T_0}\right] \tag{3.6}$$

with c the heat capacity, u_0 and η_0 the internal energy and the entropy at the reference state, respectively;

- $F_{\varepsilon_L}(e^{tr})$ is set equal to an indicator function introduced to satisfy the constraint on the transformation strain norm:

$$F_{\varepsilon_L}(e^{tr}) = \begin{cases} 0 & if\ ||e^{tr}|| \leq \varepsilon_L \\ +\infty & if\ ||e^{tr}|| \geq \varepsilon_L \end{cases} \tag{3.7}$$

It is remarkable that the expression of the energy in equation 3.2 is the same as classical thermodynamic theory, with the addition of two terms strictly related to SMA features: Ψ_{ch} and F_{el}. Herein, simplifying hypothesis are adopted: thermal capacity, conductivity and expansion are neglected as they slightly affect the problems considered in this thesis; therefore the whole Ψ_{id} 3.6 and the second addend of 3.3 are set to zero.
Constitutive equations can now be derived:

$$\begin{cases} p = \dfrac{\partial \Psi}{\partial \Theta} = K\Theta \\ \\ s = \dfrac{\partial \Psi}{\partial e} = 2G(e - e^{tr}) \\ \\ \eta = -\dfrac{\partial \Psi}{\partial T} = -\beta||e^{tr}||\dfrac{\langle T - M_f\rangle}{|T - M_f|} \\ \\ \mathbf{X} = -\dfrac{\partial \Psi}{\partial e^{tr}} = s - \left[\beta\langle T - M_f\rangle + h||e^{tr}|| + \dfrac{F_{\varepsilon_L}(e^{tr})}{\partial||e^{tr}||}\right]\dfrac{\partial||e^{tr}||}{\partial e^{tr}} =: s - \alpha \end{cases} \tag{3.8}$$

where: p and s are, respectively, the volumetric and the deviatoric part of the stress σ; η is the entropy and α is the back-stress by classical plasticity; $\mathbf{X}$ is the thermodynamic force associated to the transformation strain and indicated in the following as *transformation stress*. The subdifferential of the indicator function results:

$$\frac{F_{\varepsilon_L}(e^{tr})}{\partial||e^{tr}||} = \begin{cases} 0 & if\ ||e^{tr}|| < \varepsilon_L \\ +R & if\ ||e^{tr}|| = \varepsilon_L \\ - & if\ ||e^{tr}|| > \varepsilon_L \end{cases} \tag{3.9}$$

The tensor α plays a role similar to the so-called *back-stress* in classical plasticity and $\mathbf{X}$ can be identified as a *relative stress*. Moreover, in eq.$(3.8)_4$ the terms $\beta\langle T - M_f\rangle$ and $h||e^{tr}||$ describe, respectively, a piecewise linear dependency of α on the temperature and a linear hardening behaviour proportional to $||e^{tr}||$ during the phase transformation.
The model gets completed by the introduction of the associative evolution law for e^{tr}; Kuhn Tucker conditions are provide a realistic model for SMA features:

$$\dot{e}^{tr} = \dot{\zeta}\frac{\partial F(\mathbf{X})}{\partial \sigma} \tag{3.10}$$

with:

$$\dot{\zeta} \geq 0, \quad F \leq 0, \quad \dot{\zeta}F = 0$$

Numerous tests show an asymmetric behaviour of SMA in tension and compression [7] and suggest to describe SMA as an isotropic material with a Prager-Lode type limit surface [8][9]. Accordingly Auricchio-Petrini assume a yield function defined as:

$$F(\mathbf{X}) = ||\mathbf{X}|| - R = \sqrt{2J_2} + m\frac{J_3}{J_2} - R \tag{3.11}$$

where R is the radius of the elastic domain in the deviatoric space, m is a material parameter with $m \leq 0.46$ to guarantee the limit surface convexity[10], J_2 and J_3 are the second and the third invariants of the deviatoric tensor $\mathbf{X}$, defined, respectively, as:

$$J_2 = \frac{1}{2}(\mathbf{X}^2 : \mathbf{1}), \qquad J_3 = \frac{1}{3}(\mathbf{X}^3 : \mathbf{1})$$

In the model implemented in Abaqus, R has been set as a constant, while m has been calculated as:

$$m = \sqrt{\frac{27}{2}}\frac{\sigma_c - \sigma_t}{\sigma_c + \sigma_t} \tag{3.12}$$

3.1.2 Time-discrete integration algorithm

In addition to the time-continuous model, Auricchio-Petrini[4] also proposes a solution algorithm suitable for FEM implementation. The scheme, summarized in flowchart 3.13-3.14, is based on the classical elastic-predictor inelastic-corrector procedure used in classical plasticity: the problem gets time discretized by an implicit eulerian scheme and an elastic evolution in the current loading step is supposed to occur. After that, a check is done in order to evaluate admissibility of the current elastic state: if the check resulted negative, the internal variable e^{tr} is updated and the real stress-strain magnitudes are computed. For the sake of simplicity, in flowchart 3.13-3.14 all the variables evaluated at the current time step are signed without subscription, e.g. $e^{tr} = e^{tr}_{t_{n+1}}$, and the variables at the previous time step are signed with the subscription "n", e.g. $e^{tr}_n = e^{tr}_{t_n}$.

TIME – DISCRETE MODEL

1. Compute trial state

$$\begin{cases} e^{tr,TR} = e^{tr}_n \\ S^{TR} = 2G(e - e^{tr,TR}) \end{cases}$$

2. Check material state

$$\begin{cases} compute: & \begin{cases} \alpha^{tr} = \left[\beta\langle T - M_f\rangle + h||e^{tr}|| + \dfrac{F_{\varepsilon_L}(e^{tr})}{\partial||e^{tr}||}\right]\dfrac{\partial||e^{tr}||}{\partial e^{tr}} \\ \mathbf{X}^{TR} = s^{TR} - \alpha TR \\ F(\mathbf{X}) = \sqrt{2J_2} + m\dfrac{J_3}{J_2} - \mathbf{R} \end{cases} \\ check\ F^{TR}: & \begin{cases} if \quad (F^{TR} < 0) \quad then & \textbf{elastic step}\ (EL) \\ else & \textbf{active} \quad \textbf{p.t.}\ (PT_1) \\ endif \end{cases} \end{cases} \tag{3.13}$$

3. Update material state

$$
\begin{cases}
if \quad (CASE\ EL\ -\ Elastic\ step) \quad then: \\
\qquad \begin{cases} e^{tr} &= e^{tr,TR} \\ s &= 2G(e - e^{tr}) \end{cases} \\
else\ if \quad (CASE\ PT1\ -\ Evolving\ phase\ trnsformation) \quad then \\
\qquad \begin{cases} find\ e^{tr} \\ check\ solution: \quad \begin{cases} if\ \overline{||e^{tr}||} < \varepsilon_L\ then \quad exit \\ else \qquad\qquad\qquad CASE\ PT2 \\ end\ if \end{cases} \end{cases} \\
\qquad if\ (CASE\ PT2\ -\ Saturated\ phase\ transformation)\ then \\
\qquad\quad find\ e^{tr} \\
\qquad end\ if \\
end\ if
\end{cases}
\tag{3.14}
$$

From a computational standpoint, the time-discrete model as presented above shows a major problem, since the transformation stress $\mathbf{X}$ depends on the derivative of the transformation strain as shown in eq.3.8 which can be null making the derivative undefined. To overcome this difficulty different approaches can be followed. Herein, Auricchio-Petrini proposes to substitute the Euclidean norm $||\varepsilon^{tr}||$ with the regularized norm $\overline{||\varepsilon^{tr}||}$, defined as:

$$
\overline{||e^{tr}||} = ||e^{tr}|| - \frac{\delta^{(\delta+1)/\delta}}{\delta - 1}(||e^{tr} + \delta)^{(\delta-1)/\delta} \tag{3.15}
$$

where δ is a user-defined parameter which controls the smoothness of the regularized norm. In the implementation used for the analysis, a difference from original Auricchio-Petrini algorithm has been introduced, since the regularized norm has been calculated as:

$$
\overline{||e^{tr}||} = ||e^{tr} + \Delta|| = \sqrt{trace(e^{tr}e^{tr} + \Delta)} \tag{3.16}
$$

where $\Delta \approx 10^{-6}$ is a regularization factor whose magnitude is chosen so that it doesn't affect calculus whenever $e^{tr} >> 0$ and avoids that the derivate of the transformation strain becomes undefined whenever $e^{tr} \to 0$. It is remarkable that the model doesn't reproduce a full strain recovering under cyclic loading because of the presence of the regularized norm coefficient which is an additional term in the calculation of strain and cannot be recovered.

Numerical simulations, design and prototyping of a SMA-based actuator

Chapter 4

Study of the convergence of a elastic-plastic spring

As already discussed in chapter 2, the main elements which compose commercial SMA actuators are springs and wires; while wires have a simple geometry and they are analyzed as slender cylinders, springs show a more complex behaviour. The quality of the analysis strongly depends on the quality of discretization because some meshes are more likely to catch local resistance mechanisms than others.
This chapter aims at finding an optimal mesh for a spring element in order to perform simulations which produce engineering-rate accurate results in a time reasonably short according to producers design duration.

4.1 Problem description

The object of the analysis is the spring reported in fig.4.1. The wire which composes the spring has a radius $r_0 = 10,35\,cm$, the coils step is $\beta = 4,2\,cm$ and the global diameter of the spring is $\phi = 1,85\,mm$. In order to prevent the analysis from being affected by errors, the classic uniaxial tensile test has been taken in consideration so that contact phenomena, which could occur in compression tests, is neglected. It has also been neglected the attachment of the spring to the test machine: it has therefore chosen to focus the analysis on two and half coils taken from the middle of the spring; this choice is due to the fact that the global behaviour of the spring can be obtained as sum of many modules and a local solution near the attachments.

4.2 Material

Since the goal of the simulations on spring is to analyze the dependence of results on mesh, an elastic-perfectly plastic constitutive model has been chosen; the model

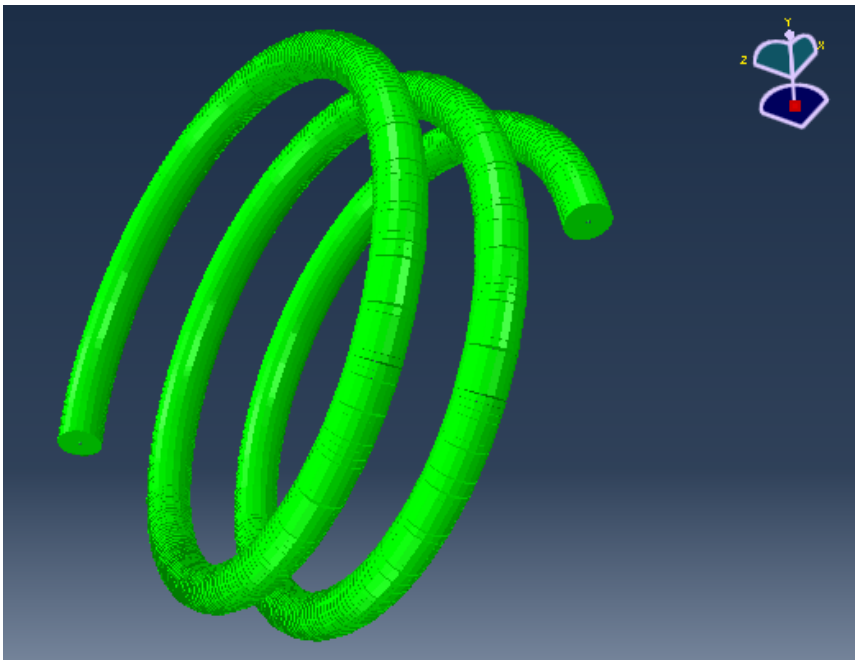

Figure 4.1: Geometry of the spring implemented in Abaqus

used is the built-in model in Abaqus, which is based on the classical Von Mises plastic criterion [11] with isotropic hardening. Experimental data have been taken from a real tensile test found in literature [12] and they are summarized in tab.4.1 and fig.4.2. Since the current study wants to investigate the spring behaviour under working conditions and not to catch failure mechanisms, an unrealistic strain value was added in tab.4.1 in order to extend plastic plateau and don't concern about strain imposed in simulations.

For the elastic phase, Abaqus expects Young Modulus and Poisson Coefficient to

Table 4.1: Experimental data of a tensile test on a steel sample

Nominal stress [Pa]	Nominal Strain
0.00E+00	0.00E+00
2.00E+08	9.50E-04
2.40E+08	2.50E-02
2.80E+08	5.00E-02
3.40E+08	1.00E-01
3.80E+08	1.50E-01
4.00E+08	2.00E-01
4.00E+08	8.00E-01

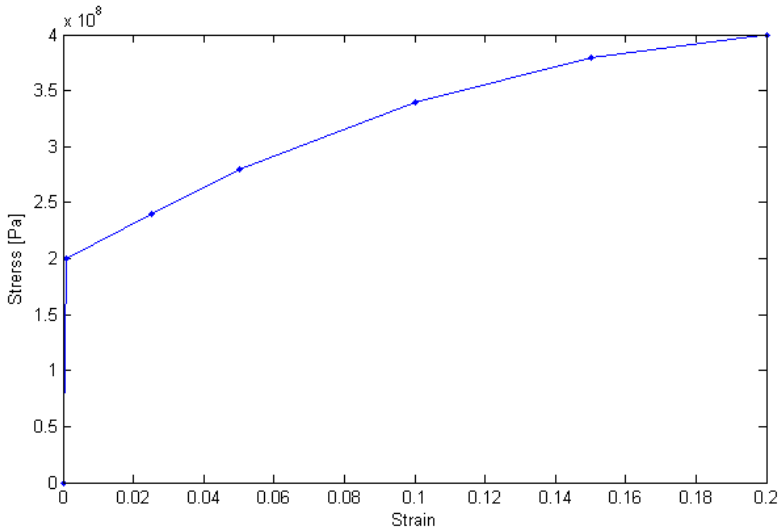

Figure 4.2: $\sigma - \varepsilon$ curve for a tensile test on a steel sample

be entered. The first was calculated as the slope defined by the first point of fig.4.2, and results to be $E \simeq 210GPa$; the latter one was hypothesized to be $\nu \simeq 0,33$, the most common magnitude for steel.
For plastic model implementation in Abaqus a load pattern in terms of *true stress* and *plastic strain*: since the experimental data were given in terms of *nominal* stress and strain, true stress and plastic strain must be calculated from the previous ones as:

- $\sigma_{tru} = \sigma_{nom}(1 + \varepsilon_{nom})$ to convert the nominal stress to true stress
- $\varepsilon_{tru} = ln(1 + \varepsilon_{nom})$ to convert the nominal strain to true strain
- $\varepsilon_{pl} = \varepsilon_{tru} - \dfrac{\sigma_{tru}}{E}$

By these steps, Abaqus input get calculated and it is reported in tab.4.2.

4.3 Mesh

Given the comparative nature of this work, different combinations of element formulations and mesh generation are considered.

- bricks elements with reduced integration (element C3D8R in Abaqus libraries) using an automatic mesh generation algorithm implemented in Abaqus

Table 4.2: Add caption

Nominal stress [Pa]	Nominal Strain	True Stress [Pa]	True Strain	Plastic Strain
0.00E+00	0.00E+00	0.00E+00	0.00E+00	0.00E+00
2.00E+08	9.50E-04	2.00E+08	9.50E-04	0.00E+00
2.40E+08	2.50E-02	2.46E+08	2.47E-02	2.35E-02
2.80E+08	5.00E-02	2.94E+08	4.88E-02	4.74E-02
3.40E+08	1.00E-01	3.74E+08	9.53E-02	9.35E-02
3.80E+08	1.50E-01	4.37E+08	1.40E-01	1.38E-01
4.00E+08	2.00E-01	4.80E+08	1.82E-01	1.80E-01
4.00E+08	8.00E-01	7.20E+08	5.88E-01	5.84E-01

- linear triangular prism wedge elements (element C3D6 in Abaqus libraries) using an automatic mesh generation algorithm implemented in Abaqus
- bricks elements with reduced integration (element C3D8R in Abaqus libraries) using a mesh algorithm implemented in Matlab by "Computational Mechanics and Advanced Materials Group" [15], University of Pavia
- linear beam elements (element B31 in Abaqus libraries) using an automatic mesh generation algorithm implemented in Abaqus
- quadratic beam elements (element B32 in Abaqus libraries) using an automatic mesh generation algorithm implemented in Abaqus

For each of the aforementioned meshes, a convergence study has been performed by increasing the number of elements used in the analysis.

4.3.1 Automatic Abaqus mesh generation: cube and tetrahedral elements

The first mesh generation algorithm uses the classic "brick" elements: 8 nodes and 24 degrees of freedom per element, while the second one uses 6-node linear triangular prism elements: 6 nodes and 18 degrees of freedom per element. The arrangement of the elements along the spring and across the section is based on a default Abaqus algorithm.
First of all, user is supposed to *seed* the part to be meshed: this means to set a number of points across the structure which approximate the analytical geometry and work as basis and reference points for the construction of the mesh. The seeding process depend on three parameters::

- *approximate global size* which is a measure of the length of each element: considering cube elements, cube's edge is supposed to be a significant equivalent

dimension of the element. This coefficient is the coefficient which mainly rules the discretization along the spring axis

- *curvature control* which is set through a *maximum deviation factor*; maximum deviation factor is a measure of the magnitude, in percent, of the deviation between the edges of two adjacent elements. From this parameter it is possible to calculate another important parameter for the current analysis: the number of elements used to approximate a circle and, consequently, the quality of the mesh across the section of the spring

- *minimun size control* which is an approximate measure of the minimum dimension of elements, set as percent of the global size or through a global length

After the seeding process, the mesh can be defined. Abaqus has two main families of mesh generation algorithms for hexaedral elements: *structured* meshes and *sweep* meshes. Structured meshes works for regular geometries: the software uses default optimized meshes known for standard shapes, e.g. triangles, squares, cubes *et cetera* and map them to the geometry; this kind of mesh is highly efficient as produce no distorted elements respecting both geometry and seeding of the model. On the contrary, sweep starts from a face of the geometry and tries to mesh it in plane in a structured way; once meshed the face, the algorithm try to reproduce it modularly till reaches geometry's edges. In the current work, sweep mesh was used because gripper's shape wasn't regular enough to perform structured meshes. Hence the mesh generation algorithm has to be chosen. Abaqus has two default algorithms:

- *medial axis* algorithm which strictly follows the seeding, but produce a bad approximation of structure's edges. This algorithm is useful whenever the user needs to control directly the arrangement of mesh elements;

- *advancing front* algorithm has the main purpose of producing a as better as possible approximation of structure's edges, even by neglecting seeds. This algorithm produces a good mesh in terms of geometry approximation, but doesn't avoid the production of highly distorted elements, whose presence could invalidate the analysis.

Two example of the mesh produced by the above-described algorithm is shown in fig.4.3. Since in this work no joints were considered, there were no need to strictly respect seeding, so advancing front algorithm had been chosen; by this choice it had been possible to better catch boundary torsional phenomena, which are widely significant for resistance mechanisms in springs and take place close to the edges.

In tab.4.3 and tab.4.4 the analysis performed are reported, including the correspondent coefficients and number of elements of the mesh.

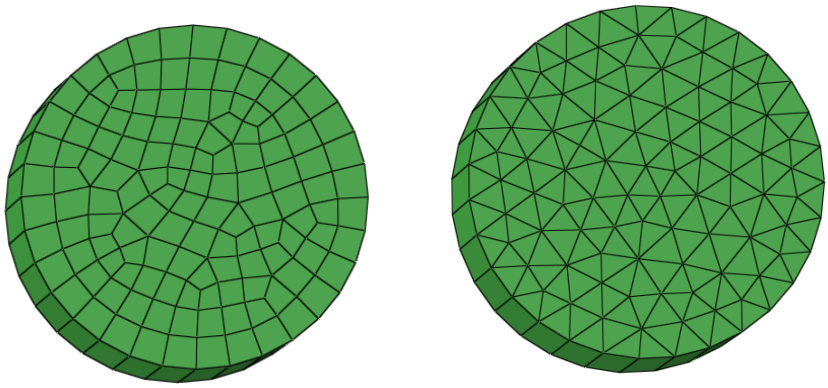

(a) Spring's cross section meshed by "brick" elements

(b) Spring's cross section meshed by tetrahedral elements

Figure 4.3: Meshes created by Abaqus default mesh generation algorithm

Table 4.3: Spring test report: parameters for default Abaqus mesh generation algorithm using "brick" elements

Test	App. global size	Curvature control	Elements per circle	Total elements
1	2.4	0.1	8	288
2	1.2	0.05	16	5700
3	0.6	0.025	32	37926
4	0.3	0.0125	64	271458
5	0.8	0.0333	24	14652
6	1.6	0.0666	12	1944

Table 4.4: Spring test report: parameters for default Abaqus mesh generation algorithm using tetrahedral elements

Test	app. global size	curvature control	Total elements
1	2.4	0.1	864
2	1.2	0.05	6300
3	0.6	0.025	53214
4	0.3	0.0125	431838
5	2	0.0833	1170
6	1.6	0.0666	1836

4.3.2 Compmech mesh

Compmech mesh generation algorithm uses the classic "brick" elements: 9 nodes and 27 degrees of freedom per element. Elements arrangement along the spring and across the section is based on the tough that spring can be subdivided in two

different parts which correspond to different resistance mechanisms:

- the "*core*", which is the part of the spring closest to the spring axis and it is supposed to react manly by bending. As it is a 1-D element longitudinal to the axis, the most influence parameter to mesh this part is the number of subdivisions along the axis itself
- the "*boundary layer*", which is the external part of the cross section. It is supposed to react torsionally, developing local torsional moments. This part is mainly influenced by the quality of the mesh across the section.

In order to better understand the compech mesh generation algorithm, in fig.4.4 an example of cross section is proposed. It is recognizable the core, at the centre of the circle, meshed orthogonally; external to it a change of mesh occurs: the elements which compose the boundary layer have different dimensions (as they are ruled by different parameters from the core mesh) and they are meshed in a polar system in order to better catch torsional phenomena.

The Matlab code, first of all, builds the axis of the spring by the parameter n_{coil} which is the number of linear segments used to describe a single coil; similarly to n_{coil}, n_{centre} is the number of element subdivisions along the single coil; these two parameters are the main parameters which rule the quality of longitudinal mesh and the capability to catch bending mechanisms.

After this step, the code starts building the single section by using two parameters (n_{node} and n_{points}) to describe the circle of the section; the section gets therefore subdivided by using three more parameters: $\_MID$ (which is the number of subdivisions of the core), $\_BL$ (which is the number of subdivision of the boundary layer) and c_f (which is the dimension of the core).

It's important to remark that this code produce duplicate nodes because of the algorithm used for the rotation; for this reason the text file produced is not the final Abaqus input file, but it is supposed to be modified through Abaqus_cae software

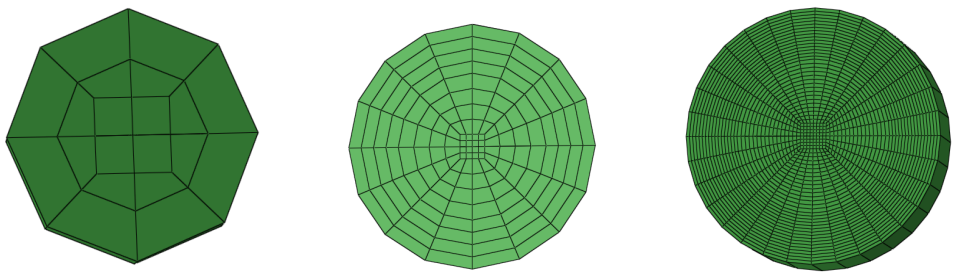

(a) Raw mesh (b) Medium mesh (c) Fine mesh

Figure 4.4: Examples of meshed section using compmech mesh generation algorithm

in order to "*merge*" duplicate nodes.
This brief introduction to the Matlab code has to be meant as an explanation of the dependencies between the code coefficient and the physical meaning; by modifying these parameters it has been possible to increase the quality of the mesh about the cross section, the longitudinal development or both of them. In tab.4.5 the analysis performed are reported, including the correspondent coefficients and number of elements of the mesh; in particular, test 17 was the finest mesh that was supposed to be the "exact" solution of the problem, so that it had been taken as comparison element for results.
The great difficult in generating the meshes of tab.4.5 was that the controllable variables don't change continuously because of the complexity of the section mesh; this meant that, in order to increase the number of mesh uniformly across the section (and not, for example, only in the core or radially), the number of elements raised quickly. In addition every test had to present a lower number of elements than test 17 in order to do considerations about convergence. For these reasons it is important to remark that the incrementation of the number of elements is not perfectly smooth and uniform in each direction.

Table 4.5: Spring test report: parameters for compmech mesh generation algorithm

Test n.	n_{node}	n_{points}	n_{centre}	_MID	_BL	c_f	Tot. Elements
1	10	9	80	1	1	0.3	1560
2	10	9	80	2	2	0.2	2808
3	10	9	80	4	4	0.1	5304
4	10	9	80	8	8	0.05	10296
5	10	9	160	1	1	0.3	3160
6	10	9	320	1	1	0.3	6360
7	10	9	320	8	8	0.05	41976
8	10	9	160	2	2	0.2	5688
9	10	9	240	3	3	1.2	12376
10	10	9	120	2	2	0.25	4248
11	10	9	120	1	1	0.3	2360
12	10	17	120	4	4	0.1	2360
14	37	33	320	8	8	0.05	183168
15	20	17	160	4	4	0.1	22752
16	37	33	80	8	8	0.05	44928
17	37	33	450	16	16	0.1	487424
18	37	33	640	1	1	0.3	223455

4.3.3 Beam element mesh

The two last meshes are based on the use of beam elements; particularly linear beams (2 nodes per element) and quadratic geometry beams have been used. As shown in fig.4.5 there's no mesh across the section of the spring: the section of the spring has been considered equal to the section of the beams and the discretization of geometry has been performed on the axis.

The arrangement of elements along the axis has been selected by a similar algo-

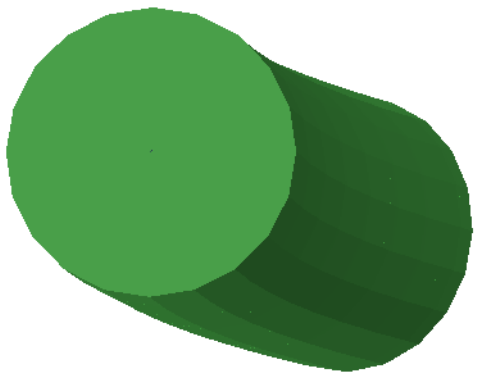

Figure 4.5: Examples of meshed section using beam elements

rithm than the one described in chapter4.4: the Matlab code has been modified in order to neglect section mesh. The modified code subdivides the axis in segments and automatically writes the Abaqus input file; differently to the original code, no duplicate nodes are produced and also the material parameters section, which is required in all Abaqus input files, has been included so that no modification by Abaqus_cae is needed.
In tab.4.6 and in tab.4.7 the analysis performed are reported as well as the correspondent axial mesh parameters used and the total number of elements.

4.4 Application of boundary conditions and external loads

The external load has been considered as an imposed displacement whose magnitude was $\bar{u} = 120\,mm$. Accordingly with the classic FEM framework, external imposed displacement gets implemented in the software as a boundary condition; one face of the spring is constrained, while the opposite one is supposed to move accordingly with the external load. In order not to introduce concentrated or non-axial perturbations in the problem, boundary conditions have been introduced by the use of two

Table 4.6: Spring test report: parameters for linear beams mesh

Test	n_{coil}	n_{centre}	Total elements
L1	30	640	639
L2	60	1280	1279
L3	120	2560	2559
L4	240	5120	5119
L5	480	10240	10239
L6	280	20480	20479
L7	30	640	319
L8	600	163840	81919
L9	90	1920	1919

Table 4.7: Spring test report: parameters for quadratic beams mesh

Test	n_{coil}	n_{centre}	Total elements
Q1	30	640	319
Q2	60	1280	639
Q3	120	2560	1279
Q4	240	5120	2559
Q5	480	10240	5119
Q6	280	20480	10239
Q7	300	40960	20479
Q8	600	163840	81919
Q9	15	320	159

reference points; the BCs have been applied on these points and then linked to the real sections of the spring trough internal constraint.
The aforementioned reference points have been obtained as the projection of the centre of the spring section on the spring axis (not the physical axis but the geometrical axis the spring twists around). Herein an internal constraint has been introduced to link the nodes on the spring section and the reference point; particularly MPC (multi-point-constrain) has been chosen. MPC internal constrain allows to impose a correspondence between a set of degree of freedom (correspondent to more than one node) and the degrees of freedom of a reference point: the nodes whose degrees of freedom get "merged" into the reference ones' are called *slave nodes*, while the reference point is called *master node*. In fig.4.6 the implementation of MPC in Abaqus_cae is shown.
MPC can be of different types, depending on the relation they create between slave and master nodes and their degrees of freedom; the main possible constraints are:

- BEAM. Provide a rigid beam between two nodes to constrain the displacement

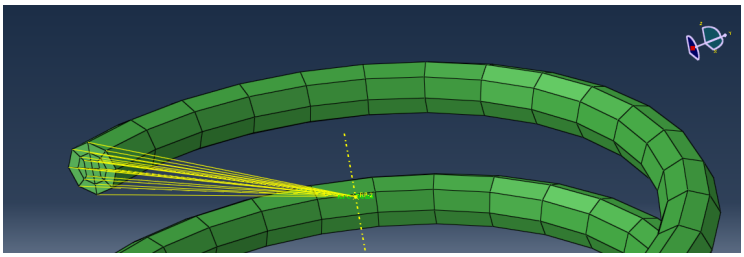

Figure 4.6: Graphic scheme of MPC

and rotation at the first node to the displacement and rotation at the second node, corresponding to the presence of a rigid beam between the two nodes.

- LINK. Provide a pinned rigid link between two nodes to keep the distance between the two nodes constant. The displacements of the first node are modified to enforce this constraint. The rotations at the nodes, if they exist, are not involved in this constraint.
- PIN. Provide a pinned joint between two nodes. This MPC makes the displacements equal but leaves the rotations, if they exist, independent of each other.
- TIE. Make all active degrees of freedom equal at two nodes.
- V LOCAL(S). Allow the velocity at the constrained node to be expressed in terms of velocity components at the third node defined in a local, body axis system. These local velocity components can be constrained, thus providing prescribed velocity boundary conditions in a rotating, body axis system.

For the current analysis, tie constraint has been chosen. Once created the internal constraints the following boundary conditions has been imposed:

- displacement = 0 in one master node
- displacement = 120 in the other master node, directed along the spring axis in order to produce a tension in the spring

4.5 Results

The complete analysis leads to a purely traction deformation of the spring as shown in figure 4.7. Several analyses based on different meshes were performed in order to point out some remarkable features and behaviours; the purpose of these analyses is to find an optimal and easy way to predict the behaviour of the spring, so that the

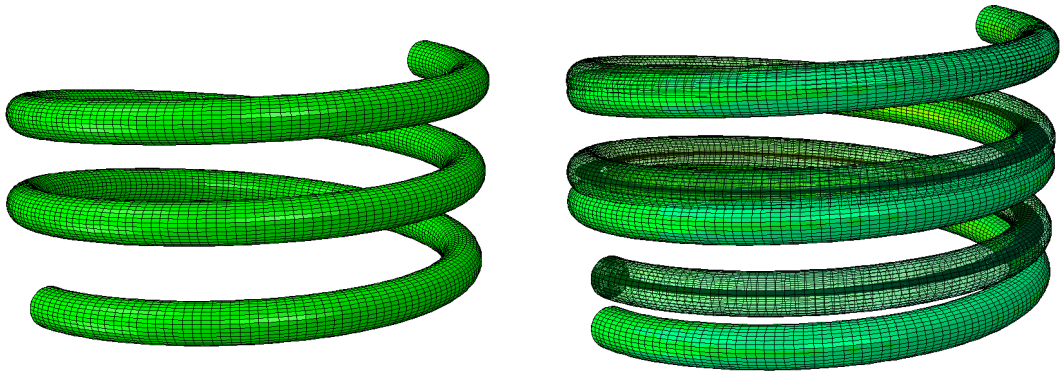

(a) Original spring geometry (b) Deformed spring

Figure 4.7: Deformation predicted by FEM analysis

numerical simulation could be considered a valid support for the design of springs by producing good results in a reasonable amount of time. The characteristic value considered, in order to judge the quality of results, is the total reaction at the spring base.

The first set of analysis performed aimed at finding an optimal mesh refinement by using the compmech algorithm; since the mesh depends on many parameters, several refinements were performed and each refined-mesh was obtained by modifying a specific set of parameters. In particular three kind of refinements have been investigated:

- Refinement on the section: no subdivisions along the spring axis are added: the refinement is increases the number of elements on the section by modifying the relative parameters. This refinement aims to better catch torsional resistance mechanisms of the spring.

- Refinement along the axis: the spring axis gets subdivided in a larger amount of parts, while the section mesh doesn't change. This refinement aims at better catching bending resistance mechanisms of the spring.

- "Total refinement": axis mesh gets enhanced as well as the section mesh. This refinement has the advantage to improve the capacity of the model to catch both torsional and bending phenomena; in addition it is an "homothetic" refinement, so that elements doesn't get distorted as in the previous kind of refinements. Anyway, for this refinement had been impossible to ensure a perfectly "homothetic" refinement because some parameters don't vary continuously.

The results of the above-mentioned refinements are reported in fig.4.8: the x-axis refers to the number of elements and, indirectly, to the number of degrees of freedom, while the y-axis refers to the logarithm of a norm of the error estimated by a comparison to the "overkilled" analysis (test number 17) considered exact. The most remarkable information evident from these curves is that the slope of the section refinement's curve is significantly higher than the axis refinement's one. This means that the refinement on of the section mesh leads to a more rapid convergence than the axis refinement, therefore the torsional resistance mechanisms appears to be prevalent than the bending one.

The second set of analysis aims at comparing the results produced by the different mesh generation algorithms described in section 4.3. Considered three meshes (one for each algorithm) with a similar rate between the number of elements along the axis and across the section, uniform refinements have been performed in order to build three convergence curves, similarly to fig.4.8. The results, reported in fig.4.9, show that the standard Abaqus mesh with "brick" elements produces the worst results; this could be caused by the fact that the other two meshes better approximate the circular section and the torsional phenomena consequently. Despite this issue the speeds of convergence of the two standard Abaqus meshes are equal. In addition, the compmech mesh generation algorithm shows an higher convergence speed, probably because its refinement is not perfectly "homotetic" between section and axis meshes so that the number of elements across the section increase more than the number of elements along the axis.

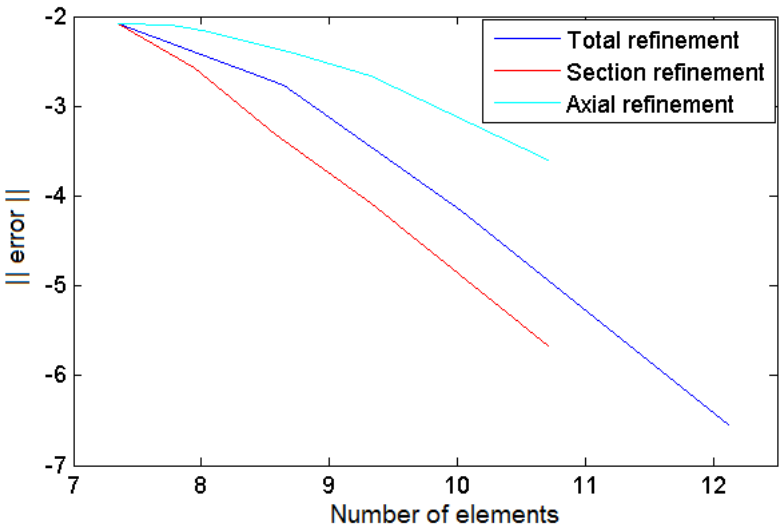

Figure 4.8: Convergence curves for the different kind of refinements in a semi-logarithmic space

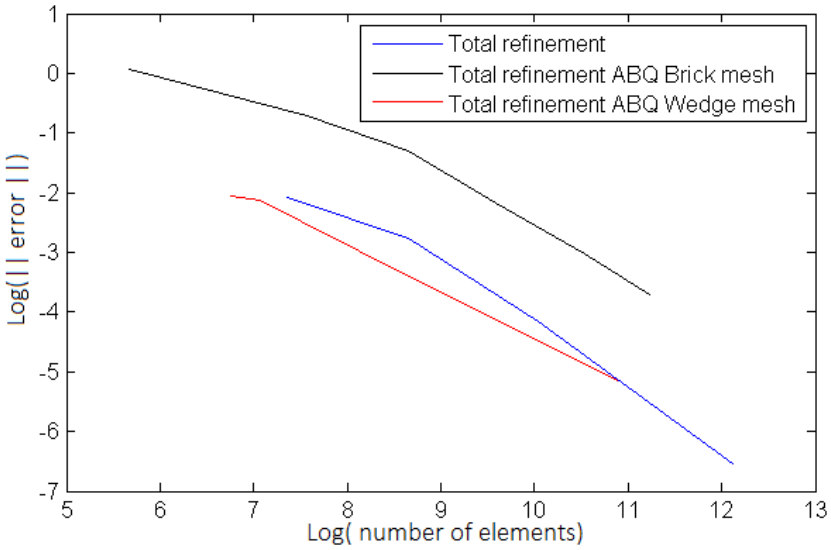

Figure 4.9: Convergence curves for the different elements and mesh topology

From this comparison the two beam-element meshes have been excluded because the problem formulation is different from the others; while spatial elements solve a spacial problem with only translational degrees of freedom, beam analyses are based on a different model of the problem and solve a different set of equations. From fig.4.10 is clear that the two meshes (using linear and quadratic beams) show a very fast convergence, since the analysis with 1000 elements (and 2000 nodes) has already reached an error of 0.5%; despite this it's important to stress that the overkilled result for these analyses is 30% different from the overkilled analyses results which used the other elements.

In conclusion, a summary of the results has been reported in fig.4.5. From an engineering point of view it's interesting to observe that, set an acceptable error e.g. 5%, the analyses which need the lower amount of elements to produce acceptable results are the analysis based on wedge elements and the mesh produced by compmech algorithm and refined on the section.

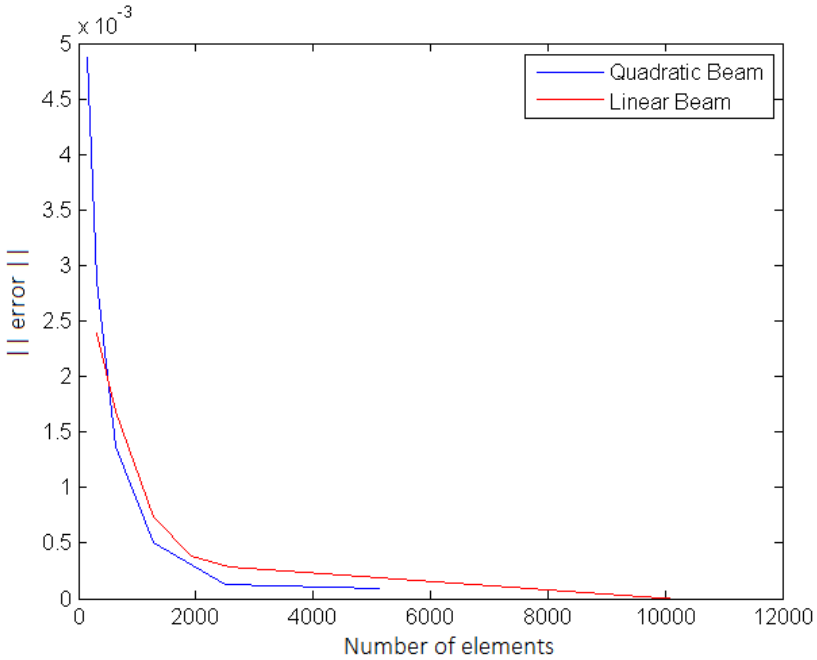

Figure 4.10: Convergence curves for the beam meshes

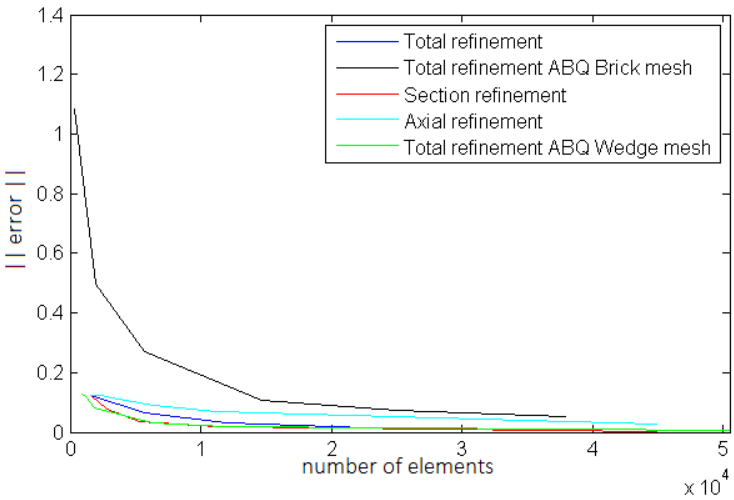

(a) Convergence curves for all analyses performed

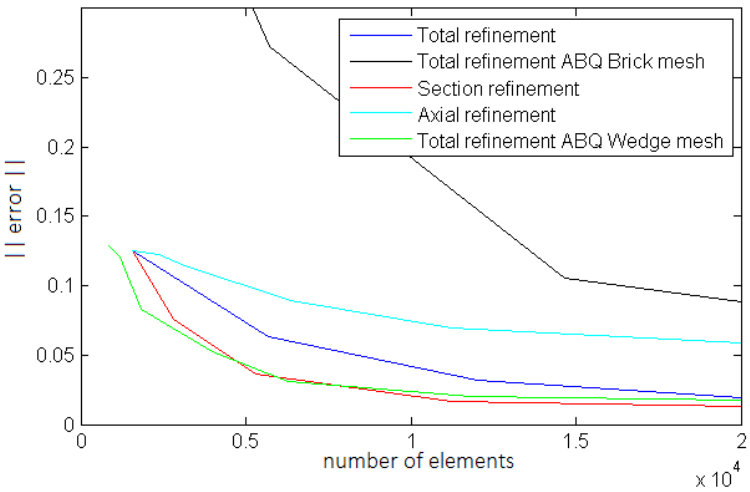

(b) Particular of convergence curves for all analyses performed

Chapter 5

Numerical implementation of the constitutive model: uniaxial cube test

This chapter describes the numerical implementation, within the Abaqus solver framework, of the two considered SMA constitutive models, i.e., Auricchio-Petrini-Souza and Auricchio-Taylor. Thereafter, a simple uniaxial tension test is performed which, by neglecting the influence of geometrical issues, lets to highlight the different features of the considered models.

5.1 Souza UMAT

Abaqus code is built with a modular scheme: the program flowchart simply links different parts of this code such as the information on the element, the material, the algorithm used in order to solve nonlinear systems and so on. This modularity allows the software to interface with user-defined subroutines which include essential elements for the analyses; these subroutines are supposed to work with a particular set of inputs and outputs, described in Abaqus manual, which link the user function and the rest of the program. In particular, UMAT is the specific class of subroutines that permits the implementation of constitutive models different from the default predefined models included in Abaqus.
The interface set of variables between UMAT subroutines and Abaqus is made of several type of variables: the variables to be defined, the variable that can be updated and the variables passed in as information. In the following paragraphs a summary of the main features of UMAT is proposed, taken from volume VI (*User Subroutines & Parametric Studies)* of Abaqus User Manual [13].

Variables to be defined

- DDSDDE: Jacobian matrix of the constitutive model, $\partial\Delta\sigma/\partial\Delta\varepsilon$, where $\Delta\sigma$

are the stress increments and $\Delta\varepsilon$ are the strain increments. DDSDDE(I,J) defines the change in the Ith stress component at the end of the time increment caused by an infinitesimal perturbation of the Jth component of the strain increment array. Unless the unsymmetric equation solution capability is invoked for the user-defined material, Abaqus will use only the symmetric part of DDSDDE.

- STRESS: this array is passed in as the stress tensor at the beginning of the increment and must be updated in the routine to be the stress tensor at the end of the increment. The measure of stress used in the "true" or Cauchy stress tensor.
- STATEV: this array contains the solution-dependent state variables. In finite-strain problems any vector-valued or tensor-valued state variables must be rotated to account for rigid motion of the material.
- SSE, SPD, SCD: specific elastic strain energy, plastic dissipation and creep dissipation respectively. They have no effect on the solution.

Variables that can be updated

- PNEWDT: is the ratio of suggested new time increment to the time increment being used. This variable allows to provide input to the automatic time incrementation algorithms in Abaqus (if automatic time incrementation is chosen).

Variables passed in for information

- STRAN: is an array containing the total strains at the beginning of each increment. These strains are avaiable for the output as the "elastic" strains. In finite-strain problems the strain components have been rotated to account for rigid body motion in the incrementation before UMAT is called and are approximations to logarithmic strain.
- DSTRAN: is the array of strain increments
- TIME(1): value of step time at the beginning of the current increment
- TIME(2): value of total time at the beginning of the current increment
- DTIME: is the time increment
- TEMP: is the temperature at the start of the increment
- DTEMP: is the incrementation of the temperature

- CMNAME: is the user-defined material name
- NTENS: is the size of the stress and strain component array
- PROPS: is the user-specified array of material constants associated with the user material
- NPROPS: is the number of user-defined material constants
- DROT: is the rotation increment matrix
- NOEL: is the element number
- NPT: is the integration point number

Souza discrete model, illustrated in equations 3.13 and 3.14, has been implemented in Abaqus through the creation of a specific UMAT. Abaqus' subroutines are supposed to be written in Fortran; in order to avoid bugs and producing a robust and efficient routine, the UMAT was not directly written in Fortran, but was produced by "Computational Mechanics and Advanced Materials Group" [15] by using an automatic AceGen algorithm. As illustrated in figure 5.1, AceGen libraries start from a symbolic code that include the problem formulation; this code (written with *Mathematica Wolfram*) gets translated in a numerical subroutine in Fortran 77. The Fortran subroutine is high efficient and includes all the numerical calculations needed for the material constitutive model; from this code it is possible to build the user UMAT subroutine by considering the name and construction of variables interface between the subroutine itself and Abaqus.

5.2 Description of the problem

In order to focus on the constitutive model a cube meshed by a single brick element subject to a tension/compression test is considered (fig.5.2). For the sake of simplicity the edges of the cube are 1 mm length, so that the imposed displacements will be equal to the uniaxial deformation.

In order to ensure a real uniaxial test, three faces of the cube have been constrained in the direction perpendicular to themselves. The uniaxial tension/compression has been implemented as imposed displacements in the four nodes delimiting the face perpendicular to y-axis not constrained yet.

The material constants have been set in the first instance equal to the parameters used in [2] and reported in table 5.1.

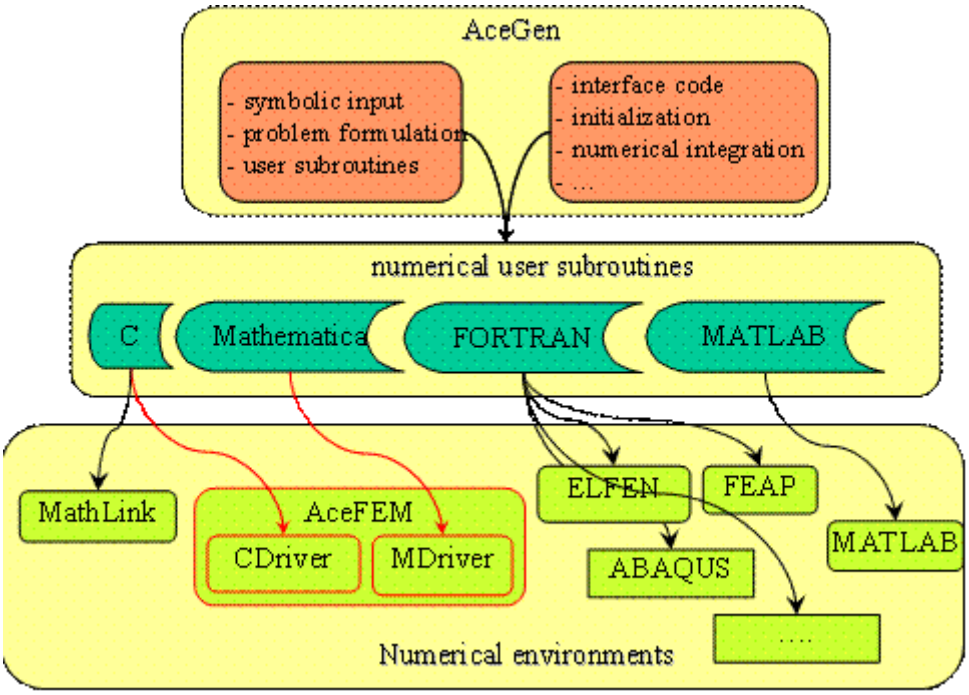

Figure 5.1: AceGen algorithm flowchart

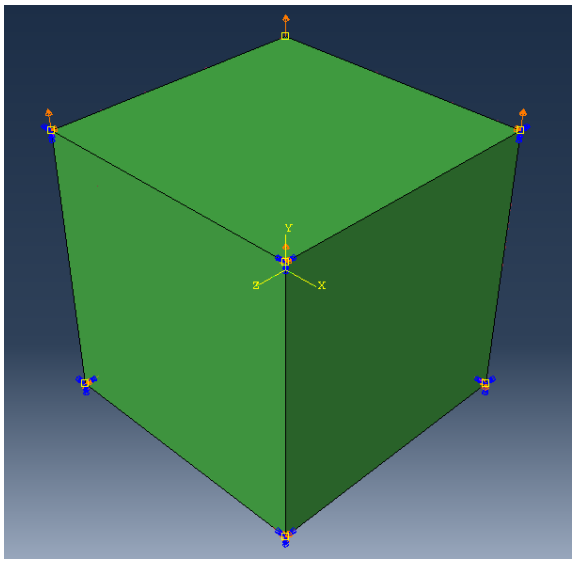

Figure 5.2: Geometry of the problem: cube meshed by a single brick element

5.3 Results

The purpose of the tests on the cube was to simulate and catch single phenomena related to the SMA behaviour. In this way it has been possible to produce some

Table 5.1: Abaqus Souza material parameters

E	Elastic Modulus	53000 MPa
ν	Poisson's ratio	0.33
h	Linear hardening parameter	1000 MPa
β	Stress-temperature relation parameter	6.1 MPa/K
T^*	Reference temperature	243 K
R	Elastic radious	100 MPa
ε_L	Maximum transformation strain norm	5.6%
δ	Regularized norm coefficient	0.02

benchmarks and modular analyses that can focus on the main features of material, so that, given experimental curves, it's possible to conduce best fitting procedure. The first set of results deal with the ability of the model to predict the pseudo-elastic effects. In figure 5.3 the results of the traction test at high temperatures in terms of stress and strain.

This test has been performed by imposing different temperatures, in order to focus on the dependence between the temperature itself and the material ability to recover the strain. In figure 5.4 is shown how transformation stress increases accordingly to the temperature and that at low temperatures the material is not able to fully recover the strain and residual deformation is evident.

The second main behaviour of SMA caught by these tests is the shape memory effect (see chapter 1.2); it is remarkable that this effect is not predicted by Auricchio-Taylor/Abaqus superelastic model, while can be simulated by Souza. In the first step the cube had been subjected by a load and unload phase that induced permanent strain (see the blue curve in figure 5.4); at this point temperature has been increased in order to induce phase transformation from deformed martensite to austenite and recover the original shape. The results of the complete test have been reported in figure 5.5; the same results have been reported in a more classical way in a $T - \varepsilon$ curve in figure 5.6.

Another diagram commonly used to understand and point out interesting aspects of SMA behaviour is the $T-\varepsilon$ (temperature-strain) curve during phase transformation, known in literature as *hysteresis test*. In figure 5.7 are reported the results of the cube subject to a constant load.

The last diagram taken from the cube analyses is another test under constant load. This plot is significant as simulates the behaviour in exercise of a large amount of actuators as well as the actuator designed in this thesis work and described in chapter 6. In figure 5.8(a) is reported a thermal hysteresis test after a load induced transformation; the analysis is made up from two steps: the first step of linear loading (which lasts 1 second) and a second step of temperature cycles under a constant magnitude of load. After the fist step, the material is in a martensite

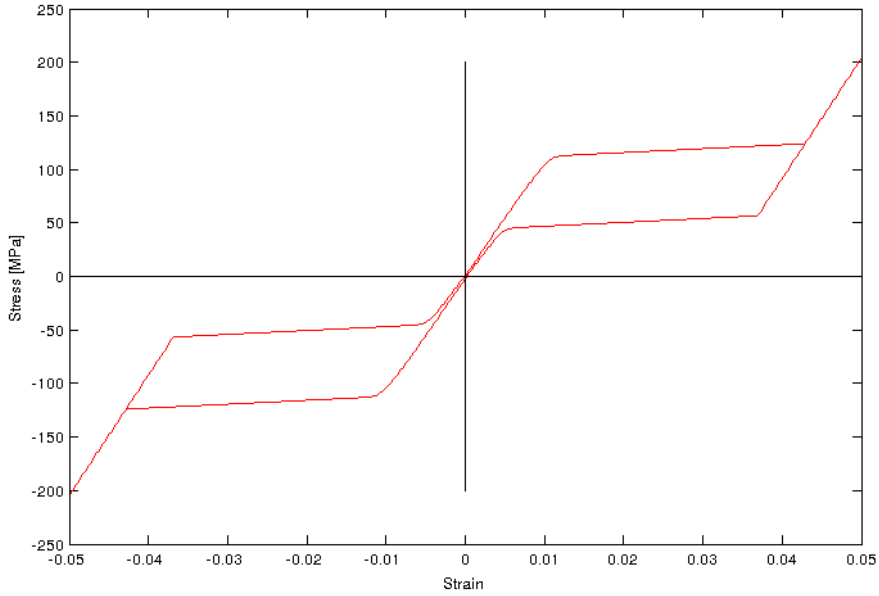

Figure 5.3: Pseudo-elastic behaviour seen in a $\sigma - \varepsilon$ curve

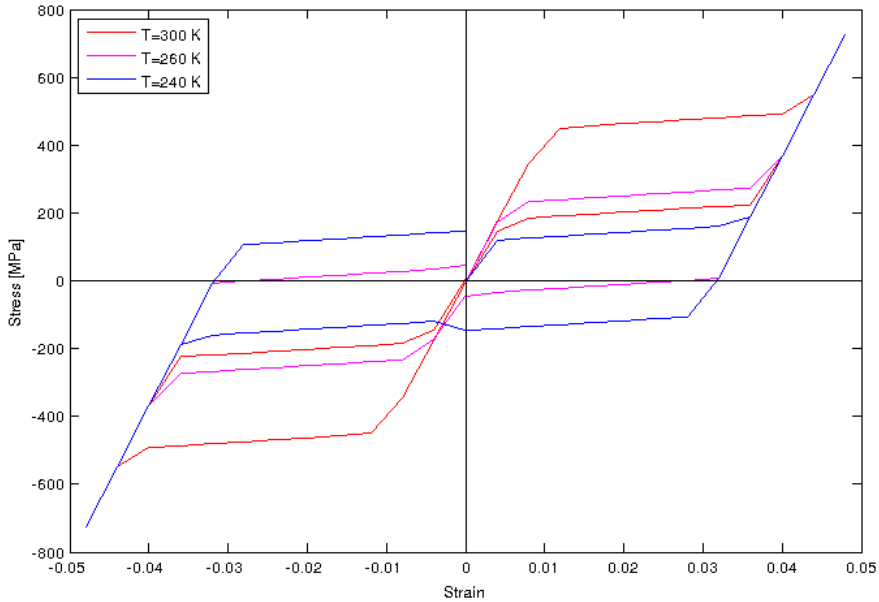

Figure 5.4: Pseudo-elastic behaviour seen in a $\sigma - \varepsilon$ curve

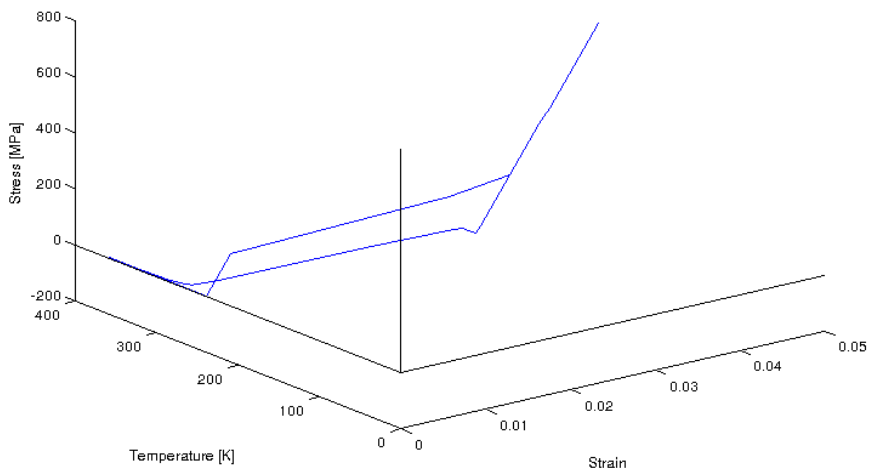

Figure 5.5: Shape memory effect: 3D curve

phase, so that in correspondence of the picks of temperature in step two, the reversal transformation occurs and the magnitude of strain decrease to the value of maximum austenite strain. Conversely, when temperature decreases, the austenite is no more stable and the material returns to a martensite phase and the value of strain induced by the load (that is the value of strain at the end of the first step).
In figure 5.8(b) a similar test is reported, but the thermal cycles have been imposed on an austenite phase because the magnitude of the load is less than the required load to induce phase transformation. In this test nothing happens in correspondence to the picks of temperature; on the other hand a thermal induced transformation occurs when the temperature decreases under a certain threshold. The transformation lead to an additional strain due to the fact that, given a constant value of load, austenite and detwinned martensite generate different value of strain (the martensite produces much higher strain than austenite).

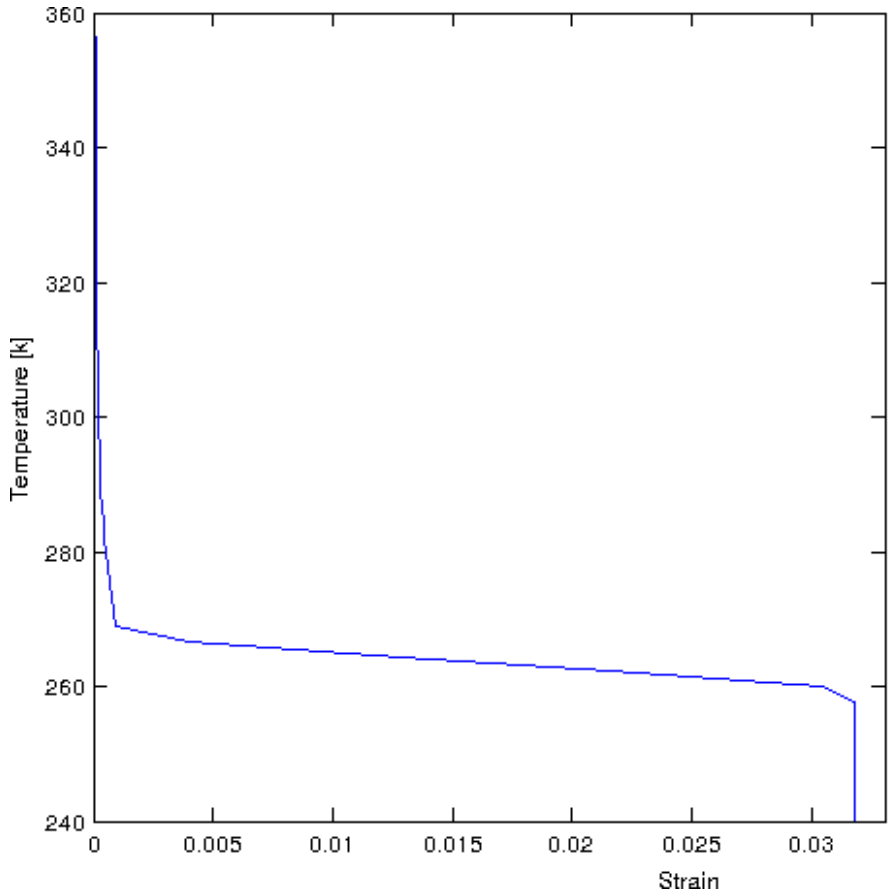

Figure 5.6: Shape memory effect: $T - \varepsilon$ curve

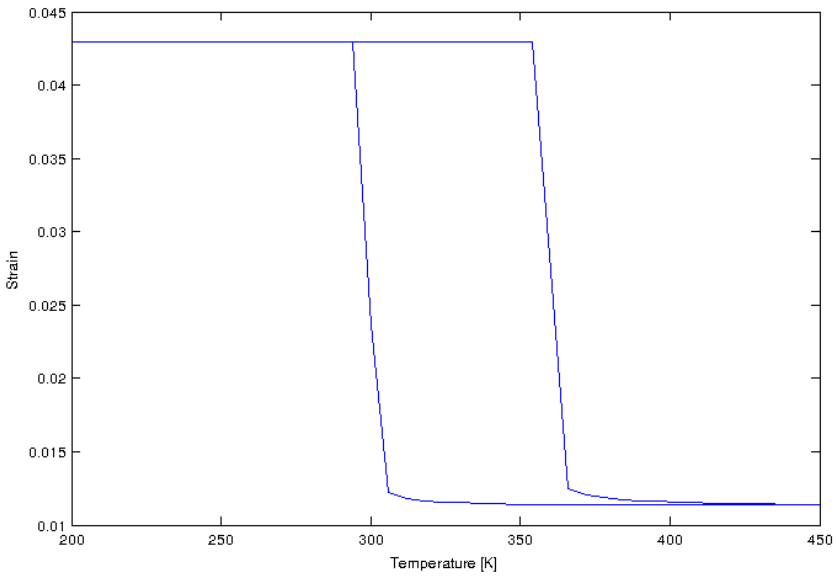

Figure 5.7: Strain-Temperature diagram during phase transformation

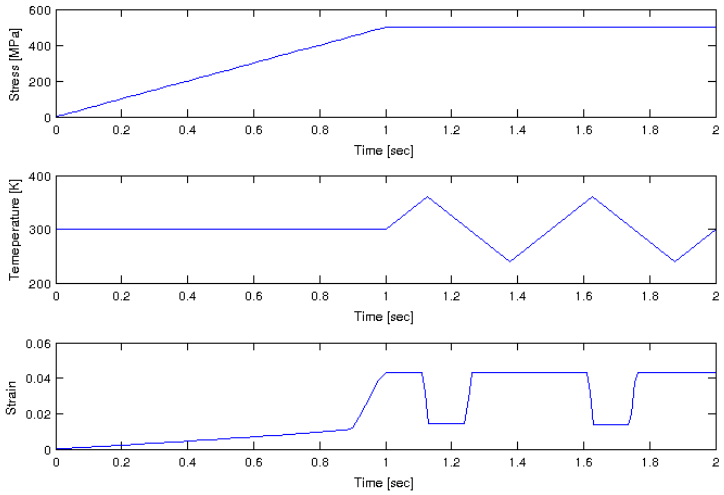

(a) Temperature cycles applied on a martensite phase element

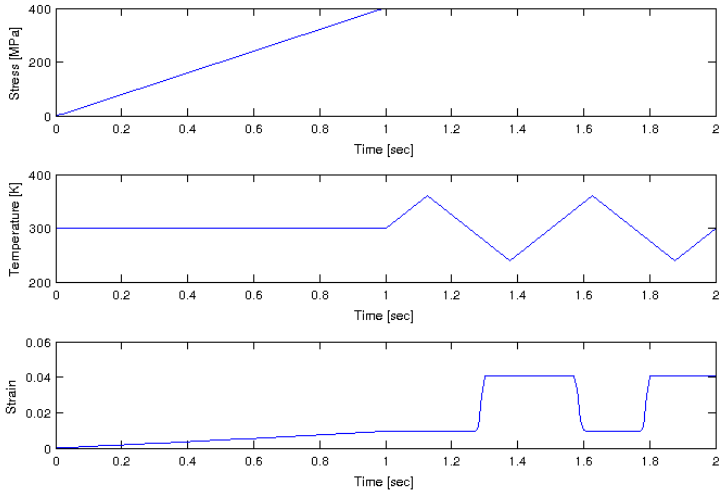

(b) Temperature cycles applied on a austenite phase element

Figure 5.8: Thermal hystereses under constant load

Chapter 6

Design and prototyping of a compliant gripper actuator based on a SMA wire

In this chapter will be reported all the steps necessary to the design and manufacture of a SMA based actuator. Nowadays actuators are usually designed without any numerical simulation; simple models are used to modelling the behaviour of the SMA parts, for example piecewise elastic model considering an high value of Young modulus for austenite (active actuator) and a lower modulus for the austenite phase. This is the most common approach because actuators usually move from a "on" to a "off' configuration, neglecting intermediate steps; in addition the most complex actuators are commonly assisted by an electronic system of motion control that is able to manage the mechanism actuation. The approach proposed in this chapter is an alternative approach to the design, whose purpose is to show the possibility to use more complex and accurate constitutive models to predict SMA mechanisms and to use finite element analyses in order to perform an high efficient optimization of the actuators.
Furthermore it is described and performed a technique of rapid prototipation based on the use of a 3D printer, which produces plastic prototypes of the actuators; this tool allows to compare simulations outputs to the real behaviour of the mechanical system analysed and to provide a valid support aimed at showing analysed projects.

6.1 Selection and analysis of the initial geometry

First of all the initial geometry, function and mechanism of the actuator have been chosen; the actuator chosen works as a compliant gripper whose mechanism is illustrated in figure 6.1.

The gripper should be actuated by a SMA wire supposed to apply the force and displacement needed to close the gripper. This mechanism is widely used in biomedical applications, i.e., for kidney stone gaspers . The initial geometry has been taken

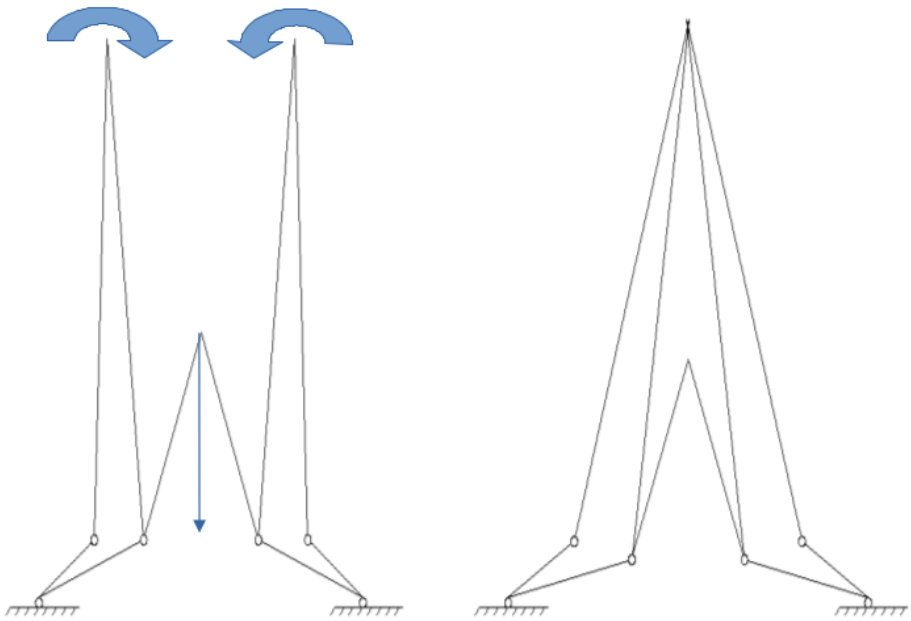

Figure 6.1: Working mechanism of the compliant gripper

from literature, i.e., a mechanism manufactured by Prof. K. J. Lu [14] in "Compliant Mechanisms Design and Optimization Laboratory" at the George Washington University. This original gripper, shown in figure 6.2, has strong similarities to the gripper to be designed, but it had not been thought for a SMA actuation; in addition its material is different from the material available for the prototipation, so that it has to be re-designed in order to work with a SMA actuation and a different material.

Material of the gripper The first step aims at analysing the current geometry of the gripper with the material used in Pavia, in order to understand the exploitation rate of the material. The material is a opaque material produced by Stratasys which is commonly used in 3D printers and it's named "VeroWhite Plus RGD835". The average technical details for the material are reported in table 6.1, while the simple traction test data from Melbourne Testing Services are reported in figure 6.3. As a complete load-unload test was not available, some assumptions have been done about the elastic and inelastic behaviour of the material.

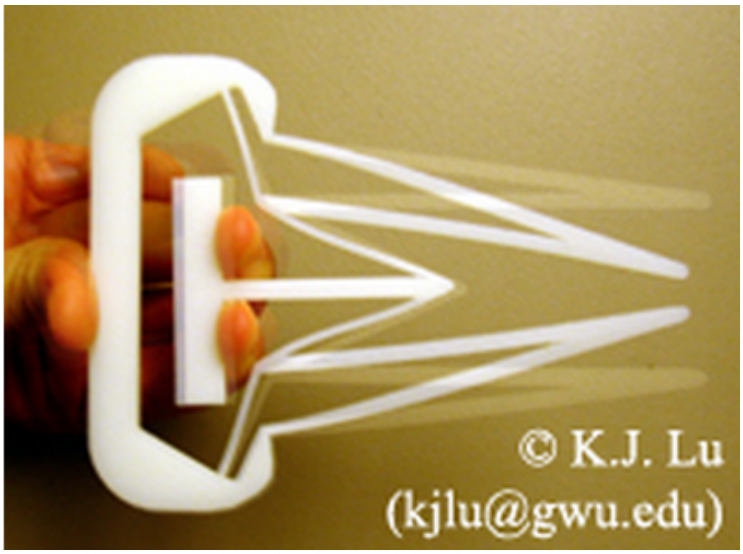

Figure 6.2: Initial gripper geometry

Table 6.1: Technical details of the gripper material

	ASTM	Units	Metric
Tensile strength	D-638-03	MPa	50-65
Elongation at break	D-638-05	%	10-25
Modulus of elasticity	D-638-04	MPa	2000-3000
Flexural strength	D-790-03	MPa	75-110
Flexural Modulus	D-790-04	MPa	2200-3200
HDT, °C @ 0.45MPa	D-648-06	°C	45-50
HDT, °C @ 1.82MPa	D-648-07	°C	45-50
Izod Notched Impact	D-256-06	J/m	20-30
Water Absorption	D-570-98 24hr	%	1.1-1.5
Shore Hardness	Scale D	Scale D	83-86
Polymerized density	D792	g/cm^3	1.17-1.18

Mesh generation The material has been considered linear elastic until a strain magnitude of 2.5%; thereafter the material have been supposed to produce plastic strain as seen in chapter 4.2. This assumption has to be considered acceptable since the material in the gripper will work at strain rate lower than 2.5% almost everywhere. The parameters of the elasto-plastic model are reported in table 6.2, while the elastic coefficients used are $E = 1951\,MPa$ and $\nu = 0.3$.

The analytic geometry of the gripper has been reproduced by using the software Solid Works that can export CATIA and IGES formats, which are importable as

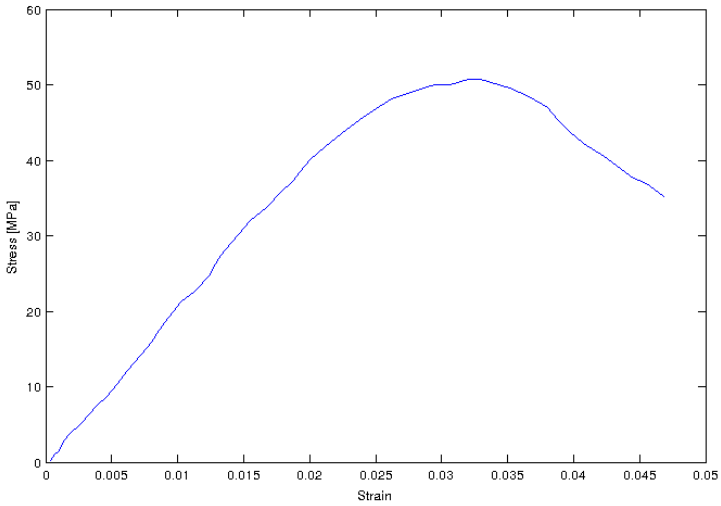

Figure 6.3: $\sigma - \varepsilon$ curve for a simple traction test on VeroWhite Plus Material

Table 6.2: Plastic parameters used to model the gripper's material

Nom. stress [Mpa]	Nom. Strain	True Stress [Mpa]	True Strain	Plastic Strain
47	0.025	48.175	0.02469	0
51	0.03	52.53	0.02956	0.00263
49	0.035	50.715	0.03440	0.00845
43	0.04	44.72	0.03922	0.01629
38	0.045	39.71	0.04401	0.02366

"Parts" in Abaqus-Cae. The geometry has been obtained as extrusion of the planar section of the gripper taken from figure 6.2. The solid obtained is $5\,mm$ deep; this value has to be considered a lower limit for thin elements prototyping as the material gets fragile if structured in thinner elements. The geometry, after having been imported in Abaqus-Cae, has not been meshed directly; in order to focus the attention on certain parts of the gripper and don't waste time and calculation in parts that don't influence the global behaviour, a subpartition mesh has been performed. The geometry has been divided in two symmetric parts and each part has been subdivided in seven regions which could be meshed separately as shown in figure 6.4.

Each part reported in figure 6.4 has been meshed separately according to the necessity in each part to have a specific quality of the mesh; the elements that have been used are "brick" elements and the mesh generation algorithm is the *medial axis* algorithm, already exposed in section 4.3.1. The seeding has been done by edges:

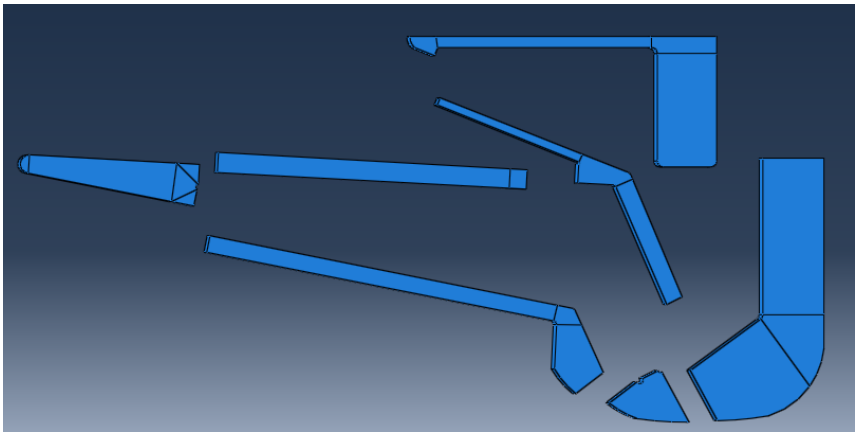

Figure 6.4: Subpatition of the global geometry

each edge of each region has been subdivided using a known number of seeds. The combination of seeding and medial axis algorithm for mesh generation allows to control the number and disposition of the elements (and correspondent nodes) on each face of the regions. This feature of the produced mesh is fundamental as every meshed part must be assembled to form the global geometry of the gripper and the boundaries of two contiguous parts must be meshed consistently; once meshed each part, they have been assembled and then the nodes have been *merged*: the function *merge* of Abaqus merges the nodes overlying or laying closest than a certain tolerance. The resultant meshed gripper is shown in figure 6.5(a); it is remarkable that the mesh is not uniform across the gripper, but is significantly finer in some points where strain will concentrate, as reported in figure 6.5(b).

Boundary conditions and Loads application The gripper has been constrained by imposing no displacements on its basis nodes. The external load magnitude was of $30\,N$ and applied uniformly on the central part of the geometry with the purpose to simulate the pressure of fingers on it as seen in figure 6.2. Since the gripper motion clearly produces large displacements, the analysis performed is a finite strain analysis and a cycle on the external load and boundary conditions is required; therefore, the load application has been subdivided in 20 steps with the purpose to facilitate the convergence of the non-linear solution and to be able, at the end of the analysis, to estimate precisely the value of load that corresponds to the closure of the gripper.

Results and study of the mechanism The results of the initial geometry analysis show that the central element moves $5\,mm$ from the initial configuration when the pincers get closed. The external load magnitude at this step is $22\,N$. As shown in figure 6.6, the stress distribution is concentrated in few and restricted regions (part

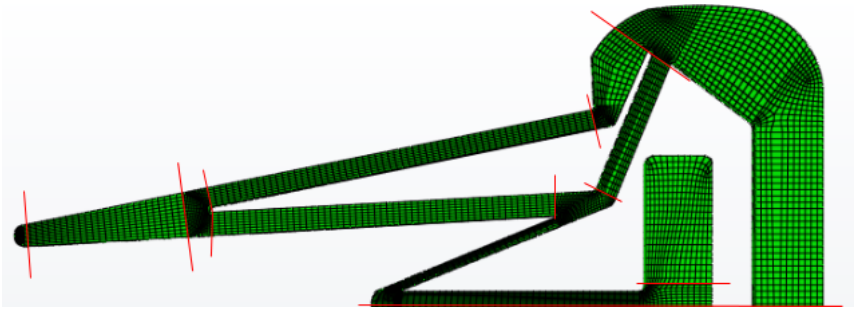

(a) Initial gripper meshed

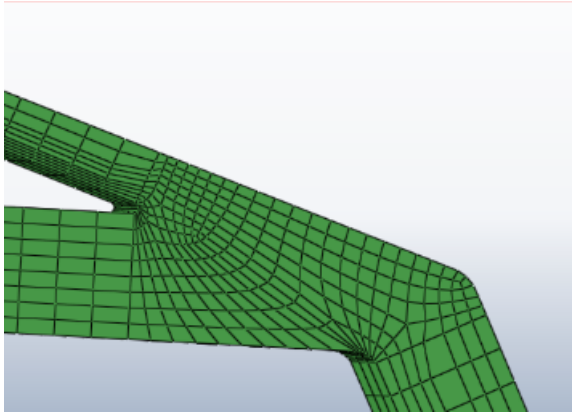

(b) Initial gripper meshed: particular

Figure 6.5: Gripper meshed

3 and 4, with reference to figure 6.6), but their magnitude is lower than the tensile strength of the material (see figure 6.3). Considering now the strain distribution; the strain picks are concentrated at the joints between the elements (in particular at the extreme sections of element 3 and 4; the magnitude of these picks is very high (close to 4%) and far from the admissible range of strain for current material. In addition it is evident from figure 6.6 that the element 3 has heavy second-order effect and it is close to suffer of instability.

From the results it was possible to catch the real resistant mechanisms of the gripper and the main differences from the theoretical model of figure 6.1. First of all the theoretical mechanism is based on rigid body motions: the gripper's ability to close is due to the presence of hinges that allow a large angular deformation without any stiffness contribution. On the other hand the designed gripper is supposed to be "monolithic", since no mobile pieces have to be required in order to ensure robustness to the object; this feature implies that the deformable joints are subjected to great strain rates, as they replace the hinges of figure 6.1. But there is another relevant

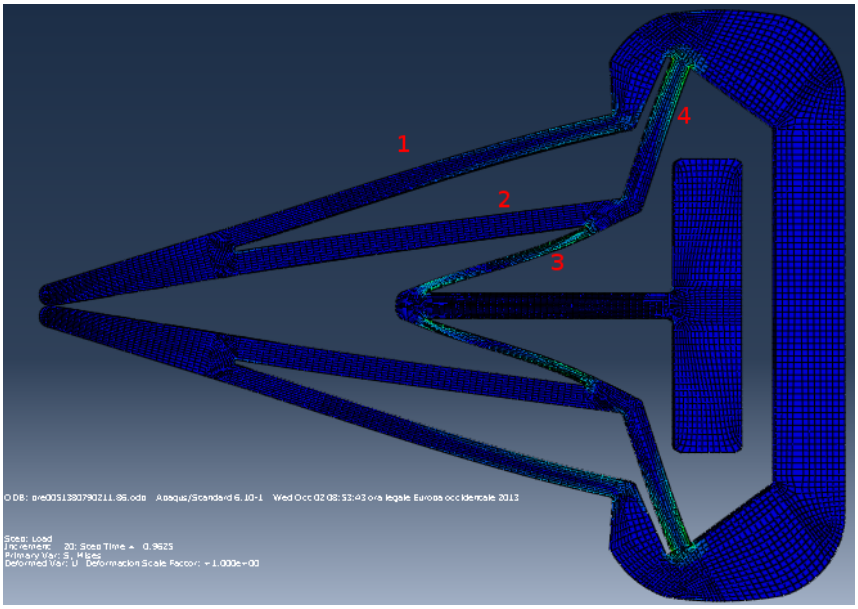

Figure 6.6: Initial geometry analysis: Von Mises stress

closing mechanism that was not predicted in the simplified mechanism: the bending of element 1. The external load application produce a clear load pattern across the gripper: the traction on the central element implies compression in element 3; that compression gets transferred through the joint to elements 2 (that mainly work in traction, too) and 4 (that reacts by a bending mechanism). Considering this load pattern, the element 1 gets subjected to bending by the force transferred by element 2 and the rotation produced by alement 4 at its extremal joints.

6.2 Optimization of the geometry

The geometry analysed in section 6.1, that had been optimized for another material and another type of actuation, shows few problems that make it unusable for the current project; the main features that must be changed to make it efficient for SMA actuation are:

- The maximum strain is too high for the current material; $2.5\% \div 3\%$ could be considered the maximum acceptable magnitude of the strain
- The element 3 in reference to figure 6.6 is affected by sensible P-Δ effects which cause instability
- The central element, which is used to close the gripper by hand, must be replaced by a place where locating the SMA actuating wire and a system that

ensure the actuation of the mechanism

In addition to prevent these evident deficiencies, the optimization has the following goals:

- Maximize the pincers excursion
- Minimize the closure requirements in terms of force and displacements of actuation (since the SMA wires used can ensure a force of few kgf and their maximum axial deformation is about 3% of the total lenght of the wire)

As first step different geometries have been proposed and analysed in order to understand the relevance of each element and dimension of the gripper. Four different geometries have been proposed in this step of the design. The four proposals, illustrated in figure 6.7, are based on different mechanisms and are designed to maximize some features of the gripper. For each geometry few characteristic dimensions have been chosen and several analyses have been performed by varying them in order to build a relation between these dimensions and the features above-mentioned.

6.2.1 Minimum stiffness geometry

The first geometry proposal has the goal of minimizing global stiffness of the closure mechanism; the basic idea is to concentrate the strain in a single joint while the pincers rotate rigidly; the central element has been removed in order to create a place where mount the SMA wire. The geometry has been characterized (see figure 6.8) by three dimensions:

- b: is the torque arm that transforms the linear force that will be applied from the SMA wire at the centre into the moment in the joint. It mainly influences the relation between the force/displacement of actuation and the rotational motion of the pincers: an high value of b means a low contribution of stiffness, but increases the actuation displacement needed to ensure the closure of the gripper; on the other hand a low value of b decreases the displacement needed, but increases the force that the wire should apply to the system
- L: is the length of the elements between the basis and the pincers of the gripper. It is highly relevant since the joint is not able to "absorb" all the strain necessary to allow the pincers to close: while the pincers and the diagonal element rotate rigidly, these elements react in bending and can be schematically represented as a beam with a clumped extreme and a imposed rotation at its second extreme. In addition, L is proportional to the distance from the basis of the gripper to the central element where the wire will be attached and, according to this, to the wire length itself

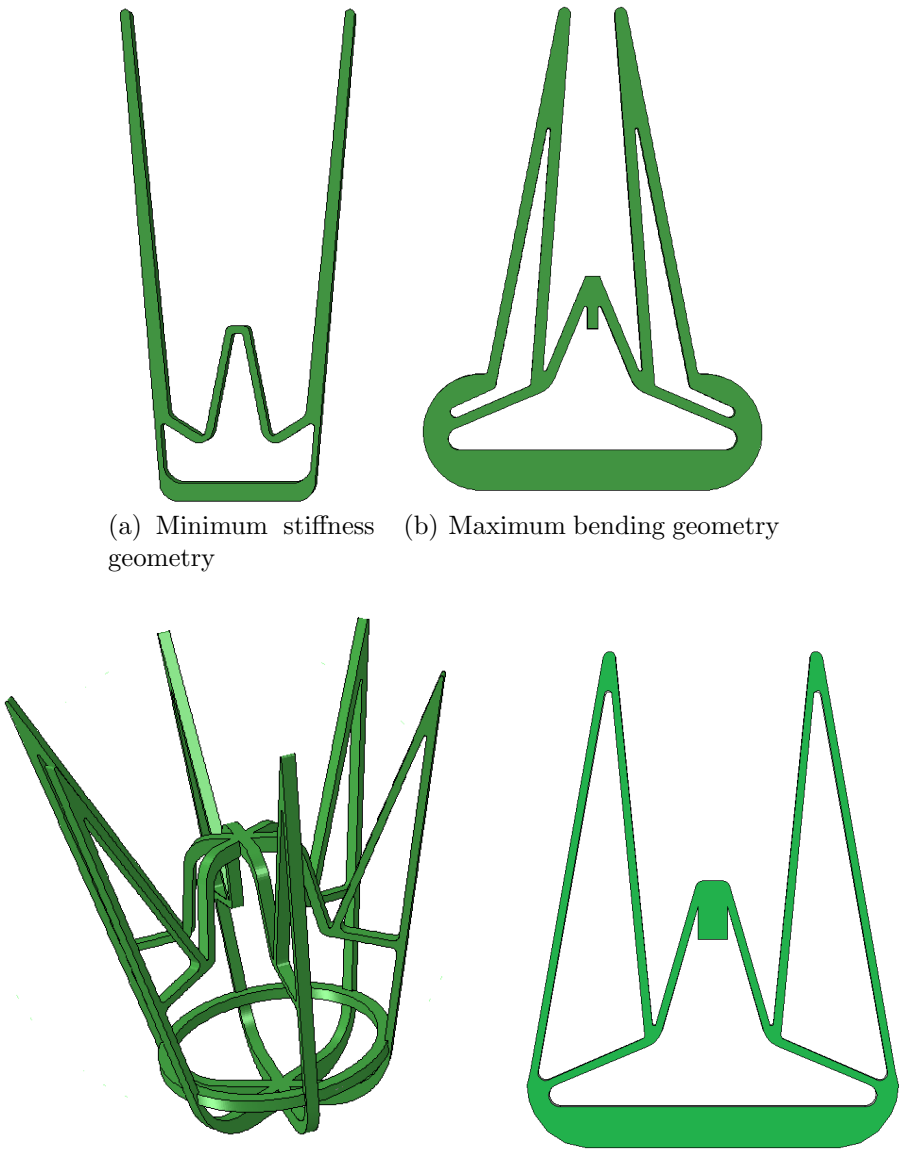

(a) Minimum stiffness geometry

(b) Maximum bending geometry

(c) Maximum excursion geometry

(d) Maximum pincers rotation geometry

Figure 6.7: Geometry proposals

- t: is the thickness of the element length of L. Considering the above-mentioned representation of this element as a clumped beam, t represents its section's hight and, consequently, the main contribution for the stiffness; a higher value of t means a higher global stiffness and strain concentration at the joint, while

a low value of t implies a concentration of strain on the element itself. In addition must be considered a low threshold given by the precision of the 3D printer that doesn't manage to manufacture too thin elements.

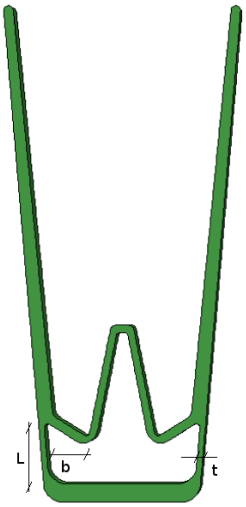

Figure 6.8: First geometry proposal: characteristic dimensions

Starting from three reasonable values of the characteristic dimensions ($t = 1.5\,mm$, $b = 5\,mm$ and $L = 55\,mm$) different meshes has been created by modifying one dimension at time and evaluating the most relevant outputs; this step has produce the results reported in table 6.3. Starting from the results of table 6.3 an empiric and simplified relation between the input and output data has been created through a minimum square algorithm and a optimum geometry has been selected. The optimum geometry, shown in figure 6.9, has been analysed and the results are reported in table 6.4. It is remarkable that the constant thickness b has been replaced by a tapered element, where the dimension b has to be considered an average length. The analysis results can be considered satisfactory, but some problems subsist: first of all the strain rate is slightly above the superior elasticity threshold of the material, which could lead to the formation of inelastic strain during the actuation and the consequent unrepeatability of the mechanism; in addition the space for the wire is $8\,cm$ length: considering a necessary displacement of $3,1\,mm$, the required axial recover capability of the wire is about 3.8% that is higher than the capability of the available wires.

6.2.2 Maximum bending geometry

Differently from geometry 6.8 where pincers rotated rigidly while the strain was concentrated mainly in the joints, the second geometry proposal mechanism of closure

Table 6.3: Results of varied minimum stiffness geometries

Inputs	Outputs at the gripper closure		
	Max Strain [%]	Actuation displacement [mm]	Actuation Force [N]
t=1.5 mm b= 5 mm L=55 mm	5.8	3.5	14.1
t=3 mm b= 5 mm L=55 mm	2.9	3.3	17.4
t=3 mm b= 8.5 mm L=55 mm	2.7	6	16.4
t=3 mm b= 3.5 mm L=55 mm	3.7	2.7	34
t=3 mm b= 5 mm L=10 mm	3.9	4.9	29.7
t=3 mm b= 5 mm L=30 mm	3.2	5	23.2

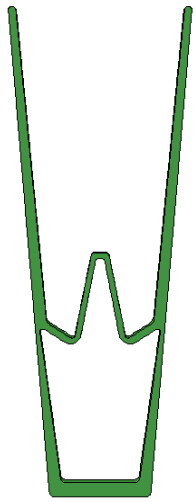

Figure 6.9: Minimum stiffness final geometry

Table 6.4: Results of varied minimum stiffness geometries

Inputs	Outputs at the gripper closure		
	Max Strain [%]	Actuation displacement [mm]	Actuation Force [N]
t=3 mm	3.3	3.1	21
b= 4.5 mm			
L=51 mm			

is based on the bending of the elements which compose the gripper. Because of the complexity of the mechanism, different quoted dimensions had to be considered to characterize the mechanism; in reference to figure 6.10, the load pattern from the wire and the pincers identifies the following elements:

- At: is the central element where the first end of the wire should be attacked
- B: is the basis of the gripper where the first end of the wire should be attacked
- S: is a diagonal element which transfers the linear actuation force/displacement to the closure mechanism; it mainly works by shear and bending
- b: is the brace, between the first pincer and the centre of rotation; it is remarkable the substantial difference from the b of geometry 6.8: in the first case, b is a short element that doesn't bend, but rotates rigidly, while the strain is focused at its end joint. On the other hand, in the case of geometry 6.10 it is a bending element clumped at its end
- Pi: is the internal pincer; it works in traction
- Pe: is the external pincer; it works mainly in bending between a quasi-clumped end (the joint between itself and element G) and the joint with Pi. In addition to bending, this element is also compressed, that could increases the Pe-element displacement by second order effects (P-Δ effects) during the large displacement analysis
- G: is an element which slightly deforms in bending, but is substantially mechanically inactive; its presence is mainly due to geometrical purpose

The described mechanism has been identified thanks to preliminary analyses and modelling the gripper as a frame structure and imposing the equilibrium at the joints. After having identified the correspondence between the elements and their resistance mechanisms, the characteristic dimensions for the geometry have been chosen:

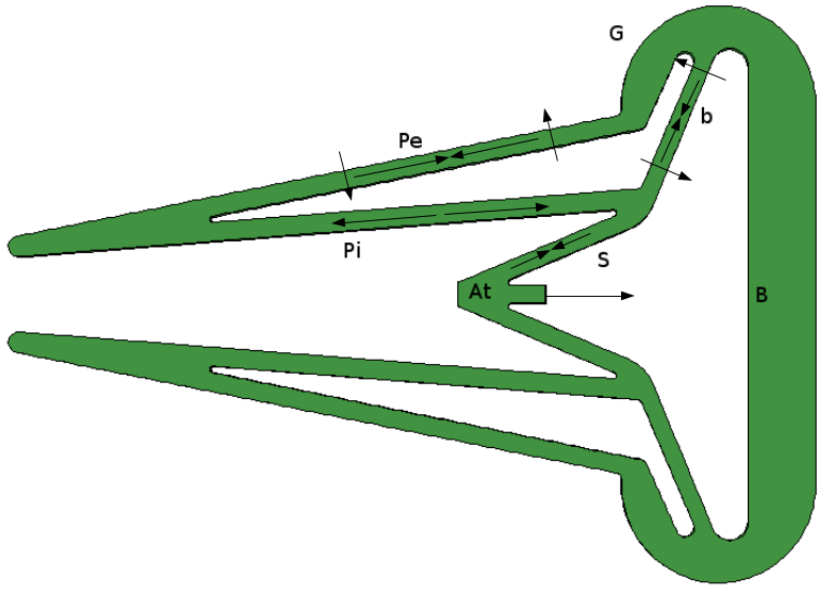

Figure 6.10: Maximum bending geometry

- The distance between the external limits of B and At: is the length of the SMA wire; this active length defines the portion of the wire in which electric current will pass increasing the wire's temperature by Joule effect

- The inclination of S, which influences the design in two ways; at first, when S tends to be parallel to Pi the distance between At and B increases as well as the length of the wire (remember that the maximum actuation displacement is proportional to the active length of the wire). In addition the more S gets parallel to Pi, the more S will react in compression instead of bending: this is a purpose of the optimization as S is supposed to transfer a linear force to the node $Pi - S - b$ in order to tensioning Pi, while a bending momentum would not influence axially the internal pincer. On the other hand when S and Pi are close to be parallel, the dimensions of the node $Pi - S - b$ increase, which greatly increases the global stiffness of the structure

- The maximum excursion of the pincers which depends on the inclination of Pi and Pe

- The relative inclination between Pi and Pe; it is the most important parameter for this geometry since it controls the rate of tensile stress in Pi which transforms into bending or compression in Pe: when the relative angle tends to zero, bending phenomena can be neglected, while compression will be highly relevant. On the other side, when the angle increases, first order bending gets

relevant, but second-order bending decreases. In addition a very important aspect has to be considered: when the two elements are close to be parallel, assuming their joint smoothness constant, the effective length of the elements decreases as well as their bending flexibility. The aspect of the smoothness of nodes has to be considered a crucial issues as sharp joints correspond to high and localized strain rates leading to fractures, while smooth ones greatly increment the global stiffness of the mechanism

- The connecting element G is used to separate the strain arriving from Pe bending from the strain arriving from b, differently from the previous geometry where all strain were located in a single joint. The dimensions of G are not influencing significantly the global mechanism; however it remains an active element as a too much big (and stiff) element G would add excessive stiffness to the mechanism; on the other hand a too flexible G would not guarantee a centre of bending to Pe which would translate pseudo-rigidly while G element would bend instead of it.

The analysis of trial geometry (shown in figure 6.10) showed that the gripper got close by the application of an actuating force of $12\,N$ (which is compatible with the capacity of SMA wires) and a displacement of $4\,mm$, which was too high for the possible wire to be installed; from this starting point an optimization has been performed pursuing the maximum possible excursion of the pincers. The optimization has been performed in two phases: at first the necessary free space for a longer wire has been created; after that the geometry has been modified in order to ensure a larger motion without increasing the global stiffness (and the actuation force).
Considering an approximate rate of recoverable axial strain of 3% of the total length and the actuation displacement of $4\,mm$, the necessary wire length has been obtained as $L = 4/0.03 = 130\,mm$; with the purpose of mounting a $13\,cm$ length wire in the gripper, an auxiliary part has been added under the basis, as seen in figure 6.11. The structure is much more stiff than the other parts of the gripper, so that is essentially inactive in terms of deformation.

From this geometry configuration, the maximum excursion has been obtained by making Pe horizontal and the two Pis divergent; this configuration needs a larger actuation displacement (and, consequently, force) since the closure mechanism substantially coincides to the previous one while the required rotation of the pincers has increased. First of all relative inclination between S and b has been reduced; by this change, Pi is no more stressed in its axis direction, but its right end gets bended clock-wise; that rotation gets transferred to Pe supporting the closure mechanism. The second step in optimization algorithm was to sharpen the joints and to reduce elements thickness until the threshold above which inelastic strains would form within the nodes. In this step, each part of the gripper has been modelled as a beam with constant cross section and known displacement and rotations at its ends:

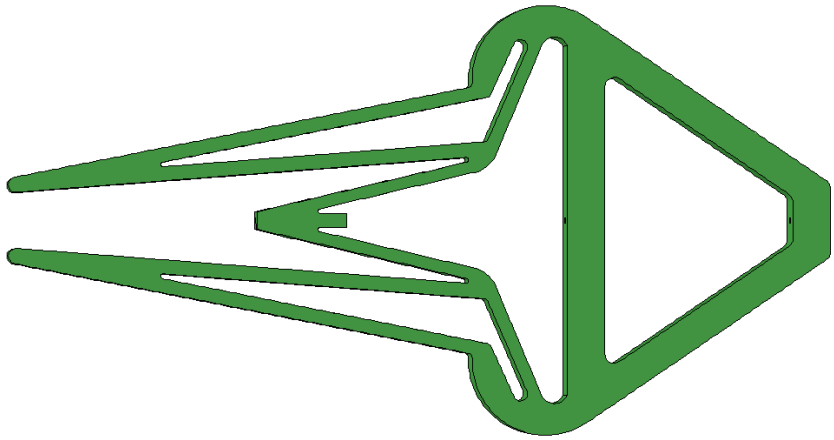

Figure 6.11: Geometry with the auxiliary structure to allow the mounting of longer wires

given this information, maximum internal forces have been computed and so the maximum strain in sections, accordingly to the classical beam theory. In reverse, given the maximum value of elastic strain, the value of the thickness of each element has been derived. The above-described algorithm is obviously approximate as it doesn't take into account the large displacement theory, the fact that the nodes' displacements and rotations (inferred from previous analyses and the difference between the original and the expected deformed configurations) will not be the real ones; at last this algorithm neglect the inside-nodes phenomena, which are highly relevant in the analysis. Despite these lacks, the algorithm has the advantage to be very quick and to lead to reasonable values of thickness; after having computed the first trial set of elements' thickness, FEM analyses have been iteratively performed and the elements dimensions adjusted until the joints reached the maximum admissible strain rate.
This algorithm brought to the geometry in figure 6.12(a). This gripper geometry needs a $4\,mm$ actuation displacement and, when closed, shows a maximum strain value of 2.9%. It is important to observe that the geometrical optimization led to satisfying result: without changing the global closure mechanism, the pincers excursion has duplicated without increasing the the actuation displacement. This aspect is due to the fact that thinner elements highly reduce the dimensions of the nodes, especially in quasi-parallel elements and, accordingly, the global stiffness; for example, in addition to the already mentioned joint between S, b and Pi, is significant the case of the Pe-Pi joint: just by decreasing their thickness, the node's dimension has been reduced and the length of Pi and Pe has increased by 18% allowing a larger bending inflexion.

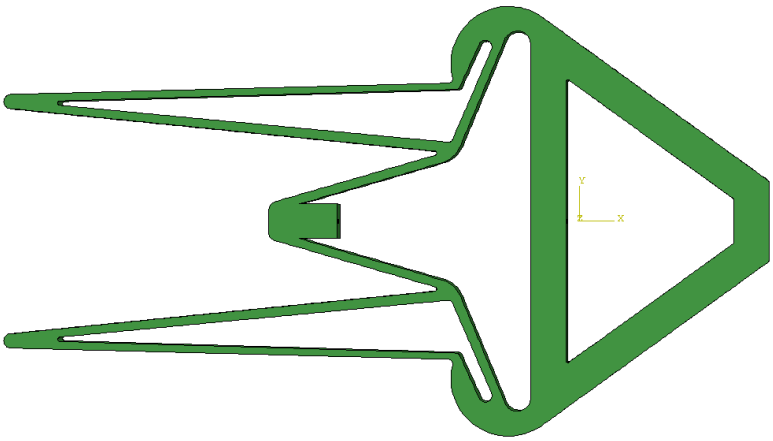

(a) Final optimized geometry

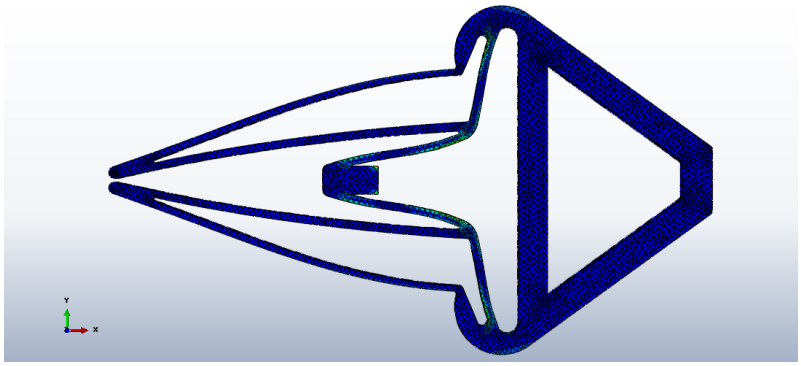

(b) Closure simulation output

Figure 6.12: Optimized gripper's geometry before the actuation (a) and after the actuation (b)

6.2.3 Other proposed geometries

Geometries shown in figures 6.7(c) and 6.7(d) are the geometries whose optimizations didn't lead to a working closure mechanism. The geometry 6.7(d) had been thought as an intermediate mechanism between geometries 6.14(a) and 6.7(b). Geometry 6.7(d) works by a bending mechanism of element Pe, as well as geometry 6.7(b). The FEM analysis produces the results reported in table 6.5. It is clear that both results are far from an acceptable magnitude: the absence of element G of geometry 6.10 forces the strain to concentrate in a single node, while the absence of element L used in geometry 6.8 makes the node itself too stiff. Finally the introduction of a long element b, which leads to a relative large angle between the

two elements composing each pincer, decreases second order phenomena. For these reasons the geometry has been considered unable to fit the goals of the optimization because based on a inefficient mechanism.

Table 6.5: Closure requirements of geometry 6.7(d)

Output	Magnitude	Units
Actuation displacement	8	mm
Actuation force	44	N
Maximum strain	5.6	%

The geometry 6.7(c) has been thought to maximize the excursion of the pincers by a 3D closure mechanism; six pincers have been designed in couples and the global geometry has been obtained as a discrete revolution around the centreline of the gripper. The in-plane shape of the geometry 6.7(c) is similar to geometry 6.7(d), with the addition of a substructure to accomodate the wire and decrease the stiffness of the node between the element corresponding to b and Pe of the other geometries. The FEM analysis results are reported in table 6.6. The geometrical outputs are similar to the outputs of the previous geometry (table 6.5) as the kinematics of the mechanism has not been changed; on the other hand the force requirements are nearly three times of the previous one. This is a awaited result as the 3D mechanism is just the assembly of three compliant grippers with their own stiffness, and the addition of the substructure (which decreases the stiffness of the main node) is not enough to ensure an acceptable flexibility of the structure. For these reasons this geometry proposal has been discarded because based on a mechanism unable to fit the requests of closure of the actuator.

Table 6.6: Closure requirements of geometry 6.7(c)

Output	Magnitude	Units
Actuation displacement	8	mm
Actuation force	96	N
Maximum strain	5.9	%

6.3 Modelling of the wire

Once modelled the gripper, the SMA actuating wire has to be included into the analysis. First of all the constitutive model parameters for the wire are needed. The wire used to build the actuator is a Nitol wire produced by Saes Getters s.p.a.

and provided to the "Computational Mechanics & Advanced Materials group" of *University of Pavia* [15] as research material. We consider two different diameters value, i.e., $0.3\,mm$ and $0.15\,mm$. The first wire produces in exercise conditions a force equal to $15\,N$, compatible to the required actuating force for geometry 6.7(b) ($12\,N$). In order to derive the constitutive models parameters for the FEM analyses, a set of experimental tests has been carried out on the wire, whose results would be the input data for the best-fitting algorithm by which the parameters have been computed.

6.3.1 Uniaxial tensile test in thermal chamber on the SMA wire

The equipment used in the test on wire is the MTS Insight Testing Systems 10 kN (MTS System Corporation), shown in figure 6.13(c). The test equipment is composed by the following parts:

- *Grips*, visible in figures 6.13(a) (wedge grips) and 6.13(b) (pneumatic grips). The first ones get closed manually, while the second ones get closed by a system of compressed air wires. The pneumatic grippers are built suitably for testing wires: they have larger gripping surfaces that avoid the wires to crimp and their geometry facilitates the mounting of the wires. On the other hand the compress air wires don't resist at high temperature: the higher threshold for their usage is about $145°C$: for this reason, wedge gripper were preferred for the current tests

- *Cross-head*, which is the cross element that moves the superior grip

- *Load cell*, visible in the hight part of figure 6.13(c). Two cells, respectively, of *10 kN* and *250 N* are supplied with the device; considering the wires tested, the *10 kN* load cell has been used for the current tests

- *Thermal chamber*, visible in figure 6.13(c); it's a thermally isolated chamber which can be mounted across the machine. A system of electric resistances and liquid nitrogen controls the temperature inside the chamber, where the specimen and the grippers are located during the test

The test flowchart has been defined by *TestWorks4*, which is the software interface between the machine and the computer; by this software is possible to define the test flowchart, control the test while it has been carried out and post-process output data. Since no thermal controlled test have never been carried out before, a new user-defined flowchart has been defined. The test has been subdivided in four steps, as illustrated in figure 6.14:

(a) Wedge grippers (b) Pneumatic grippers for wires testing (c) "*MTS Insight Testing System*" testing machine

Figure 6.13: Testing equipment used in the tests

- Step I, from $t0$ to $t1$: the unloaded wire at room temperature T^0 gets heated till a certain value of temperature *T1*, which is a test parameter. This incrementation of temperature induces a phase transformation in the wire, from martensite phase to austenite phase.

- Step II, from $t1$ to $t2$: the wire gets pre-loaded until it reaches a certain load rate, parameter of each test (set by default to $8\,N$). The pre-load is done by imposing a linear incrementation of displacement with velocity v^p parameter of the test.

- Step III, from $t2$ to $t3$: the wire gets loaded until it reaches a certain load rate, parameter of each test (set by default to $50\,N$). The loading phase is done by imposing a linear incrementation of displacement with velocity v^l parameter of the test, with $v^l < v^s$ in order to better catch the loading-related phenomena; v^l is usually taken lower than $8\,mm/min$ in order to avoid high gradient of load in case of break.

- Step IV, from $t3$ to $t4$: the wire gets unloaded until the cross-head reaches the position it had at the end of Step II.

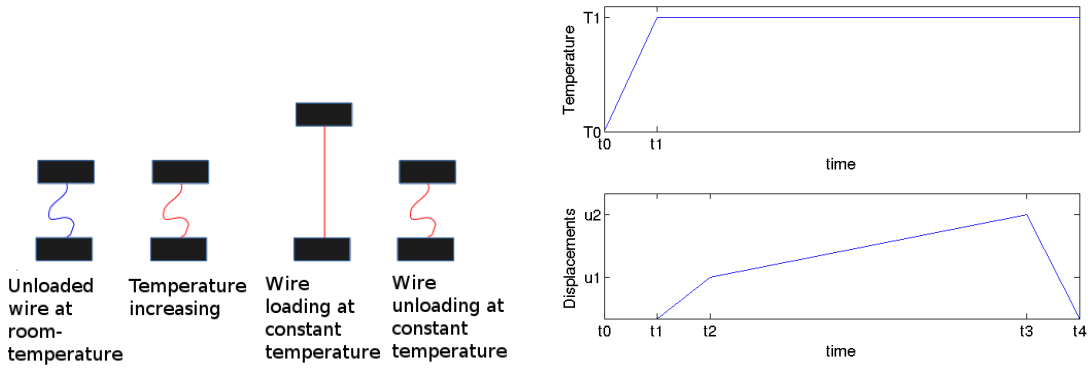

(a) Illustration of the test flowchart

(b) Variation of control variables during the tensile test

Figure 6.14: Tensile-thermal controlled test flowchart

The test had been tested 17 times without exporting the outputs in order to train it and making its mechanical behaviour stable. After the training phase, several tests have been carried out at different temperatures; in particular, five tests have been done at 95 $°C$ because that is almost the temperature of the wire during the actuation. The data output provided by the software were in terms of load (N) and displacements (mm); the post-processing of experimental data consisted in:

- Compute the stress as $\sigma = \dfrac{F}{A}$, where F is the output load value and A is the area of the wire
- Compute the strain as $\varepsilon = \dfrac{u}{L_0}$, where u is the output displacement value and L_0 is the original wire's length
- Translate the $\sigma - \varepsilon$ curve in order not to consider the cross-head displacements when the wire is bland as producing strain

After the post processing operations, pseudo-elastic response curves have been exported in Matlab as shown in figure 6.15 and 6.16.
In addition to the test above described, a second flowchart (fig. 6.17 has been set, in order to better catch thermal related phenomena.

Similarly to the first workflow, also the second test flowchart is subdivide in different steps:

- Step I, from *t0* to *t1* the unloaded specimen at room temperature get heated/cooled until a certain temperature *T1*

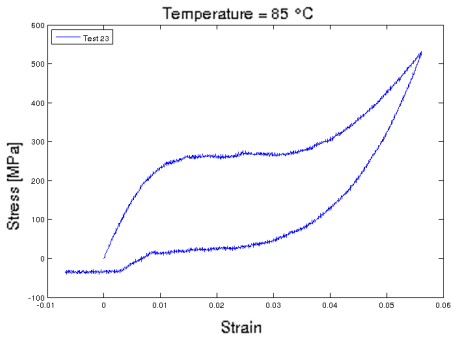

(a) $\sigma - \varepsilon$ curve at $T = 85°C$

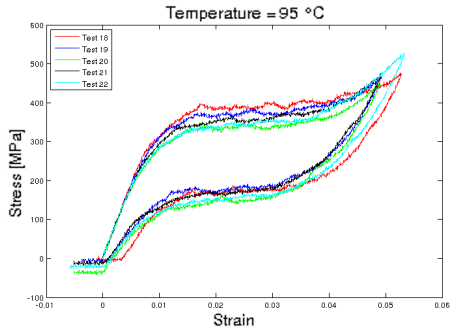

(b) $\sigma - \varepsilon$ curve at $T = 95°C$

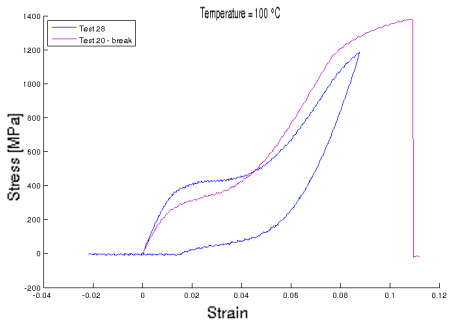

(c) $\sigma - \varepsilon$ curve at $T = 100°C$

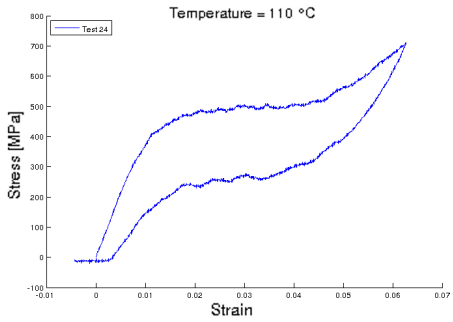

(d) $\sigma - \varepsilon$ curve at $T = 110°C$

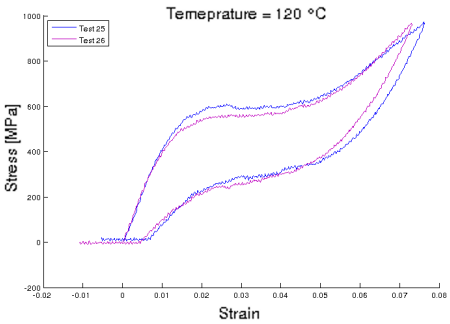

(e) $\sigma - \varepsilon$ curve at $T = 120°C$

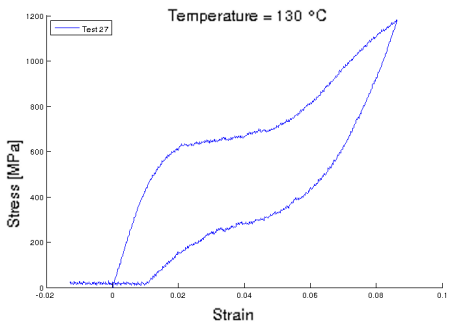

(f) $\sigma - \varepsilon$ curve at $T = 130°C$

Figure 6.15: Output data of experimentsl tests

- Step II, from *t1* to t2: the wire gets loaded until a certain load rate is reached, parameter of each test
- Step III, from *t2* to *t4*: while the displacement of the cross-head is maintained constant, the temperature is cycled between *T1* and *T2*, with $T1 < T2$ or

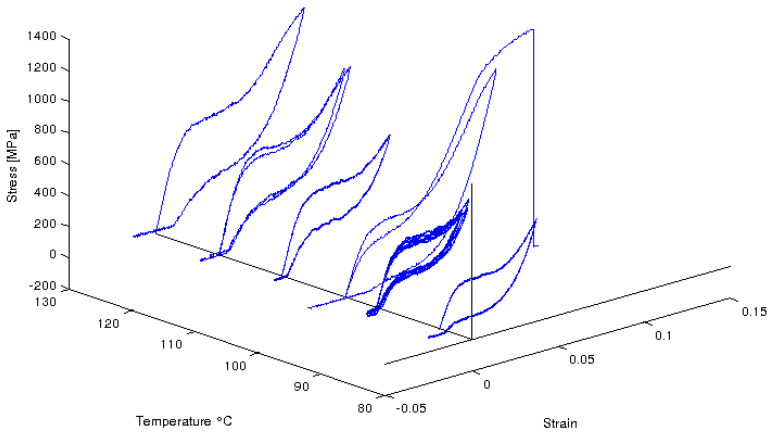

Figure 6.16: Outputs of experimental tests in a $\sigma - \varepsilon - T$ 3D space

$T1 > T2$ indifferently

- Step IV, from *t4* to *t5*: the specimen gets unloaded
- Step V, from *t5* to *t6*: the temperature is brought to the original room temperature

This test is very useful to catch thermal related phenomena and compute the relative parameters. On the other hand, the temperature control (in particular the cooling phases) implies the use of liquid nitrogen, which has a relevant cost. For this reason just few of these tests have been performed, but not enough to use them in the computation of constitutive models parameters.

6.3.2 Derivation of material parameters for SOUZA UMAT

Referring to chapter 3.1, the necessary constitutive parameters have been computed as following (figure 6.18):

- **Young modulus - E**: it has been computed as the average of slopes of the first linear part in the $\sigma - \varepsilon$ curves
- **Poisson's ratio -** ν: is has been taken as a known parameter from literature and set equal to 0.33
- **Linear hardening parameter - h**: it has been computed as the average of slopes of the second linear part in the $\sigma - \varepsilon$ curves

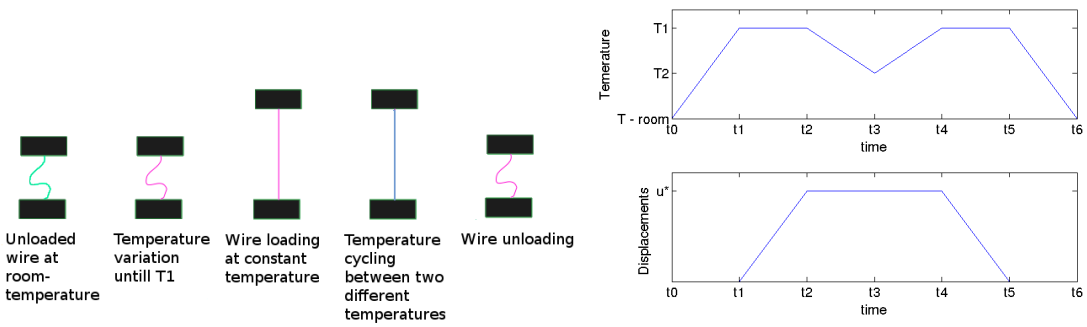

(a) Illustration of the second test flowchart

(b) Variation of control variables during the tensile test

Figure 6.17: Tensile-thermal controlled test flowchart

- **Elastic Radius - R** : it is equal to the half the height of the hysteresis

- **Stress-temperature relation parameter -** β: it has been computed as the slope of the hardening/plateau state through temperature variation, reminding that $\beta = \dfrac{\partial \sigma}{\partial T} \simeq \dfrac{\Delta \sigma}{\Delta T}$. This calculation has been done for each couple of temperature and the final value of β has been computed as the average of the results

- **Maximum transformation strain norm -** ε: it has been computed as the difference in strain between the first elastic loading phase and the quasi-linear unloading phase which are modelled as parallel by the current constitutive model

- **Regularization norm -** Δ: it has been taken as a default value equal to $2 \cdot 10^{-6}$

- **Reference temperature -** T_0: M_f has been taken as reference temperature; in order to compute M_f, the $\sigma - T$ curve has been derived by points: from each pseudo-elastic experimental curve the stress correspond at the end of the direct transformation (the end of the loading plateau) has been taken as the σ coordinate in the mentioned chart, while the T coordinate corresponds to the temperature of the considered specimen. The obtained point ware interpolated linearly in the least square sense and the parameter T_0 has been taken as the intersection between the interpolating curve and the temperatures axis

The final set of parameters for Souza model analyses are reported in table 6.7. The parameters have been tested on the simple 1-D tensile test on the cube (as described

in chapter 5.2) at 85 °C, 95 °C and 110 °C and the results have been compared to the experimental ones, as reported in figure 6.19

Table 6.7: Souza UMAT material parameters

E	Elastic modulus	35800	MPa
ν	Poisson's ration	0.33	[-]
h	Linear hardening parameter	1460	MPa
R	Elastic radius	95	MPa
β	Stress-temperature relation parameter	8.9	MPa/K
ε	Maximum transformation strain norm	4.3	[%]
Δ	Regularization norm	$2 \cdot 10^{-6}$	[-]
T_0	Reference temperature	350	K

6.3.3 Derivation of material parameters for Auricchio-Taylor constitutive model

The second constitutive model implemented in the FEM analyses is Auricchio-Taylor model, which is the default model used in Abaqus to describe pseudo-elastic phenomena. Since it has been created to model superelasticity, it should fit experimental data (performed in a pseudo-elastic test) better than SOUZA. Parameters for Auricchio-Taylor model have been derived from pseudo-elastic curve as shown in figure 6.20 and computed as following:

- E_A, E_M: are the Young Modulus of austenite and martensite phases respectively; they have been derived as the average slope of curve $\sigma - \varepsilon$ before and after the hardening branch
- ν_A, ν_M: are the Poisson's ratio of austenite and martensite phases respectively; they both have been assumed as equal to 0.33, considered a standard magnitude for the current alloy
- ε_L: is the maximum transformation strain norm, computed similarly than for SOUZA, with a coefficient $\sqrt{2/3}$
- β_1, β_2: are the stress-temperature relation parameters for loading and unloading phases respectively; β_1 is the same computed in SOUZA, while β_2 has been computed in the same way, but in the inferior/unloading plateau
- $\sigma_L^S, \sigma_L^E, \sigma_U^S, \sigma_U^E$: are the transformation stresses which correspond to the start of the transformation in loading phase, end of the transformation in loading phase, start of the transformation in the unloading phase and end of the

transformation in the unloading phase respectively. Herein, the stress magnitudes derived from the curve have been rescaled referring to the reference temperature T_0

- T_0: is the reference temperature, computed as it had been computed for SOUZA model
- ε_V: is the maximum transformation volume strain, set equal to ε_L

The final set of parameters for Abaqus superelastic model analyses are reported in table 6.8. The parameters have been tested on the simple 1-D tensile test on the cube (as described in chapter 5.2) at $85\,°C$, $95\,°C$ and $110\,°C$ and the results have been compared to the experimental ones, as reported in figure 6.21

Table 6.8: Auricchio-Taylor material parameters

E_A	Austenite Elastic modulus	35800	MPa
E_M	Martensite Elastic modulus	18488	MPa
ν_A	Austenite Poisson's ration	0.33	[-]
ν_M	Martensite Poisson's ration	0.33	[-]
ε_L	Maximum transformation strain norm	3.86	[%]
β_1	Loading Stress-temperature relation parameter	8.9	MPa/K
β_2	Unloading Stress-temperature relation parameter	6.5	MPa/K
σ_L^S	Start of transformation loading	118	MPa
σ_L^E	End of transformation loading	256	MPa
σ_U^S	Start of transformation unloading	74	MPa
σ_U^E	End of transformation unloading	-48	MPa
T_0	Reference temperature	350	K
ε_V	Maximum transformation volume strain	3.86	[%]

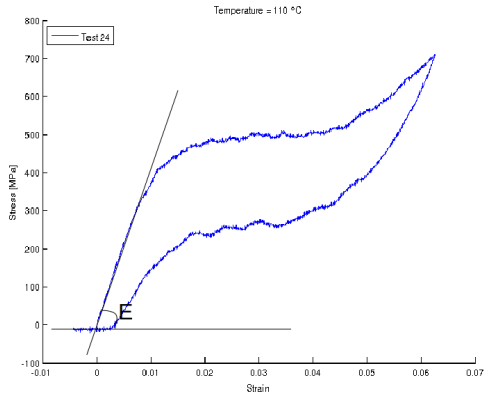

(a) Determination of E

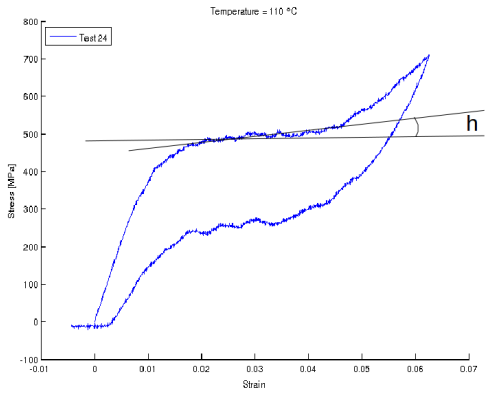

(b) Determination of h

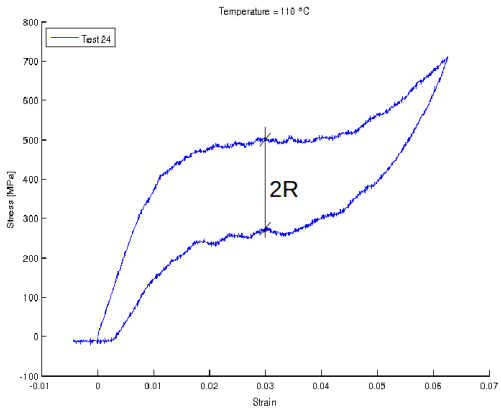

(c) Determination of R

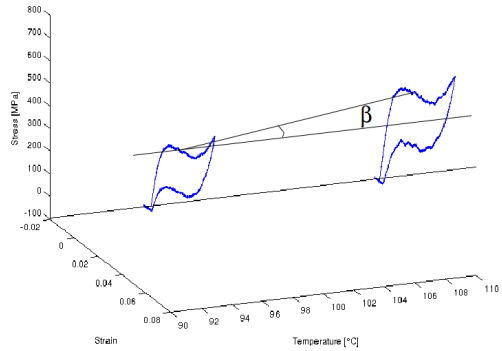

(d) Determination of β

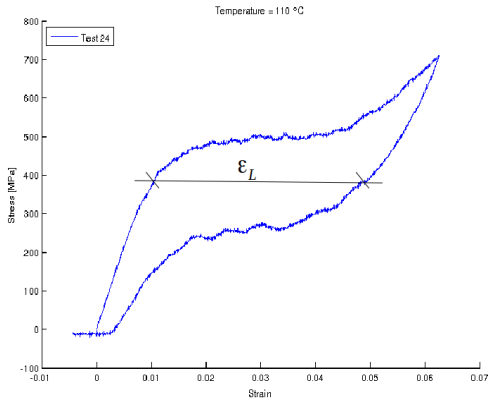

(e) Determination of ε

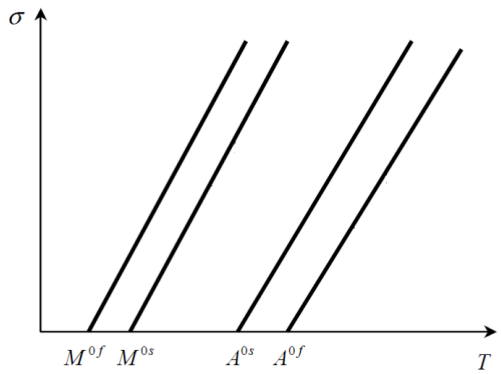

(f) Determination of T_0

Figure 6.18: Output data of experimentsl tests

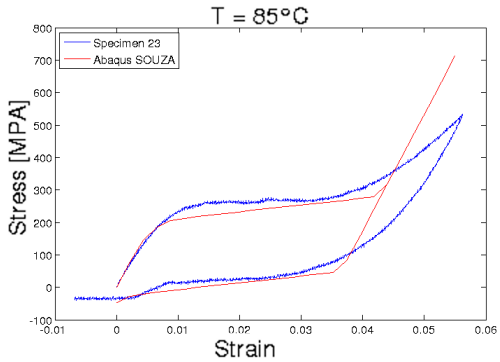

(a) $\sigma - \varepsilon$ curves at 85 $°C$

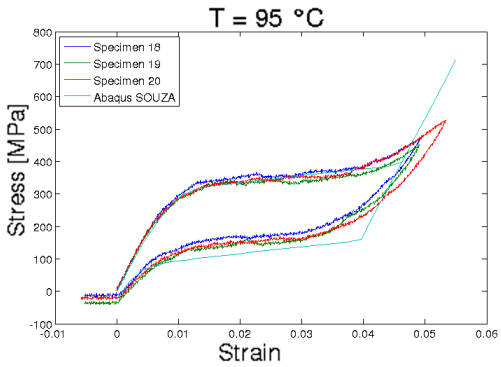

(b) $\sigma - \varepsilon$ curves at 95 $°C$

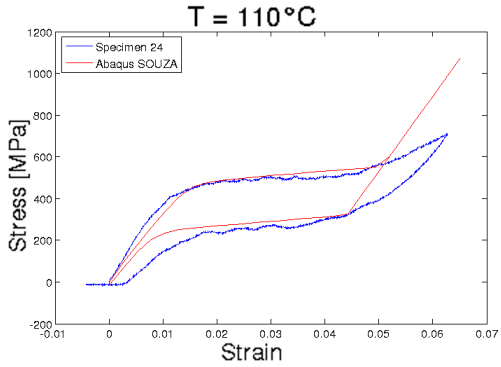

(c) $\sigma - \varepsilon$ curves at 110 $°C$

Figure 6.19: Comparison between FEM analysis and experimental tests - SOUZA UMAT

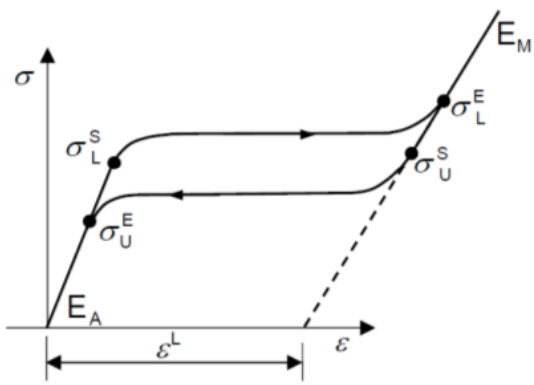

Figure 6.20: Uniaxial SMA behaviour[2]

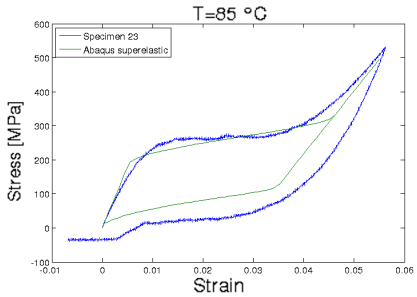

(a) $\sigma - \varepsilon$ curves at $85\,°C$

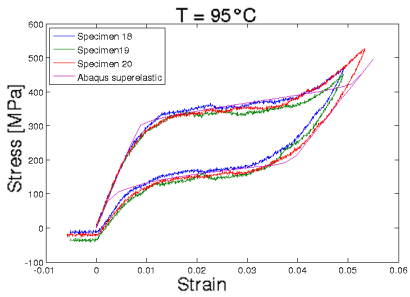

(b) $\sigma - \varepsilon$ curves at $95\,°C$

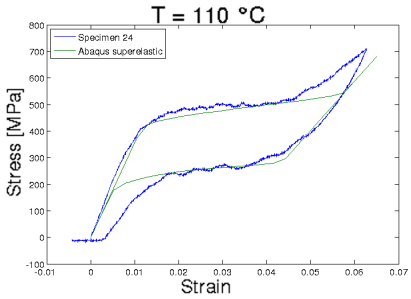

(c) $\sigma - \varepsilon$ curves at $110\,°C$

Figure 6.21: Comparison between FEM analysis and experimental tests - Abaqus superelastic constitutive model

6.4 Modelling of the complete actuation mechanism

Once have modelled the two gripper's main parts, i.e. the SMA wire and the gripper itself, the final analysis of the complete actuation mechanism has been performed. The first wire's end has been connected to the gripper by a rigid body constrain imposed to the nodes evidenced in figure 6.22. On the other hand, the gripper has been clumped at its basis.

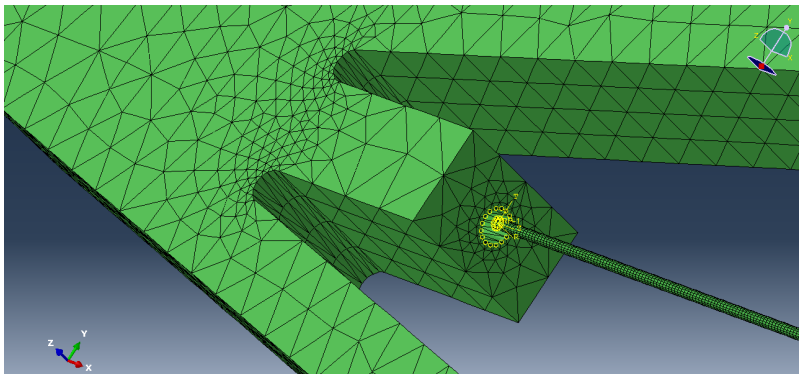

Figure 6.22: Connectivity between the wire and the gripper

The nonlinear analysis (as finite deformation model has been considered) has been subdivided into two different steps: one mechanical step in order to simulate the initial conditions of the actuator and one thermal step aimed to simulate the actuation and gripper's closure/opening motion.
The first step has been subdivided into twenty load steps. At a constant temperature of 420 K and the wire in Austenite phase, the gripper has been closed by applying an adequate displacement ($4\,mm$) to the unconstrained face of the wire. The wire in austenite phase is stiff and stable enough to transfer actuation force to the gripper without transform in martensite and develop a large strain. This step has not a direct correspondence to the real mechanism but, since no direct control of the internal variables could be performed in Abaqus when a UMAT has been used, it is a mean to produce a initial state before the actuation similar to the real one.
The second step has been subdivided in one hundred load steps (which have been increased by Abaqus driver algorithm to 106); the external inputs have been applied smoother than in the first step as in this step are concentrated constitutive model related non-linearities (phase transformations). Boundary conditions on the displacement have been maintained constant, while the temperature has been cycled between $420\,K$ and $306\,K$. When the simulation reaches the temperature of $306\,K$ the martensite transformation is completed and the gripper is open: this is the very moment which correspond to the mounted actuator; following cycles of warming

correspond to the actuation and closure of the gripper. On the other hand, when the temperature decreases, martensite is formed and the gripper works as a bias spring which detwinnes the crystal lattice. The flowcharts of controlled variables, i.e., temperature and one wire's end displacement, are reported respectively in figure 6.23(a) and 6.23(b).

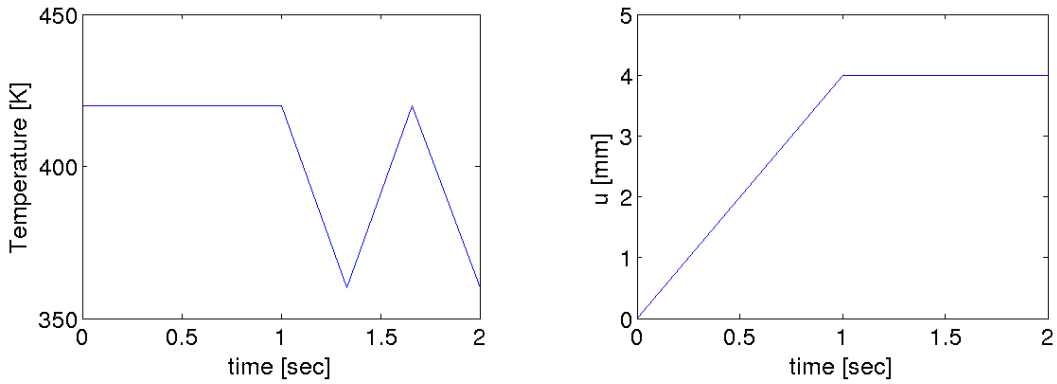

(a) Wire's temperature variation during the analysis

(b) Wire's end displacement during the analysis

Figure 6.23: Control variables flowchart

6.4.1 Simulation outputs

First of all it is important to remark the magnitude of the computational problem in relation to the computing power; the wire has been meshed by 32514 nodes and 25344 "brick" elements, while the gripper has been subdivided in 133177 elements through 133257 nodes. The analyses have been performed using one six-core CPU (Intel(R) Xeon(R) CPU E7540 @ 2.00GHz) which is part of *Computational Mechanics & Advanced Materials Group*'s server capability; the total time required to finish each analysis is about five hours and the output's size is 6 Gb.
Abaqus' output (*.ODB* files) shows the actuation mechanism and the gripper's closure for both SOUZA and pseudo-elastic constitutive models, as shown in figure 6.24. At the same time it is possible to check mechanical variables (such as strain and stress) in the most active zones e.g. the joints and high curvature parts (fig.6.25). Wire's displacement vs time is shown in figure 6.26: both analyses using the two considered constitutive models lead to the same displacement (which correspond to gripper's closure), while the simulated actuating paths are different. It is remarkable that the distance between the pincers behave basically as the wire displacement. SME, which is not modelled in Auricchio-Taylor constitutive model, is shown in figure 6.27; it is remarkable that the actuation is not perfectly centred on the thermal

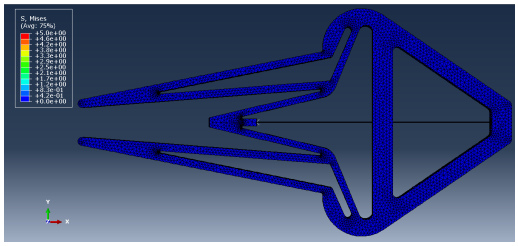

(a) Reference configuration - unmounted gripper

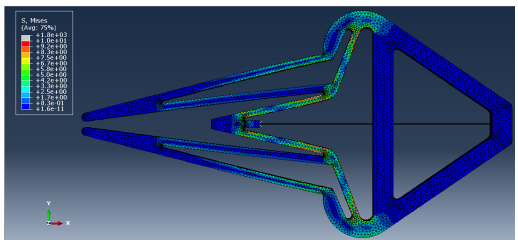

(b) First gripper closure

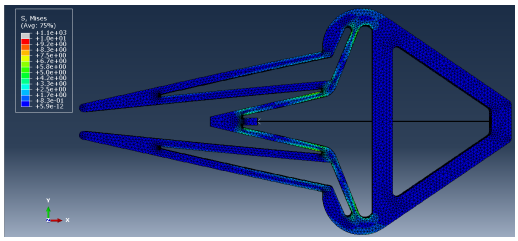

(c) Cooling phase - gripper opening

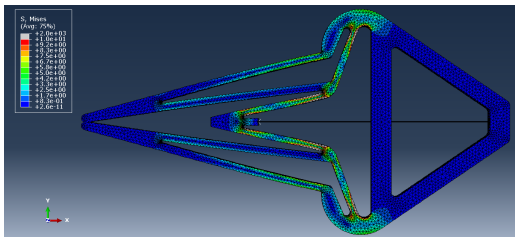

(d) Heating phase - gripper closure

Figure 6.24: Actuation simulation

hysteresis: thanks to FEM simulations is nevertheless possible to make the wire work in the part of phase transformation the designer prefers.
In figure 6.28 is plotted the force passed from the wire to the gripper vs the displacement of wire's end. In the first loading phase the behaviour is the classical PE behaviour before PT2, while the unloading phase is different because of the temperature variation; in the cooling phase, when phase transformation to martensite occurs, the gripper works as a bias spring which deforms the wire and detwinnes martensite lattice.

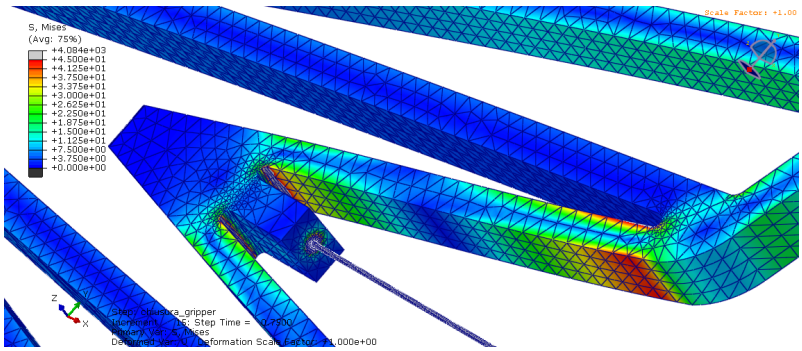

Figure 6.25: Particular of the deformed gripper

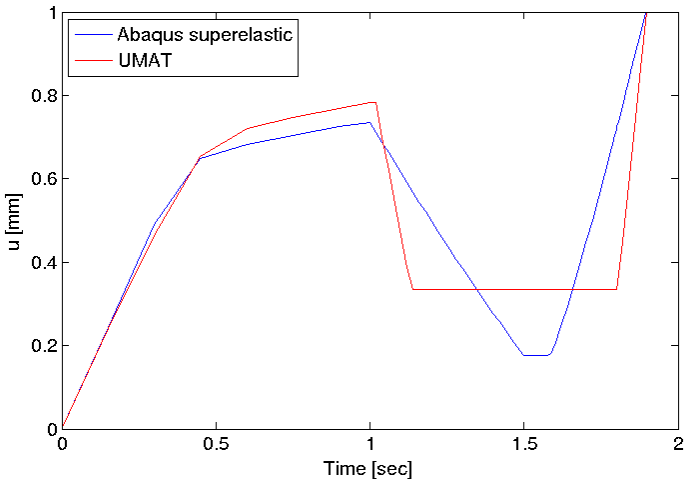

Figure 6.26: Gripper's displacement during actuation

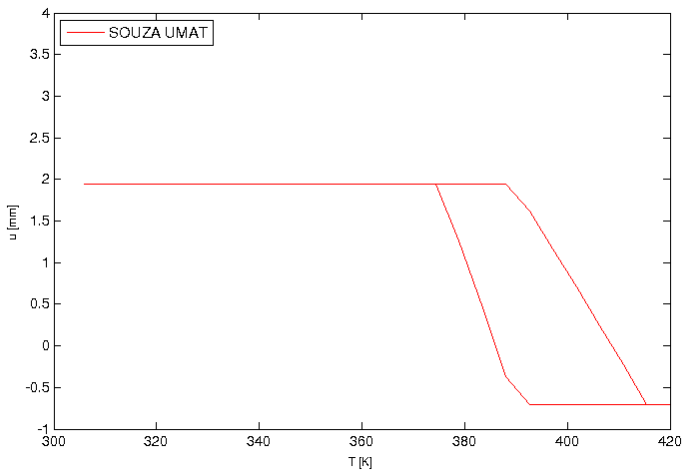

Figure 6.27: Actuator thermal hysteresis

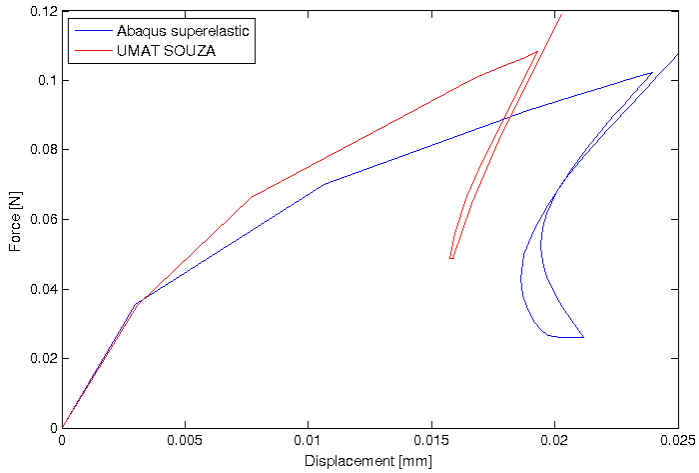

Figure 6.28: u-F curve

6.5 Prototipation of the actuator

The gripper's prototipation has been conduced by the use of "Objet 30Pro 3D printer" (fig.6.29), able to print 3D models in different materials. Models are created through a layer by layer process: the CAD model is virtually sliced, and the printer drops for each slice a layer of material that is then cured using UV light.

From the CAD models of the geometries, plastic grippers have been reproduced, as

Figure 6.29: Objet 30Pro 3D printer

shown in figure 6.30. The pre-tensioned SMA wire has been mounted and crimped in the apposite locations. The actuation gets finally performed by connecting wire's ends to a current generator, as reported in figure 6.31. In figure 6.31 is clear that the actuator starts from a deformed configuration; this phenomena is just partially

predicted by simulations through the elastic-plastic constitutive model used for the gripper. The real problem, not considered in the simulation, was the viscosity of gripper's material: no viscous behaviour were described in the material specification sheet, so that it was neglected; despite this, after the prototype had been completed, it has been noticed that a large amount of time (few minutes) was necessary to the gripper to completely reach a stable configuration.

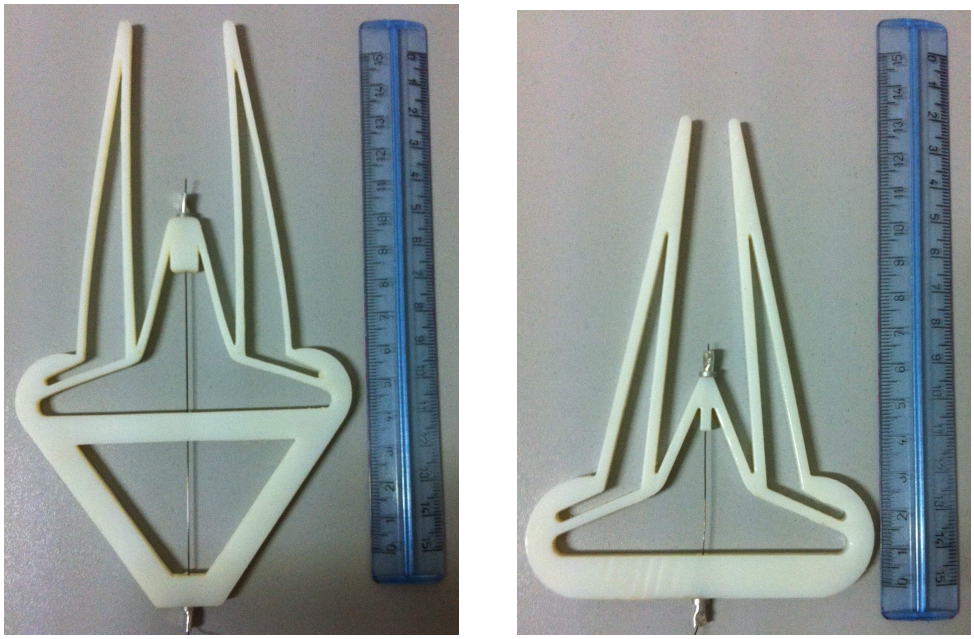

(a) (b)

Figure 6.30: Grippers prototypes

6.6 Conclusions and future developments

The present work aims at showing how FEM analyses can effectively support the design of SMA-based actuators. First of all these analyses allow the designer to predict the mechanical behaviour of actuated mechanism. In chapter 4 was declared the possibility to get fine results in a sensible amount of time and computational work; this possibility is due to the development of an appropriate mesh generation algorithm that optimizes the disposition of nodes and elements in order to get the main mechanism's features with a minimum effort. The use of numerical simulations let also to predict the mechanical behaviour of complex geometries; as seen in section 6.2, this possibility leads to an hight optimization of actuators' geometries which reduces the amount of material used and improves the mechanical skills of

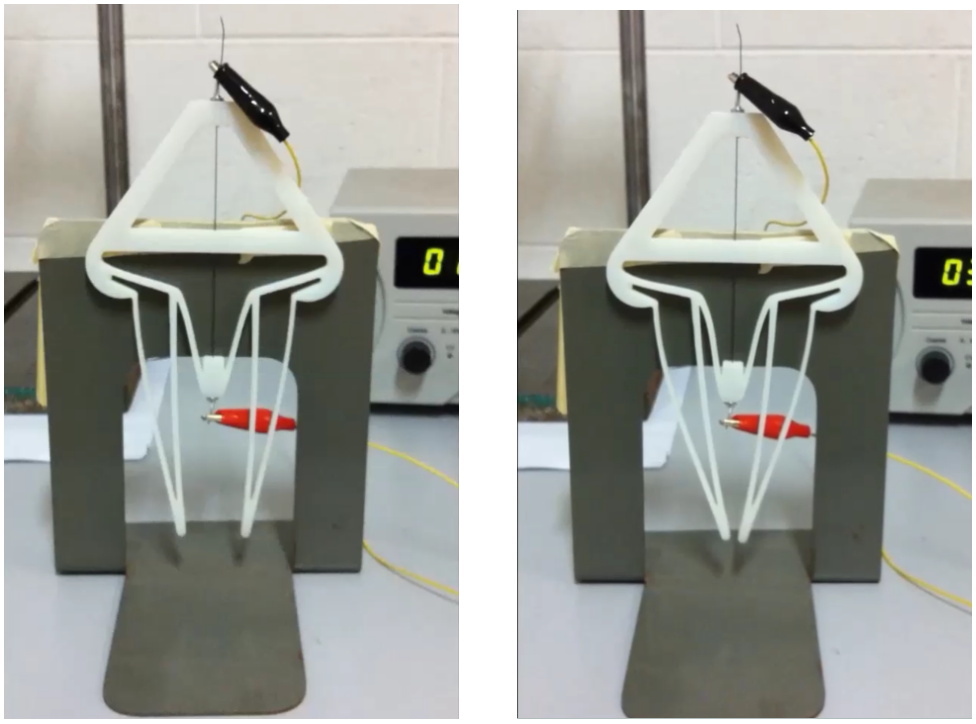

(a) Open gripper - before actuation (b) Close gripper - after actuation

Figure 6.31: Gripper actuation

the actuator itself.
From the SMA constitutive model point of view, the main result reached in this thesis is the possibility to fit complex constitutive model's parameters on simple mono-axial tensile tests. In chapter 6.3 a high correspondence between test data and outputs of FEM analyses is shown; this result is fundamental as lets companies to perform highly accurate simulation starting from few and simple experimental tests. Herein, from the complete actuating mechanism FEM model, is possible to set actuator's working conditions and capitalize the main SMA transformation features. In this moment FEM analyses are not the most common tool in actuators' design, but companies are getting interested in order to product more efficient actuators; starting from this thesis a default path in their modelling could be developed. In order to minimize the amount of time needed to perform FEM simulations, could be relevant the development of an automatic procedure where enforcing the main features of those analyses e.g. mesh generation for the most common geometries (wires, springs), material parameters derivation, standard flowcharts for SMA related experimental tests et cetera.
For the constitutive model's implementation point of view, would be very significant the development of an algorithm or model which includes electrically induced actu-

ation. Even now, using SOUZA and Auricchio-Taylor constitutive models could be possible simulate that in a coupled analysis: at each step of time the temperature variation due to Joule effect is computed and then set as input of UMAT. These kind of simulations would have the great advantage to catch temperature variations through the wire (while in the current thesis the temperature was imposed as constant in the wire) and model the transformation in the very moment it occurs in the different parts of the wire; this possibility could lead to the modelling of more complex plane or spatial problems, where the thermal conductivity, inertia and heat propagation significantly affect SMA related behaviour. On the other hand the development of a direct relation between SMA transformation and electricity (in terms of current intensity or potential difference) would be the perfect tool to perform analyses on actuators, which are commonly electrically actuated. Finally, lots of models are now getting developed with the purpose to catch more SMA features; one of the main fields of research is the modelling of fatigue phenomena, especially for devices which have to endure many cycles.

Bibliography

[1] C. M. Wayman and T. W. Duerig. *An Introduction to Martensite and Shape Memory*, chapter 1.1. Butterworth-Heinemann Ltd., 1990.

[2] F. Auricchio. Numerical implementation of sma constitutive models. Technical report, Università degli Studi di Pavia, 2012.

[3] D. E. Hodgson and R. J. Biermann. Shape memory alloys. *Metals Handbook 2*, 1992.

[4] F. Auricchio and L. Petrini. A three-dimensional model describing stress-temperature induced solid phase transformations: solution algorithm and boundary value problems. *International journal for numerical methods in engineering*, 61:807–836, 2004.

[5] F. Auricchio, R. L. Taylor, and J. Lubliner. Shape-memory alloys: macromodelling and numerical simulations of the superelastic behavior. *Computer Methods in aplpied mechanics and engineering*, 146:281–312, 1997.

[6] A. C. Souza, E. N. Mamiya, and N. Zouain. Three dimensional model for solids undergoing stress-induced phase transformations. *European journal of mechanics*, 17:789–806, 1998.

[7] L. Orgéas and D. Favier. Non-symmetric tension-compression behavior of niti alloy. *Journal de Physique IV*, C8:605–610, 1995.

[8] P. Y. Manach and D. Favier. Shear and tensile thermomechanical behavior of equiatomic niti alloy. *Materials Science and Engineering*, A222:45–57, 1997.

[9] E. Patoor, A. Ebherardt, and M. Berveiller. Micromechanical modelling of superelasticity in shape memory alloys. *Journal de Physique IV*, C1-6:277–292, 1996.

[10] A. M. Freudenthal and P. F. Gou. Second order effects in the theory of plasticity. *Acta Mechanica*, 8:34–52, 1969.

[11] R. von Mises. Mechanik der festen körper im plastisch deformablen zustand. *Göttin. Nachr. Math. Phys.*, 1:582–592, 1913.

[12] *Manual for the Calculation of Elastic-Plastic Materials Models Parameters.*

[13] *ABAQUS - Analysis user's manual*, 6.5 edition.

[14] K. J. Lu and S. Kota. Topology and dimensional synthesis of compliant mechanisms using discrete optimization. submitted to ASME Journal of Mechanical Design, 2005.

[15] Computational Mechanics and Advanced Materials Group. *http://www-2.unipv.it/compmech/.*

[16] K. J. Lu and S. Kota. Design of compliant mechanisms for morphing structural shapes. *Journal of Intelligent Material Systems and Structures*, 14:379–391, 2003.

[17] K. J. Lu and S. Kota. Compliant mechanism synthesis for shape-change applications: Preliminary results. In *Proceedings of the 2002 SPIE Modeling, Signal Processing, and Control Conference*, volume 4693, pages 161–172, March 2002.

[18] F. Auricchio, M. Conti, S. Morganti, and A. Reali. Shape memory alloy: from constitutive modeling to finite element analysis of stent deployment. *Computer Modeling in Engineering and Sciences*, 57:225–243, 2010.

[19] F. Auricchio. *Shape memory alloys: applications, micromechanics, macromodelling and numerical simulations.* PhD thesis, University of California at Berkeley, 1995.

[20] D. Fugazza. *Use of Shape-Memory Alloy Devices in Earthquake Engineering: Mechanical Properties, Advanced Constitutive Modelling and Structural Applications.* PhD thesis, Università degli studi di Pavia, 2005.

[21] J. L. Proft and T. W. Duerig. *The Mechanical Aspects of constrained recovery*, chapter 2.1. Butterworth-Heinemann Ltd., 1990.

[22] T. W. Duerig, D. Stöckel, and A. Keeley. *Actuator and work Production Devices*, chapter 3.1. Butterworth-Heinemann Ltd., 1990.

[23] J. Perkins and D. Hodgson. *The Two-Way Shape Memory Effect*, chapter 3.2. Butterworth-Heinemann Ltd., 1990.

[24] P. Tautzenberger. *Thermal Actuators: A Comparison of Shape Memory Alloys with Thermostatic Bimetals and Wax Actuators*, chapter 3.3. Butterworth-Heinemann Ltd., 1990.

[25] T. Waram. *Design Principles For Ni-Ti Actuators*, chapter 3.5. Butterworth-Heinemann Ltd., 1990.

[26] D Stöeckel. *Shape Memory Actuators for Automative applications*, chapter 4.1. Butterworth-Heinemann Ltd., 1990.

[27] Y. Furuya and H. Shimada. *Shape memory Actuators for Robotic Applications*, chapter 4.5. Butterworth-Heinemann Ltd., 1990.

[28] T. W. Duerig and R. Zadno. *An Engineer's Perspective of Pseudoelasticity*, chapter 5.1. Butterworth-Heinemann Ltd., 1990.

[29] Q. Chang-jun, M. Pei-sun, and Y. Qin. A prototype micro-wheeled-robot using sma actuators. *Sensors and Actuators*, 113:94–99, 2004.

[30] F. Auricchio. A robust integration-algorithm for a finite-strain shape-memory-alloy superelastic model. *International journal of Plasticity*, 17:971–990, 2000.

[31] K. J. Paik and R. J. Wood. A bidirectional shape memory alloy folding actuator. *Smart materials and structures*, 21, 2012.

[32] F. Auricchio and E. Bonetti. A new "flexible" 3d macroscopic model for shape memory alloy. *Discrete and continuous dynamical systems series*, 6:277–291, 2013.

[33] M. Mertmann and G. Vergani. Design and application of shape memory actuators. *The european physical journal*, 158:221–230, 2008.

[34] L. Howell, P. Magleby, and M. Olsen. *Handbook of Compliant Mechanisms*. John Wiley & Sons, 2013.

[35] W. Huang. on the selection of shape memory alloys for actuators. *Materials and Design*, 23:11–19, 2001.

[36] A. D. Johnson. Shape memory alloy rotary actuator. USP, 8 1989.

[37] J. R. Anadòn. Large force shape memory alloy linear actuator. Master's thesis, University of Florida, 2002.

[38] W. Huang. Modified shape memory alloy (sma) model for sma wire based actuator design. *Journal of intelligent material systems and structures*, 10:221, 1999.

[39] F. Auricchio. Numerical implementation of sma constitutive models. Technical report, Università degli Studi di Pavia, 2011.

[40] F. Butera. Shape memory actuators for automotive applications. Technical report, FIAT Research Centre (CRF), 2001.

[41] M. Rota. Compositi attivi con materiali a memoria di forma. Master's thesis, Università degli studi di Pavia, 2001.

Ringraziamenti

Alla fine della mia tesi triennale scelsi di mettere un brevissimo elenco di ringraziamenti che, seppur sinceri, risultavano abbastanza sommari e distaccati. Presi questa scelta un po' perchè consideravo la laurea triennale come un momento di passaggio, gratificante, ma destinato a finire nello spazio dei miei ricordi denominato "cose che passano"; un po' perchè ero convinto che ci sarebbe stato sempre tempo e modo per ringraziare le persone a cui tengo per il fatto di aver incrociato il mio cammino. Ebbene, dopo due anni, mi sento di cambiare l'approccio: ho scoperto con rammarico che bisogna ringraziare tali persone subito, sempre, altrimenti le si ringrazierà sempre un giorno dopo il possibile e la mia laurea mi sembra un discrimine abbastanza netto nella mia vita per cui vale la pena cimentarsi nell'atto dei ringraziamenti.
Un grazie di cuore va quindi

- a Ferdinando Auricchio, per tutte le critiche e per avermi sempre fornito un punto di vista sulle cose molto diverso dal mio, aiutandomi a migliorare il mio lavoro e le mie capacità accademiche sotto aspetti a cui io non avrei mai dato importanza

- ad Alessandro Reali, per tutto il sapere che ha condiviso con me, esprimibile non tanto in nozioni, quanto nel trasmettere la forma mentis con la quale affronta le varie situazioni, ma soprattutto per la passione che mette nel proprio lavoro. E' quella passione ad avermi chiarito, una volta per tutte, cosa voglio fare da grande

- a Mauro ed Elisa, per avermi accompagnato nella costruzione di questa tesi, dedicandomi una quantità di tempo per cui sarò loro sempre riconoscente

- a Mauro, perchè lui merita senz'altro un doppio ringraziamento, se non altro per aver corretto il mio sublime stile di scrittura in inglese: se mai fossi in grado di scrivere un testo intelligibile in inglese, sarà solo merito suo

- ai miei genitori, anzi, a mio Papà e a mia Mamma, che mi son sempre stati vicino, nonostante io sia alquanto insopportabile; grazie per il vostro amore, grazie per il vostro esempio, grazie per i vostri sacrifici. Grazie (repetita iuvant)

- a Matteo, perchè una cosa è essere fratelli con un anno di distanza, una cosa è esserlo con nove: non è scontato, non è banale, ma è un rapporto a cui non rinuncerei mai; so che sei il mio primo tifoso, sappi che sei il mio primo esempio

- a Mitch, Gio, Queque, Claudia, Raffa: scusate se vi raggruppo, ma devo portare la tesi a stampare e il tempo scarseggia. E' questa la cosa bella: non serve dirlo, non serve vedersi tutte le settimane (anche se penso di aver passato con Mitch più tempo che con il resto dell'umanità): con voi ho un legame più profondo di una prova CPT (Mitch, a te l'onore di spiegare la similitudine) e non ci sarà distanza né tempo capaci di scalfirlo

- a Bruno e a tutti i dispo 2014, perchè l'unità di misura dell'amicizia e della condivisione non sono le ore, i giorni o gli anni: siete stati un tesoro inaspettato e con voi ho condiviso la parte più bella di me

- a Claudio che, nonostante tutto, non è ancora riuscito a convincermi a prendere un Mac

- a Maru, Krum-cuore-di-panna, Gina, Mattia, Emma, Marcomes, Bianca, Franci, Giulia, Bea e a tutti quelli che mi hanno incrociato in questi bellissimi 24 anni, che sono un pezzetto della mia vita e a cui va il mio sincerissimo abbraccio

- a Greta, che più che una cugina è una sorella

- a LaTeX, perchè mi ha insegnato che, nella vita, se non voglio mettere una figura in un posto, non c'è nessun uomo, comando o Dio che possa obbligarmi a farlo

- a Tux, perchè da quando "windows" sono solo degli aggeggi di vetro per far entrar luce nelle stanze, è tutta un'altra cosa; senza di lui sarei ancora ad aspettare che Abaqus rispondesse

- a Marta, perchè con lei ho condiviso tutti gli aspetti della mia persona. Ma tutti tutti. E lei non è scappata, anzi, è rimasta, facendomi capire quanto io sia fortunato. Poi, si sa: condividi oggi, condividi domani... finiremo per condividere anche dopodomani

- a mia nonna, anche se avrei dovuto farlo prima. Perchè qualunque cosa di buono ci sia in me, lo devo a lei, ma soprattutto perchè continuo a sentirla vicina